Durham University

Durham E-Theses

Nanoscale silver: Thin-film structure and antimicrobial functionality

ANDREW KRISTOFFER DEAN

How to cite:

DEAN, ANDREW KRISTOFFER (2012) Nanoscale silver: Thin-film structure and antimicrobial functionality. Masters thesis, Durham University.

Use policy

The full-text may be used and/or reproduced, and given to third parties in any format or medium, without prior permission or charge, for personal research or study, educational, or not-for-profit purposes provided that:

- a full bibliographic reference is made to the original source
- a https://etheses.durham.ac.uk/id/eprint/5896/ is made to the metadata record in Durham E-Theses
- the full-text is not changed in any way

The full-text must not be sold in any format or medium without the formal permission of the copyright holders.

Please consult the full Durham E-Theses policy for further details.

Academic Support Office, The Palatine Centre, Durham University, Stockton Road, Durham, DH1 3LE
e-mail: e-theses.admin@durham.ac.uk Tel: +44 0191 334 6107
https://etheses.durham.ac.uk

Nanoscale silver: Thin-film structure and antimicrobial functionality

Dr Andrew Kristoffer Dean

A thesis submitted in partial fulfilment of the requirements for the degree of Master of Philosophy

University of Durham

2012

Abstract

Since antiquity, silver has been used as a material to reduce spoilage. Over the past decades, there has been an increasing scientific and commercial interest in developing silver surfaces due to the increasing number of drug resistant microorganisms. In this study, the effect of nanostructuring silver films as an antimicrobial against the bacteria *Escherichia coli* (*E. coli*) and *Staphylococcus aureus (S. aureus)* was examined. Films consisting of 3 nm chromium adhesion layers and nominal 20 nm silver surfaces (assuming flat deposition) were deposited by thermal evaporation and nanostructuring was controlled by varying the incident angle of the silver onto the substrate. Four substrate angles were used including 0 °, 18 °, 40 ° and 70 ° to the horizontal. Examination by atomic force microscope, Rutherford backscattering and ellipsometry showed that as the incident angle of deposition increased, so did the nanostructuring and surface roughness. This was coupled with a decrease in film thickness. Incubation of the nanostructured thin-films in bacterial broths with *E. coli* and *S. aureus* showed that as the surface roughness increased the antimicrobial activity was enhanced – both in solution and for bacteria adhered to the thin-films. Inductively coupled plasma mass spectrometry was used to measure silver leaching from the thin-films and showed a negligible loss for all films, with corresponding low-levels of antimicrobial activity. Further indicating the enhancing effect of nanostructuring as an antimicrobial. All thin-films showed biological fouling after prolonged exposure to the bacterial solutions, which reduced antimicrobial activity. Cleaning the films with IPA showed that the films could be regenerated but with some loss of antimicrobial activity. The mechanism of thin-film antimicrobial activity is at

this time unknown but it is speculated that nanostructuring is capable of penetrating the cell envelopes of bacteria, which enhances the antimicrobial activity of silver.

Declaration

Unless explicitly stated otherwise, the work presented in this thesis is solely that of Dr Andrew Kristoffer Dean, Spartan Nano Ltd and Durham University and has not been submitted for examination for any other degree.

All antimicrobial testing was carried out at the Molecular Workstation in Newcastle (UK), in conjunction with Dr Ashley Chessher. Dr Andrew Kristoffer Dean, Spartan Nano and Durham University own all intellectual property.

RBS, Ellipsometer and AFM experiments were carried out in the Centre for Materials Chemistry with Dr Richard Thompson. SEM measurements were taken within the Durham University Electron Microscopy Facility with Leon Bowen.

I certify that this statement is correct.

Dr Andrew Kristoffer Dean

Copyright © 2012 by Andrew Kristoffer Dean. No part of this work may be reproduced without the written permission of the author.

Table of Figures

Figure 1. Diagrammatic representation of three methods of thin-film growth……..9
Figure 2. Diagrammatic representation of a thermal evaporator……... 10
Figure 3. Scanning electron microscope images of AFM cantilevers and tip…….... 15
Figure 4. Schematic of an Atomic Force Microscope……... 16
Figure 5. AFM scans of surface roughness……17
Figure 6. Schematic of a Rutherford Backscatter system……..22
Figure 7. RBS ion interaction with a surface……23
Figure 8. RBS spectrum……25
Figure 9. Diagrammatic representation of an ellipsometer……26
Figure 10. Piezoelectric quartz crystal representation……... 31
Figure 11. Schematic of a scanning electron microscope……..34
Figure 12. Schematic representation of the interaction volume and penetration depth……...34
Figure 13. Monte Carlo simulation of electron scattering…… 35
Figure 14. Schematic illustration of an Inductively Coupled Plasma…….....38
Figure 15. Schematic of a Mass Spectrometer……...39
Figure 16. Diagrammatic representation of a Gram-negative cell envelope……. 44
Figure 17. Transmission electron micrograph of *E. coli* cells……..... 45
Figure 18. Diagrammatic representation of a Gram-positive cell envelope…….. 46
Figure 19. Transmission electron micrograph of *S. aureus* cells…….....47
Figure 20. Theoretical bacterial growth curve……...48
Figure 21. Diagrammatic representation of an absorbance microplate spectrophotometer setup…… 52
Figure 22. Schematic of a bright field light microscope……53
Figure 23. Molecular structure of Crystal Violet……...54
Figure 24. Molecular structure of Safranin……55
Figure 25. Molecular structure of Tryan Blue……... 55
Figure 26. Trypan Blue staining…… 56
Figure 27. Thermal evaporator sample holder……...68
Figure 28. Scanning electron microscopy images of thin-film silver surfaces……..80
Figure 29. Examples of tapping AFM images……... 81

Figure 30. AFM lines profiles……82
Figure 31. RMS silver surface roughness……..83
Figure 32. The average width of the large intermittent peaks……... 84
Figure 33. Total film thickness…….. 85
Figure 34. Total film thickness over a 16-week period…… 86
Figure 35. Rate of film growth on top of the silver surfaces…… 87
Figure 36. Loss of chromium from thin-films……... 88
Figure 37. Loss of silver from thin-films……...88
Figure 38. Raw data optical density of *E. coli* growth…….....92
Figure 39. Normalised *E. coli* growth curves……..... 93
Figure 40. Normalised *S. aureus* growth curves……93
Figure 41. Reduction in *E. coli* growth…….....94
Figure 42. Reduction in *S. aureus* growth…… 95
Figure 43. Solution based chromium and silver reduction in bacterial growth……. 96
Figure 44. Percentage of denatured *E. coli* cells bound to the silver surfaces examined by Trypan Blue staining…….....98
Figure 45. Percentage of denatured *S. aureus* cells bound to the silver surfaces examined by Trypan Blue staining…… 98
Figure 46. Frequency shifts from *E. coli* binding to silver coated quartz crystals… 100
Figure 47. Frequency shifts from *S. aureus* binding to silver coated quartz crystals……... 100
Figure 48. *E. coli* mass adsorption to silver coated quartz crystals……... 102
Figure 49. *S. aureus* mass adsorption to silver coated quartz crystals……...102
Figure 50. AFM line profiles after cleaning……...104
Figure 51. The effect of cleaning on RMS surface structure……107
Figure 52. AFM average width of large intermittent peaks after cleaning…… 109
Figure 53. AFM total film thickness after Cleaning…….. 111
Figure 54. Effect of IPA cleaning on silver thin-film mediated *E. coli* antimicrobial activity……..113
Figure 55. Effect of IPA cleaning on silver thin-film mediated *S. aureus* antimicrobial activity……..114

Table of Equations

Equation 1. R_a Surface roughness……..13
Equation 2. RMS Surface roughness……. 14
Equation 3. Kinematics of the collision of an incoming ion and atomic nucleus…..24
Equation 4. Kinematic factor K……..... 24
Equation 5. The difference in phase difference Delta (Δ)……. 26
Equation 6. Ratio of magnitude of the total reflection coefficient Psi (Ψ)……27
Equation 7. Change in polarisation Rho (ρ)…….. 27
Equation 8. Piezoelectric crystal peak kinetic energy density…….....28
Equation 9. Piezoelectric crystal peak potential energy density……29
Equation 10. Piezoelectric crystal balanced peak potential and potential energies...29
Equation 11. Linear approximation of mass binding and frequency shift……30
Equation 12 Piezoelectric crystal thickness…….. 30
Equation 13. Resonant frequency related to the N^{th} mode…… 30
Equation 14. Shear wave phase velocity……31
Equation 15. The Sauerbrey Equation……... 31
Equation 16. Piezoelectric crystal solution measurement……..32
Equation 17. Inverse dependence of inelastic scattering on kinetic energy…….. 36
Equation 18. Kinetic energy of an ion……40
Equation 19. Magnetic force……..40
Equation 20. Centripetal force……... 40
Equation 21. Velocity of an ion in a magnetic field…….. 40
Equation 22. Mass/charge ration with respect to field strength……41
Equation 23. MS Mass resolution……..41
Equation 24. Beer-Lambert law……51
Equation 25. Optical density……..51
Equation 26. Antimicrobial activity……...76
Equation 27. Standard deviation……91

Table of Tables

Table 1. Antimicrobial activity of silver nanoparticles...…….. 61
Table 2. Table of controls and experimental procedures for determining antimicrobial activity……. 75
Table 3. The RMS and average peak widths of surfaces after cleaning…… 108

Abbreviations

AFM	Atomic Force Microscope
SPM	Scanning Probe Microscope
STM	Scanning Tunneling Microscope
PSD	Position Sensitive Detector
RBS	Rutherford Backscattering
ICPMS	Inductively Coupled Plasma Mass Spectrometry
ICP	Inductively Coupled Plasma
MS	Mass Spectrometer
QMF	Quadropole Mass Filter
TOF	Time-of-Flight
QCM	Quartz Crystal Microbalance
CVD	Chemical Vapour Deposition
PVD	Physical Vapour Deposition
SEM	Scanning Electron Microscope
RMS	Root Mean Squared
E. coli	*Escherichia coli*
S. aureus	*Staphylococcus aureus*
MHz	Megahertz
UV-vis	UV-Visible Spectrophotometer
PBS	Phosphate Buffered Saline
SSC	Sodium chloride-sodium citrate
TE	Tris.HCl
PPM	Parts-per-million
PPB	Parts-per-billion

Symbols

General

M	Molarity
g	Gram
º C	Degrees Celsius
º	Plane Angle
H^+	Hydrogen Ion

Rutherford Backscattering

k	Kinematic Factor
$E_{Scattered}$	Energy of the scattered ions
$E_{incident}$	Energy of the incident ions
M_1	Incident Ion Mass
M_2	Target Nuclear Mass
θ	Scattering Angle
p-	Electric field parallel to the plane of incidence
s-	Electric field perpendicular to the plane of incidence
Δ	Change in phase difference that occurs upon reflection
Ψ	The angle whose tangent is the ratio of the magnitude of total reflection coefficients
δ_1	Difference between the parallel component and perpendicular component of the incoming wave
δ_2	Difference between the parallel component and perpendicular component of the outgoing wave

Ellispometry

R_p	Change in the Fresnel reflection coefficient for *p*- polarised light
R_s	Change in the Fresnel reflection coefficient for *s*- polarised light
δ_1	Difference between the parallel component and perpendicular component of the incoming wave
δ_2	Difference between the parallel component and perpendicular component of the outgoing wave
Ψ	Ratio of the magnitude of the total reflection coefficient
ρ	Change in polarization
e	Exponential
Δ	Change in phase difference

Piezoelectric Measurement

A	Coating area of the electrode
c	Stiffness sensitivity
C_f	Integral sensitivity
Δf	Change in resonant frequency
f_0	Fundamental frequency of the transducer
h_s	Crystal thickness
k	Electromechanical coupling coefficient
λ	Acoustic wavelength
ΔM_s	Mass of material adsorbed/deposited on the crystal electrode
μ	Shear modulus
μ_q	Shear stiffness
N	Integer
η	Viscosity
η_1	Viscosity of the liquid contacting the crystal
ρ	Crystal density

ρ_q	Mass per unit volume of quartz
ρ_s	Mass per surface area of quartz
ρ_1	Liquid density contacting the crystal
Q	Electrical quality factor
u	Component of displacement
U_k	Peak crystal kinetic energy density
U_p	Peak crystal potential energy density
v_a	Phase velocity of the acoustic wave
v_s	Shearwave phase velocity
ω	Angular frequency of the circuit
ω_0	Unperturbed resonant frequency

Scanning Electron Microscope

P_i	Probability of inelastic scattering
Z	Electrons within an atom
E	Kinetic energy lost by the electron and gained by an atom
u	atomic mass unit
A	Atomic mass number
ρt	Mass-thickness of the specimen
α	Scattering cross section of nucleus presented to each incident electron.

Inductively Coupled Plasma Mass Spectrometry

z	Charge of the ion
e	elementary charge
V	Acceleration voltage
v	Velocity of the ion after acceleration
m	Mass of the ion
B	Magnetic field strength
r	Radius of the magnetic field
Δm	Difference between two adjacent mass peaks
m	Nominal mass of the first peak.

List of Presentations

Chapter 4, 5 and 6 contain material that was orally presented:

Dean, A. K., Atkinson, D. 'Bacterial interactions with nanostructured surfaces', *IOP, Complex Molecules at Surfaces*, March 2011.

Dean, A. K., Atkinson, D. 'Nanostructured Antimicrobial Films for Healthcare Applications', *METRC, Nanotechnology: Delivering Innovation*, February 2012.

Dean, A. K., Atkinson, D. 'Nanostructured Antimicrobial Films for Textile Applications', *KTN, Nano4Design*, February 2012.

Acknowledgements

I would like to thank my supervisor Dr Del Atkinson for his support, guidance and friendship throughout the duration of this project. I would also like to express my gratitude to all of the members of the Nanoscale Science and Technology group for their warmth and support.

I am deeply indebted to Dr Richard Thompson for his thoughts on surface analysis and assistance in developing my physical chemistry skills and understanding in this area.

I would like to thank Dr Ashley Chessher from the Molecular Workstation for his help examining biomolecular interactions with the fabricated surfaces.

Leon Bowen is also thanked for his help in SEM imaging of the silver nanostructures.

The Durham Industrial Bridging Fellowship (DIBF), Spartan Nano Limited and the Molecular Engineering Translational Research Centre (METRC) are thanked for their financial support of this project.

I would finally like to thank my friends and family for all of their love and support throughout this work.

Table of Contents

Abstract……i
Declaration……iii
Table of Figures……iv
Table of Equations……vi
Table of Tables……vii
Abbreviations……viii
Symbols……ix
List of Presentations……xiii
Acknowledgements……xiv
Table of Contents……xv

Chapter 1. Introduction……1
1.1. Motivation and Aim……1
1.2. Thesis Outline……3

Chapter 2. Theory……6
2.1. Thin-Film Fabrication and Characterisation……7
2.1.1. Thin-Film Characterisation……8
2.1.2. Thermal Evaporation……9
2.1.3. Surface Roughness……11
2.1.4. Inducing Surface Roughness……11
2.1.5. Calculating Surface Roughness……13
2.1.6. Material Measurements – Analysis Techniques……15
2.1.7. Atomic Force Microscopy……15
2.1.8. Rutherford Backscattering……22
2.1.9. Ellipsometry……25
2.1.10. Piezoelectric Quartz Crystal Mass Measurement……28
2.1.11. Scanning Electron Microscopy……33
2.1.12. Inductively Coupled Plasma Mass Spectrometry……37
2.1.12.1. Inductively Coupled Plasma……38
2.1.12.2. Mass Spectrometer……39

2.2. Bacterial Interactions with Surfaces……42
2.2.1. Bacterial Cell Envelope……43
2.2.2. Gram-Negative Bacteria…….. 44
2.2.3. Gram-Positive Bacteria……46
2.2.4. Bacterial Growth……..48
2.2.5. Quantification of Bacterial Population Growth……... 50
2.2.6. Absorbance Spectrophotometry……...51
2.2.7. Light Microscopy……53
2.2.8. Bacterial Staining – Gram and Trypan Blue……54
2.2.9. Silver as an Antimicrobial……57
2.2.10. Ionic Silver Antimicrobial Activity……58
2.2.11. Silver Nanoparticle Antimicrobial Activity……...58
2.2.12. Nanoscale Structure and Surfaces Antimicrobial Activity…….63
2.2.13. Chromium Adhesion Layer Toxicity..... 64
2.3. Surface Fouling and Cleaning……65

Chapter 3. Materials and Methods……67
3.1. Thin-Film Sample Preparation……68
3.1.1. Scanning Electron Microscopy…… 69
3.1.2. Material Thickness……...70
3.1.3. Post Deposition Changes……..71
3.1.4. Metal Desorption……..71
3.2. Biological Experimental Methods……...72
3.2.1. Biological and Biochemical Stocks……..72
3.2.2. Bacterial Growth Methodology……73
3.2.3. Solution Based Antimicrobial Activity……74
3.2.4. Surface Bound Antimicrobial Activity……76
3.2.5. Bacterial Adsorption on Surfaces……77
3.3. Thin-Film Cleaning……77

Chapter 4. Results and Discussion: Nanostructured Thin-Films…..……..... 78
4.1. Surface Structuring Thin-Film Island Formation……..……. 79
4.2. As-Deposited Film Thickness..…….. 85
4.3. Post Deposition Surface Changes……... 86

4.4. Desorbed Silver and Chromium from Nanostructured Surfaces……..... 88

Chapter 5. Results and Discussion: Bacterial Interactions with Fabricated Surfaces…….....……... 90
5.1 Biological Reproducibility.....……91
5.2. Solution Based Antimicrobial Activity.....……95
5.3. Desorbed Silver and Chromium Antimicrobial Activity.....…… 96
5.4. Surface Binding of Bacteria and Antimicrobial Activity...…… 97
5.5. Surface Fouling.....…….99

Chapter 6. Results and Discussion: Surface Cleaning and Antimicrobial Activity...103
6.1. Thin-film Cleaning and Antimicrobial Activity...…….. 103
6.2. Surface Structure.....……..104
6.3. Material Thickness after Cleaning..... 110
6.4. Effect of Cleaning on Fouled Thin-Films.....…….112

Chapter 7. Conclusions..... 115
7.1. Thin-Film Fabrication and Characterisation.....115
7.2. Bacterial Interactions with Thin-Films..... 117
7.3. Thin-Film Cleaning and Antimicrobial Activity..... 120

Chapter 8. Future Work……..123

References…….……126

Appendices…….....151
Appendix A. Raw data optical density of *E. coli* growth.....151
Appendix B. Raw data optical density of *S. aureus* growth.....152

Chapter 1. Introduction

1.1. Motivation and Aim

As a medical treatment, bulk silver has been used since the ancient Greeks and Egyptians, with Hippocrates making mention of its uses to treat ulcers (Hippocrates, 400 B. C.). The first recorded use of silver as an antimicrobial was in 1884 by the German obstetrician, C. S. F. Crede who used a 1 % solution of silver nitrate to prevent the disease gonococcal ophthalmia neonatorum caused by the bacteria *Neisseria gonorrhoeae* and *Chlamydia trachomatis* (Russell and Hugo, 1994). Since then, silver has been used widely for the treatment of pathogenic infections, to inhibit bacterial growth and to coat medical devices, such as wound dressings (Russell *et al*, 1994) and catheters (Silver 2003). In particular, it has been used to hinder the growth of bacterial cells or to denature them. The mechanisms of silver activity with bacteria are dependent upon the form of silver during the microbial interaction. It is known that silver ions (Ag^{+}) interact strongly with electron donors (Brook *et al*, 2006) and that in ionic form it can readily undergo metal-ligand reactions with protein groups containing thiols and sulfides (Clement *et al*, 1994; Fernández *et al*, 1996; Liau *et al*, 1997). Silver is also known to interact with other cellular components such as nucleic acids (Jensen *et al*, 1996) and has been shown to inhibit energy production by inhibition of the bacterial respiratory chain (Bragg *et al*, 1973).

Antimicrobial surface coating systems have predominantly focussed on sharp nanostructures (Donaldson *et al*, 2006; Poland *et al*, 2008; Warheit *et al*, 2004; Miyawaki *et al*, 2008), nanoparticles (Kim *et al*, 2010., Yoksan and Chirachanchai,

2010., Das *et al*, 2011., Yang *et al*, 2011) or the release of silver salts directly from the surface itself (Williams *et al*, 1989). Although silver salts are known to be highly antimicrobial, they can often react and form complexes with biological fluids. The release rates are also difficult to control (Sant *et al*, 1999). Similarly, silver nanoparticles have shown a high antimicrobial activity but have been found to be potentially toxic to mammalian cells (Braydich-Stolle *et al* 2005). It can also be difficult to control the release of nanoparticles from surfaces, which can escape and accumulate in the environment causing potential problems. It is the consideration of the antimicrobial activities of silver and the challenges of using it effectively without toxicity, that have led to the antimicrobial activity of thin-film silver nanostructures being examined in this work. In the past decade, the suggestion has been made that silver nanostructures have great potential in biomedical applications, particularly as antimicrobials, due to the interactions that can occur between the nanoscale architectures and biological interfaces (Hornebecq *et al*, 2003; Carja *et al*, 2009). There are however many fundamental issues that need to be addressed in the investigation of nanostructured surfaces for antimicrobial films, including; the antimicrobial activity against model microorganisms with different cell envelope structures; the optimal thickness and film structure; the stability of the films in contact with different media; the conditions that foul the surfaces and render them inactive; the rate and level of surface oxidation, and the capability to clean and regenerate the surfaces. These challenges are not insignificant and have resulted in scientific and health drivers to understand the activity of, and produce thin-film silver surfaces that have a high antimicrobial activity but are non-toxic to mammalian cells.

At this time, the influence of nanoscale structuring and surface roughness of silver films at the nanometre scale has not been examined for antimicrobial activity. It is with this in mind that the physical vapour deposition (PVD) technique of thermal evaporation with oblique angle deposition was used for the production of silver thin-films. Oblique angle deposition was used as it can produce different nanostructures and surface roughnesses based on the angle of incidence of the deposited material onto a susbtrate (van Dijken *et al*, 2000; Park *et al*, 1995; McMichael *et al*, 2000; Wolfe *et al*, 2001; Bubendorff *et al*, 2006; van Dijken *et al*, 1999; van Dijken *et al*, 2000 and van Dijken *et al*, 2001).

1.2. Thesis Outline

Chapter 2. Theory

This chapter describes the production and characterisation of nanostructured thin-films by thermal evaporation using oblique angle deposition. Characterisation of thin-film thickness, surface roughness and post-evaporation surface changes is also considered using the analytical techniques of Rutherford Backscattering, ellipsometry, atomic force microscopy, quartz crystal rate monitor and scanning electron microscopy.

Bacterial interactions with silver surfaces (nanostructured, nanoparticle and ionic) are examined alongside antimicrobial mechanisms. Aspects of bacterial cell envelope biochemistries are investigated with regard to antimicrobial activity of the silver surfaces.

Finally, the background theory of cleaning biologically fouled surfaces is investigated, as a method of regenerating the surface.

Chapter 3. Materials and Methods

This chapter details the materials and methods for production and characterisation of nanostructured silver thin-films deposited by thermal evaporation. It also describes the methods of determining surface roughness, film thickness, post-deposition changes and material desorption.

Biological methods are given for growing *E. coli* and *S. aureus* in broths, and the subsequent determination of solution and surface based antimicrobial activity.

Chapter 4. Results and Discussion: Nanostructured Thin-Films

This chapter introduces the results from thin-film fabrication and physical characterisation, examining surface roughness, film thickness, post-deposition changes and material desorption.

Chapter 5. Results and Discussion: Bacterial Interactions with Fabricated Surfaces

This chapter examines bacterial interactions with the nanostructured thin-film surfaces. This is carried out for nanostructured chips incubated in bacterial broths to determine solution antimicrobial effects, and by incubating bacteria directly on the surfaces to examine the effect of direct contact. Silver losses from the surfaces are also measured for antimicrobial activity.

Chapter 6. Results and Discussion: Results and Discussion – Surface Cleaning and Antimicrobial Activity

The effect of simple and low cost chemical cleaning is examined in this chapter, alongside physical changes to the nanostructured surfaces and potential changes in antimicrobial activity.

Chapter 7. Conclusions

This chapter draws together all of the theoretical and experimental work in this thesis to show that nanostructuring enhances antimicrobial activity of silver thin-films.

Chapter 8. Future Work

This chapter recognises the limitations within this study and suggests future work that could be carried out to validate conclusions drawn from this study.

References

Appendix

This section contains experimental biological data where appropriate.

Chapter 2. Theory

In this chapter, the theory of thin-film fabrication and characterisation, silver as an antimicrobial and thin-film cleaning were examined.

Thermal evaporation as a method of inducing nanostructured thin-films is described. This is alongside methods to characterise the surfaces, including, atomic force microscopy, Rutherford backscattering, ellipsometry and scanning electron microscopy, which showed surface roughness, thin-film thickness, and nanoscale topography of the surfaces. The theory of inductively coupled plasma mass spectrometry was also investigated as a method to determine the loss of ionic or nanostructured silver from the thin-films.

The relationship between bacterial cells and their cell envelope structures (Gram positive and Gram negative) to disease were examined, with the use of optical density and cellular staining methods to measure cell population growth and antimicrobial activity, respectively. In particular, the use of silver in ionic, thin-films and nanoparticulate forms was considered as an antimicrobial against both bacterial cell envelope types.

Surface cleaning of biologically fouled surfaces was investigated, as a method to regenerate the surface for continued usage. This was with the rationale of simplistic and low-cost cleaning methods that do not require skilled operators.

2.1. Thin-Film Fabrication and Characterisation

Thin-film technology is based upon the production of sub-nanometre to micrometre sized continuous layers. The study and use of thin-film materials has been driven largely by the development of new material growth and characterisation techniques (Martin *et al*, 2010). This has allowed thin-films to be used in a myriad of technologies, including but not limited to: photovoltaics (Herrero and Guillén, 2004), gas sensors (Miyata *et al*, 2003), transistors (Shin *et al*, 2008), biosensors (Bai *et al*, 2011) and antimicrobials (Ghosh *et al*, 2010). Commonly perceived advantages of thin-films are often technology specific but can be based on increasing the surface to volume ratio, creating nano- or micrometre sized structures, coatings and economies of scale.

In this study, silver was examined as an antimicrobial thin-film coating on the rigid substrate of silicon dioxide. The use of high value metals such as silver can offer great economic savings when used as thin-films. When looking at the trend for the commodity value of silver, it has risen by over 490 % since 1960 (London Daily, 2011), which is well above levels of inflation. This issue has the potential to make the use of bulk-scale silver prohibitive in comparison to thin-film technology. Taking a simple hypothetical example, converting a millimetre coating of silver to a nanometre coating approximately reduces the material cost to a millionth of the bulk.

2.1.1. Thin-Film Formation

Thin-films can be deposited using a wide variety of chemical and physical techniques. The two main approaches to deposition are chemical vapour deposition (CVD) and physical vapour deposition (PVD). Many factors need to be examined for the type of material to be deposited. Such factors include, the purity of material to be deposited, its chemical and physical nature, the interaction between the substrate and the material, level of vacuum required (if at all), rate of thin-film formation, desired topography, density and thickness of the thin-film.

Three significant thin-film growth modes are recognised, namely: (1) Volmer-Webber (island) growth, (2) Frank-Van der Merwe (layer-by-layer) growth, and (3) Stranski-Krastanov growth (see figure 1). Volmer-Weber island growth occurs as a result of the smallest stable clusters nucleating on the susbtrate and growing into three-dimensional island structures. This type of structure is due to the adsorbing atoms or molecules being more strongly bonded to each other than the substrate. Depositing materials with a higher surface free energy than the substrate, form these structures to minimise the surface energy. The opposite characteristics to Volmer-Weber growth are shown in Frank-Van der Merwe growth, where the deposited material has a lower surface free energy than the substrate. This growth occurs from deposited material growing two-dimensionally, as the deposited material is more strongly bound to the substrate than to other deposited atoms or molecules. Ideally planar sheets are formed, with each successive layer being less strongly bonded to the layer beneath until the bulk bonding strength is reached. The final growth mechanism is termed Stranski-Krastanov, and can be considered a mixing of Volmer-Weber and Frank-Van der Merwe mechanisms, as it contains initial planar growth and island growth. In this type

of growth, the depositing material forms one or more monolayers, until further growth becomes energetically unfavourable due to layer thickness creating strain and resulting in the interface energy increasing (Eastwood, 2010). This leads to island growth.

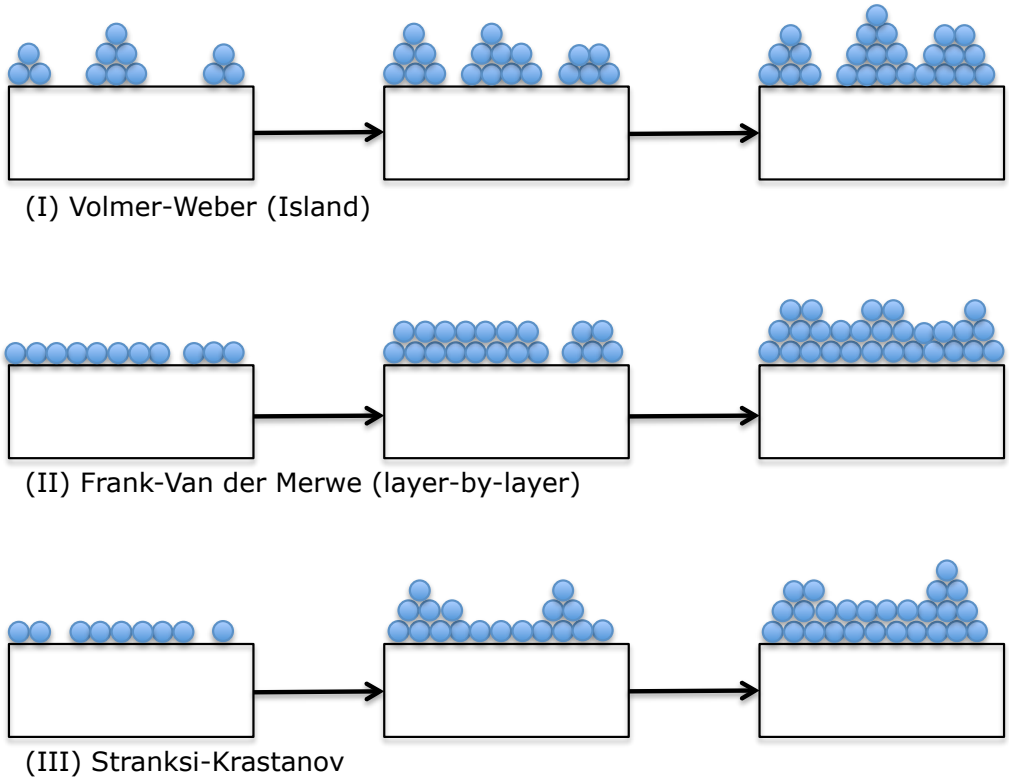

Figure 1. Diagrammatic representation of the three methods of thin-film growth, including: (I) Volmer-Weber (island) growth, (II) Frank-Van der Merwe (layer-by-layer growth) and (III) Stranski-Krastanov, layer then island formation. This diagram was modified from Martin et al., 2010.

2.1.2. Thermal Evaporation

Thermal evaporation (figure 2) is a PVD technique that is relatively simple and can produce multi-layered sub-nanometre thin-films. The process is carried out under vacuum to reduce thin-film defects and contamination, which is particularly the case

for materials such as silver and chromium, which can easily undergo oxidation in ambient and non-vacuum conditions. To evaporate material, a crucible is heated by current (used in this study), or an electron beam can be applied locally to create a liquid phase with a vapour phase above. Upon atomisation, the material moves freely in the high vacuum where it may come into contact with the substrate and be deposited. Control over the rate of material atomisation, and thin-film deposition, is controlled by altering the heating or electron beam. A quartz crystal rate monitor, located in the chamber alongside the substrates, is used for measurement of thin-film deposition rate and thickness. In this study, an angled substrate holder was used for all depositions. The angled substrate holder was fabricated in house, with a goniometer being used to measure the angle of each substrate holder.

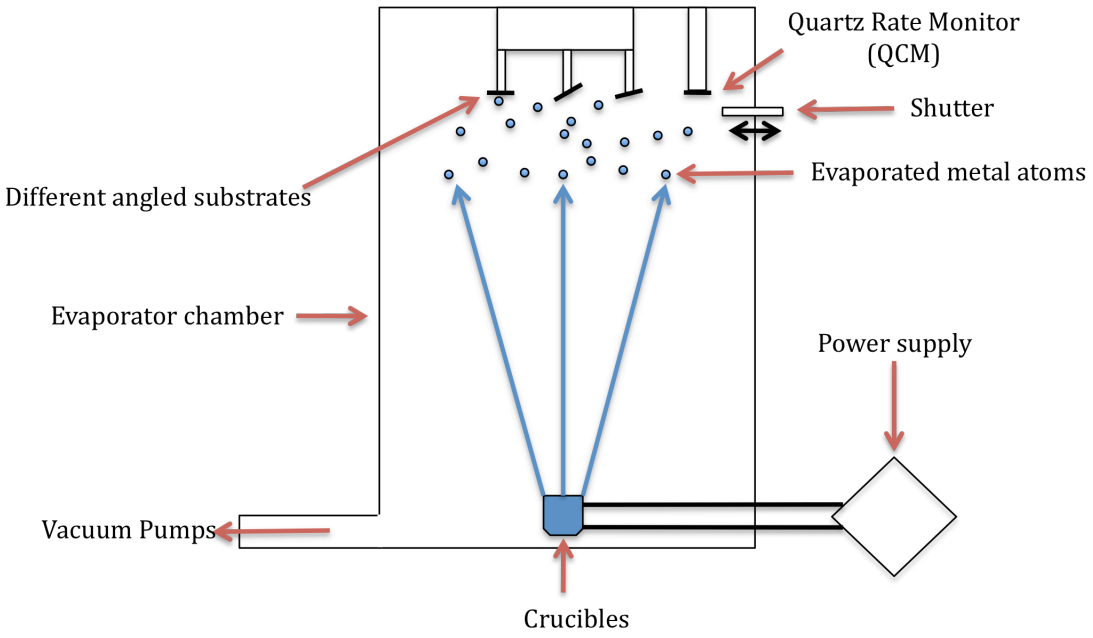

Figure 2. Diagrammatic representation of a thermal evaporator. Material is shown being atomised and forming thin-films on different angled substrates and on a quartz rate monitor.

2.1.3. Surface Roughness

'All surfaces are rough, though perfect crystals are rough only at the very small scale of intra-lattice distances' (Neogi, 2006). The roughness of a sample can be divided into surface roughness and internal inhomogeneity (Glover *et al*, 2009). Of particular interest to this study is surface roughness, which is a measure of the variability in surface height across a sample and is routinely studied using techniques such as, optical profilometry (Poon and Bhushan, 1995), atomic force microscopy (AFM) (Bennett, 1992), scanning tunneling microscopy (STM) (Binnig, 1986), transmission electron microscopy (TEM) (Chládek *et al*, 1996), scanning electron microscopy (SEM) (Schwander *et al*, 1995), and X-ray reflectivity (Spiller *et al*, 1993).

2.1.4. Inducing Surface Roughness

The deposition process and growth of thin-films can lead to the formation of roughened surfaces. Uncovered substrate and boundaries between islands of growth can lead to defects in crystal structure, which as successive atom deposition occurs, results in increased roughness. Surface roughness is therefore related to the size of material grain formed, with larger grain sizes resulting in higher amplitude surface roughness. There are numerous methods of inducing surface roughness, including thermal evaporation (Gupta *et al*, 2009), electron beam lithography (Georgiev *et al*, 2004) and sputtering (Wang *et al*, 2003), amongst others. Of particular interest to this study are methods using oblique angle deposition (Hadley *et al*, 2002; Alameda *et al*, 1996; van Dijken *et al*, 2000). The use of this type of deposition on flat substrates has been well studied for the production of nano-scale anisotropic structures and

roughness (van Dijken *et al*, 2000; Park *et al*, 1995; McMichael *et al*, 2000; Wolfe *et al*, 2001; Bubendorff *et al*, 2006; van Dijken *et al*, 1999; van Dijken *et al*, 2000 and van Dijken *et al*, 2001).

Oblique angle deposition growth results in surface roughness through the formation of ripples or elongated islands (Politi *et al*, 2000), with numerous theoretical studies explaining elongated island growth at oblique angle deposition (Bubendorff *et al*, 2009). Molecular-dynamics simulations (Luedtke and Landman, 1989) showed that deposition at oblique angles created a shadowing and deflective effect for thin-film growth, whereby incident atoms/molecules induced columnar structures and increased surface roughness. It is believed that shadowing, results in given points in a surface receiving fewer adsorbing atoms/molecules due to nucleated structures blocking incoming material. Deflection of incident atoms/molecules means that long-ranged attractive forces create a redistribution of incoming material over the surface (van Dijken *et al*, 2000; van Dijken *et al*, 1999; van Dijken *et al*, 2000; Luedtke and Landman, 1989; Amar, 2003) and is highly suited to this work as it is a relatively simple single step process that can produce nanoscale structuring over relatively large areas.

For thin-film growth, approaching atoms have been found to deposit on the top of Volmer islands even at normal incidence (known as steering), which increases at oblique incidence (van Dijken *et al*, 1999 and van Dijken *et al*, 2000). Therefore the thin-film surface has an increased roughness in the direction parallel to the incidence of atomic flux (Bubendorff *et al*, 2009). Theoretical and practical work using copper by Amar (2003) and Bubendorff *et al* (2009) with normal incidence and oblique

angles up to 55 degrees from the surface normal has shown that steering has a negligible effect on the trajectory of incoming particles. For angles above 55 degrees however, steering can become significant. Short-range attraction can also result in adsorbing atoms being attracted towards the upper terrace instead of the lower terrace (Bubendorff *et al*, 2009). This also can lead to increased surface roughness, which is amplified with oblique angle deposition (Yu *et al*, 2002). The effect of steering and shadowing, both lead to an increased surface roughness, particularly when oblique angle deposition is used as a fabrication method.

2.1.5. Calculating Surface Roughness

Determination of surface roughness is necessary for understanding how biological materials interact with surfaces. This is particularly relevant for understanding bacterial adhesion to surfaces and the mechanism of surface antimicrobial activity (Méndez-Vilas *et al*, 2006). Measuring surface roughness is not without challenge, as samples can have different amplitudes and spatial variation or wavelength and yet still have the same surface roughness. For biological interactions with thin-films, this has the potential for two structurally different surfaces to interact in different ways with biological materials, but having the same surface roughness. There are numerous measures of surface roughness but in biomedical research (Santiago *et al*, 2005; Ungersböck and Rahn, 1994) it is commonly calculated by average roughness (R_a) or the root mean square (RMS), as shown in equations 1 and 2.

$$R_a = \frac{1}{N}\sum_{i=1}^{1}\left|Z_i - \overline{Z}\right| \qquad (1)$$

$$\mathrm{RMS} = \sqrt{\frac{\sum_{i=1}^{N}\left(Z_i = \bar{Z}\right)^2}{N}} \qquad (2)$$

Where z_i is the height of the ith point with respect to the lowest one in the image and N is the total number of points in the image.

Many parameters have been introduced for the quantification of roughness amplitude and spatial distribution (Stout *et al*, 2003 and Valkonen, 1987). For simple approximations of roughness, it is generally accepted that most of the traditional parameters are related by linear relationships (Stout *et al*, 2003 and Valkonen, 1987; Nowicki, 1985), which means that only a few roughness parameters are required (Choi *et al*, 2007). Difficulties can arise however, from these roughness parameters not being influenced by spatial distribution or roughness amplitude (Choi *et al*, 2007). Work by Stoudt and Hubbard (2005), showed that two roughness profiles having different spatial roughness patterns can have the same surface roughness, when calculated by a technique such as R_a. This finding shows the importance of utilising the most appropriate calculation for surface roughness. In this study, RMS roughness is used as a method for defining the AFM derived surface roughness. It is not suggested as the only method for calculating surface roughness produced by thermal evaporation. It is however one of the most widely used calculations used for surface roughness (Choi *et al*, 1997) and is a useful proxy to indicate differences between the different surfaces produced in this work, although as shown later the nanostructured surfaces resulting from the highest angle deposition do not show simply increased roughness.

2.1.6. Material Measurements – Analysis Techniques

In this section, the functionality of the analytical techniques used to investigate the physical state of the thin-films is described.

2.1.7. Atomic Force Microscopy

The AFM (Binnig *et al*, 1986) is a scanning probe microscope where a sharp tip forming part of a cantilever, shown in figure 3 (mounted on a piezoelectric transducer) can be moved in the *x-y-z* dimensions by piezoelectric controllers (as shown in figure 4).

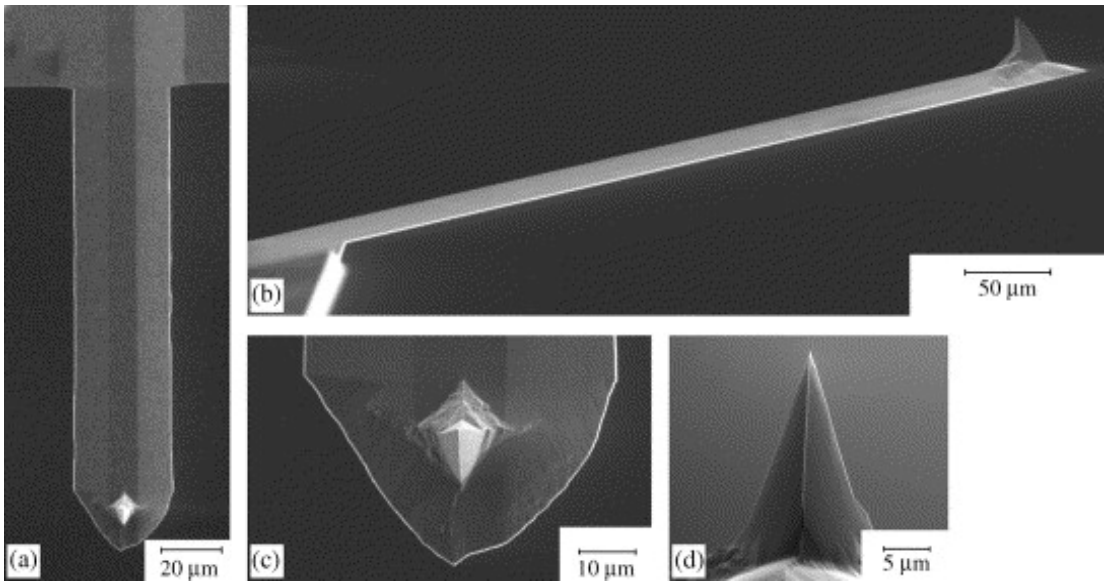

Figure 3. Scanning electron microscope images of AFM cantilevers and tip. (a) Plan view, (b) side view images, (c) close-up of the end of the cantilever and (d) side view of the AFM tip (Kopycinska-Müller et al., 2006).

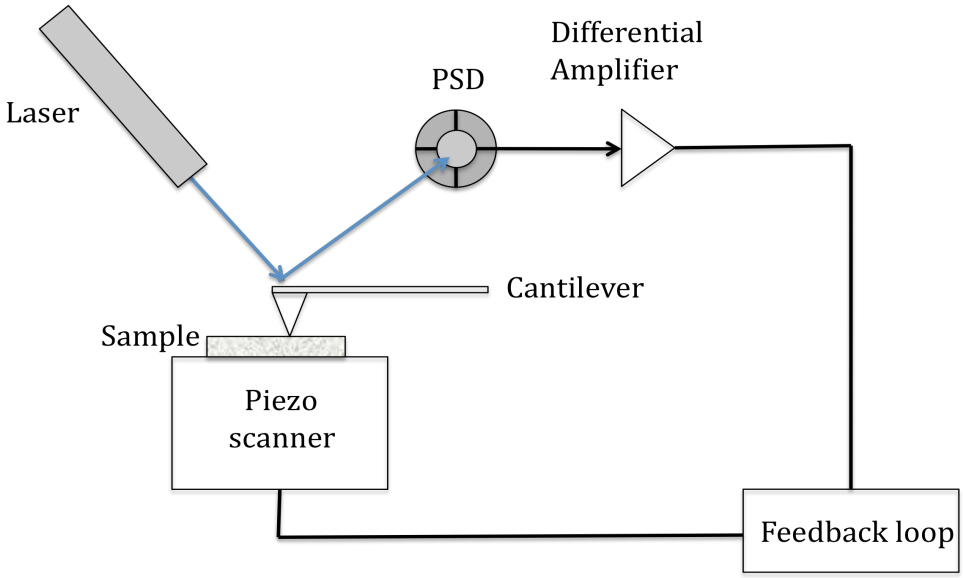

Figure 4. Schematic of an Atomic Force Microscope. A sample is shown being scanned by an AFM tip, which is attached to a micro cantilever, which in turn is mounted on a piezoelectric transducer. The resulting force between the tip and sample is measured by deflection of the cantilever. Surface topography is produced by plotting cantilever deflection against the position of the probe tip.

The sample surface consists of user-defined points for each tip measurement in the *x*-*y*, with each point having a voltage coordinate in the *z* dimension. An image is created by rastering the tip across the sample surface, which results in a voltage for each *x*-*y* coordinate being obtained as the tip is brought into contact or close contact to the surface (Allison *et al*, 2002). This is achieved by probe-sample interactions creating cantilever deflections. Such deflections are commonly monitored by an optical detector using the optical lever technique (Meyer & Amer, 1988; Alexander *et al*, 1989). This is based upon a diode laser being focused on to the cantilever and the reflected beam position is monitored using a four-quadrant position sensitive detector (PSD). As force is applied to the tip, the cantilever will bend which in turn will change the position where the laser strikes the PSD (Butt *et al*, 2005), which in turn changes the ouput voltage of the PSD. At this point, a feedback loop is employed by

application of voltage to the piezoelectric which results in cantilever retraction from the surface, cantilever relaxation and re-alignment of the laser to its original position on the PSD (Allison *et al*, 2002). AFM has found wide usage in measuring surface roughness, such as in this work, with an example being shown in figure 5.

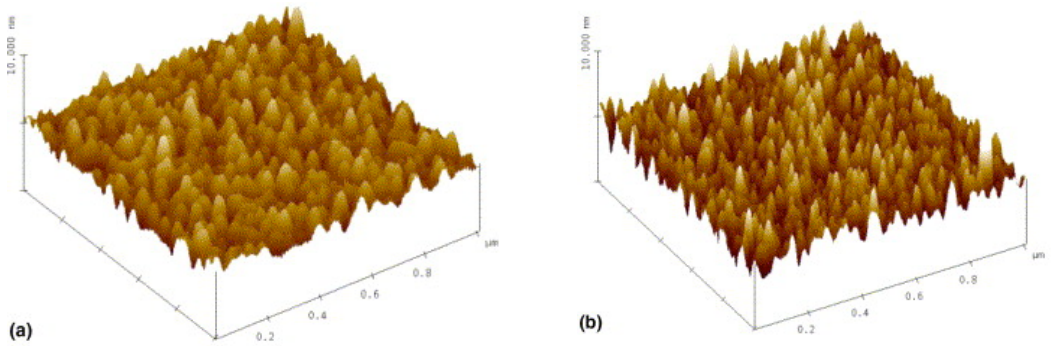

Figure 5. AFM scans of surface roughness. In this example study, copper was seeded on silicon dioxide over a 200-hour period, and showed increased surface roughness when measured in tapping mode (Brunoldi et al, 2005).

Microcantilever properties are of critical importance for surface imaging, with length, width, thickness and shape having an effect on the ability to image (Frederix *et al*., 2003). Typically cantilevers are in the micrometre range but with the use of smaller cantilever dimensions, an increase in cantilever resonance frequency is observed which can lead to an increase in force sensitivity.

The resolution of three-dimensional AFM images depends upon both the lateral (*x*-*y*) and vertical (*z*) resolutions. Each resolution is limited by AFM machine induced noise and thermal fluctuations of the cantilever. However, with the use of damping systems, the largest source of noise is thermal and is invariably associated with the cantilever noise (Garcia and Pérez, 2002).

Image resolution is also affected by the size of the tip, which is often responsible for increased apparent width in measurements. Simplistically, the tip used must be smaller than the object being measured to obtain sample images closer to the actual width (Keller and Franke, 1993). Lateral resolution is also limited by the strength of tip-surface attraction forces, which has been shown for high attractive forces and/or non-rigid samples, often leading to a reduction in resolution (Garcia and Pérez, 2002). The converse of this has also been shown to be true, with the use of low tip-surface forces and a rigidly bound sample leading to an increase in resolution (Möller *et al*., 1999). For surface roughness measurements, image resolution is of great importance as is the requirement to measure surface roughness and not effects such as ringing. Ringing related artifacts can result in false surface roughness and can occur due to various factors, particularly where sudden height changes occur. For small tips, ringing artifacts can occur from tip bending, adhesion and stiction to surfaces (Strus *et al*, 2005). This is more likely to occur at the bottom of high aspect ratio structures, where the tip-trench stiction and controller reaction to the resulting force increase is measured by the controller as a topography change (Strus *et al*, 2005). This can be particularly problematic at low scan speeds, where ringing can introduce artifacts into the image, which may be mistaken for surface roughness (El Rifai and Youcef-Toumi, 2001). Strus *et al* (2005) suggested that increasing the driving amplitude, lowering the integral gain, can reduce ringing artifacts and ensuring correct tip alignment.

The three main modes of microcantilever operation used to image and manipulate surface topography include: contact (C-AFM), non-contact (NC-AFM) and tapping mode (T-AFM). The three modes are distinguished by the frequency of

microcantilever oscillation, relative distance between tip and surface as well as interactive forces that occur between sample and tip.

In C-AFM, the tip is maintained in constant contact with the sample as it raster scans across the surface (Fung and Huang, 2002). As the tip scans, the forces between tip and sample are predominantly repulsive, and dominated by Van der Waals, which is due to electron clouds between atoms in the tip and surface repelling each other. Van der Waals however, are not the only forces that act upon the tip, with two others including, the shear force exerted by the microcantilever and the capillary force of any contaminant layer over the surface. Under most laboratory conditions a contaminant layer will form over the sample, which will have a constant attractive capillary force on the tip in a homogenous contaminant layer. The magnitude of microcantilever forces however is dictated by the deflection and spring constant of the microcantilever (Jalili and Laxminarayana, 2004) but is also affected by the contaminant layer.

Using C-AFM, two scanning modes are available: constant height and constant force mode. In constant height, the piezo-controller holds the tip at a known (z) height above the surface. This allows, microcantilever deflection to map the surface topography based upon tip-sample interactions but has the potential of damaging the surface by tip crashes. This is especially the case, where the surface is far from flat and/or has irregularities. This problem is addressed in constant force mode, where the force between tip and sample is kept constant via piezo-controller feedback. As the tip is brought to the surface, piezo-controller feedback is used to keep the tip at and in contact with the surface. The microcantilever deflection is monitored by the PSD, with deflections in the x-y being converted into a surface topography. A disadvantage

of the constant force mode is that resulting shear forces from the microcantilever can potentially damaging soft samples and/or distort soft surface features.

In NC-AFM, the tip is brought close to the surface (tens of nanometres away) and the microcantilever is oscillated near its natural resonance frequency resulting in tip movement a couple of nanometres in the *z* dimension (Basso *et al*, 1998). At this frequency, tip surface interaction occurs in the Van der Waals regime. As the tip rasters across the sample surface the vibrating tip weakly interacts with the surface, with resulting changes in oscillation being recorded. The use of this mode enables many of the problems encountered with contact mode to be eradicated. In particular, this mode of AFM has proved to be very successful for imaging soft samples, including: SAMs (Tanaka *et al*, 2006), liquids (Checco *et al*, 2006), bacteria (Méndez-Vilas *et al*, 2004), hydrogels (Kim *et al*, 2001) and biomolecules (Maeda *et al*, 1999). Disadvantages of NC-AFM are often based on a lower resolution of image as a consequence of the tip being a greater distance from the sample.

T-AFM can almost be regarded as combining various aspects of C-AFM and NC-AFM. This is due to the microcantilever being oscillated near its natural resonant frequency, which allows the tip to regularly impact the surface for a limited time period (Salapaka and Chen, 1998). The force applied to the microcantilever creates a vibration that moves the tip between 20-100 nm when not in contact with the surface. As the tip is brought closer to the surface, the tip begins to lightly tap the surface being imaged. Throughout surface imaging, the tip taps the surface and lifts off alternatively at frequencies between 50-500 k cycles/s (Jalili and Laxminarayana, 2004) with the oscillation amplitude being kept constant via a feedback loop. When

the tip contacts the surface, a loss of energy is observed resulting in a reduction in amplitude according to surface topography. This is shown upon the tip moving over a surface feature with increased height, which leads to a decrease in vibration amplitude to a reduction of space for tip vibration. The converse of this effect is shown whereby an increase in vibration amplitude occurs when the tip moves over a trough, allowing the tip to move to its free amplitude. Changes in amplitude are detected by the PSD and are relayed and compared to reference values, using a piezo-controller in a feedback loop to regulate the height of the tip from the sample surface. Image generation is carried out by differences between the amplitude reference and actual tip values, which are then converted into surface topography. Again, the use of this mode allows many problems associated with C-AFM to be overcome such as friction and adhesion, thus allowing high resolution imaging of soft samples.

2.1.8. Rutherford Backscattering

Rutherford Backscattering (RBS) is an ion accelerator technique for compositional depth measurements of thin-films (figure 6). It was originally developed by E. Rutherford in 1911 and was first described as a technique for thin-film analysis by Rubin *et al* (1957). RBS is quantitative, when used with reference samples and is non-destructive.

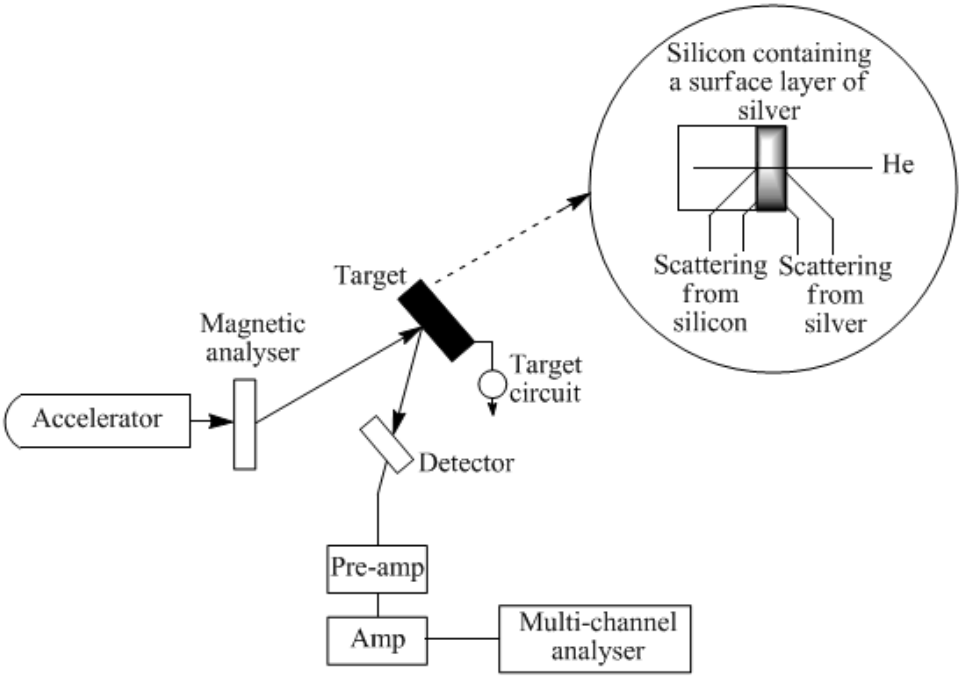

Figure 6. Schematic of a Rutherford Backscatter system, showing ions being accelerated towards a sample.

The principle of RBS is that a mono-energetic beam of light ions, such as helium, are directed onto a sample where they penetrate the sample and lose kinetic energy, due predominantly to interactions with electrons. However, when ions approach the atomic nuclei in the sample, the repulsive coulomb forces scatter the ions at large angles, (as shown in figure 7). Some of these ions leave the sample and are detected

by a silicon solid-state detector and their energies analysed. Backscattered ions create electron hole pairs in the detector, which are separated by an applied electric field, which in turn creates a charge pulse. The number of electron hole pairs created is proportional to the ion energy (Williams and Möller, 1978). Resolution of silicon detectors is limited by statistical fluctuations for energy transfer to electrons and phonons, as well as statistical fluctuations in the annihilation of electron-hole pairs (Williams and Möller, 1978). Detector resolution can be increased by changing the detector type to an electrostatic or magnetic analyzer, but they are often much larger and more expensive.

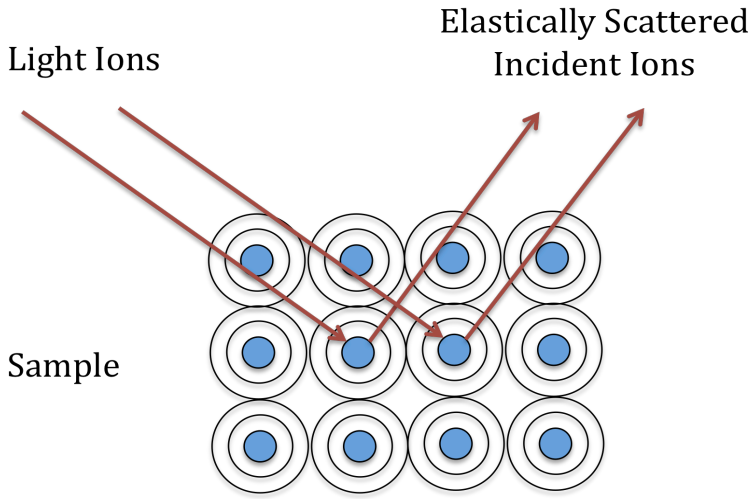

Figure 7. RBS ion interaction with a surface. Light ions are shown penetrating into a sample of atoms and the ions being elastically scattered upon contact with atomic nuclei, where they will be detected.

The energy of the backscattered ions is dependent upon the depth of collision in the material and on the mass of the scattering nucleus. Simplistically, RBS can be considered to be an elastic collision between a high kinetic energy particle from the incident beam and a stationary particle (in the atomic nucleus) in the sample. The kinematics of the collision shows that the energy of the scattered object is reduced from the initial energy E_0 to E_1, see equation 3 (Williams and Möller, 1978).

$$E_1 = k \times E_o \tag{3}$$

Where E_1 is the energy of the scattered ion, E_0 is the initial energy of the incoming ion and k is the kinematic factor. The kinematic factor k (which characterises the target atomic nuclei) can be defined as the ratio of energies before and after scattering and is shown in equation 4 (Williams and Möller, 1978).

$$k = \frac{E_{scattered}}{E_{incident}} \left| \frac{\left(1 - \left(M_1 \operatorname{Sin} \theta\right)^2\right) + \frac{M_1 \cos \theta}{M_2}}{1 + \frac{M_1}{M_2}} \right|^2 \tag{4}$$

Where k is the kinematic factor, θ is the scattering angle, M_1 is the incident ion mass, M_2 is the target nucleus mass and E refers to the energy of the incident ions and scattered ions.

Detector resolution, energy straggling, multiple scattering, surface roughness and geometrical effects determine the depth resolution of RBS. Considering a standard RBS experimental setup using 2 MeV He^+ backscattered through a 150 ° solid-state detector with an energy resolution of 15 keV, a depth resolution of 300 Å could be attained (Williams and Möller, 1978). An example RBS trace is shown in figure 8.

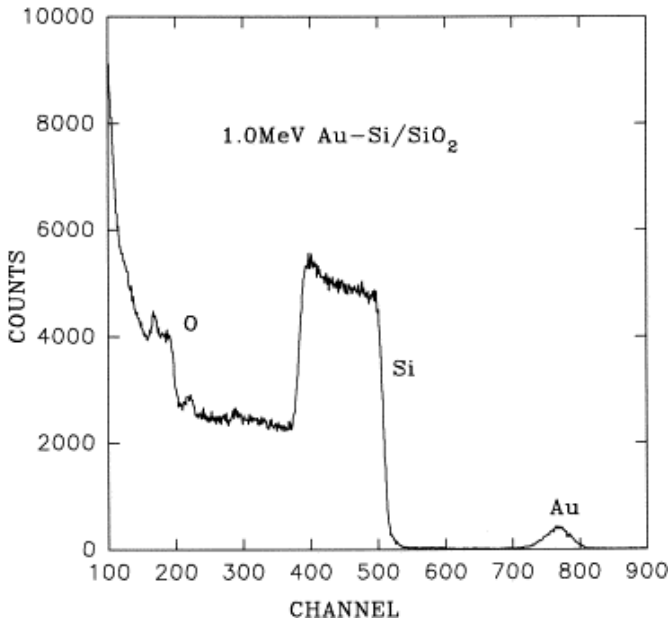

Figure 8. RBS spectrum of 1.0 MeV Au^+ implanted into amorphous Si film on silicon dioxide susbtrate (Wang et al, 1999). Channel refers to incoming ions being aligned with a major crystallographic direction, which reduces the backscattered yield, as incoming ions are guided into the plane. Information is given on the quality of the crystal and possible defects and contaminants.

2.1.9. Ellipsometry

The term ellipsometry was first used by Rothen (1945) and is an optical technique that is well suited for the measurement of surfaces and coating layers and is based on the polarisation transformation that occurs as a beam of polarised light is reflected from or transmitted through a film. It is particularly suited to thin-film analysis as it is essentially non-perturbing and is sensitive to the formation of sub-monolayer thicknesses (Azzam and Bashara, 1977).

The basic set-up of an ellipsometer is shown schematically in figure 9, where a monochromatic light source passes through a polariser, to produce a beam of known polarisation. The beam subsequently interacts with the sample surface and is reflected,

refracted, transmitted or scattered. After interaction with the sample, the state of the polarised light beam is analysed with a variable polarisation analyser and photodetector.

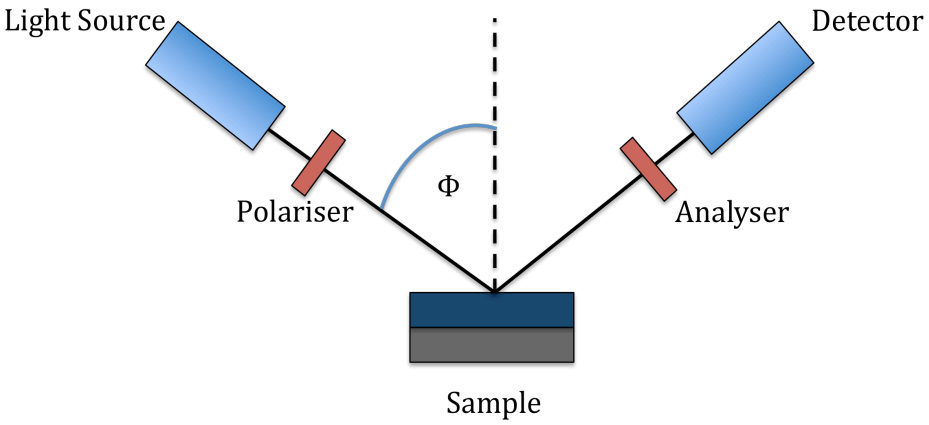

Figure 9. Schematic of an ellipsometer, showing the generation of a beam of polarized light, the polarization, the interaction with a surface, reflection of the light through an analyser to a photo-detector.

Invariably, ellipsometry involves the reflection of light (containing either electric fields parallel (*p*-) or perpendicular (*s*-) to the plane of incidence) from a surface. Contrary to popular belief the technique does not measure the thickness of a sample but measures the quantities Δ and Ψ, that describe the change in polarisation that occurs when a measurement beam interacts with a sample. Upon interaction of the measurement beam with the surface, the surface differentiates between the *p*- and *s*-light, causing a change in the outgoing polarisation. Δ is the change in phase difference that occurs upon reflection and it can have a value between 0 º to 360 º and is represented simplistically by equation 5 (Tompkins, 1993):

$$\Delta = \delta_1 - \delta_2 \qquad (5)$$

Where Δ is the difference in phase that occurs upon reflection, δ_1 is the difference between the parallel component and perpendicular component of the incoming wave and; δ_2 is the difference between the parallel component and perpendicular component of the outgoing wave.

Ψ is the angle whose tangent is the ratio of the magnitudes of the total reflection coefficients, which can be between 0 º to 90 º and is shown in equation 6 (Tompkins, 1993):

$$\tan \Psi = \left| \frac{R_p}{R_s} \right| \tag{6}$$

Where R_p and R_s are the Fresnel reflection coefficients for the p- and s- polarised light, respectively.

The change in polarisation (ρ), in the ellipsometry measurement is shown in equation 7 (Tompkins, 1993):

$$\rho = \tan (\Psi) e^{i\Delta} \tag{7}$$

Some of the main advantages of this technique are the non-destructive and simple methodology, which allows samples to be rapidly loaded and measured.

2.1.10. Piezoelectric Quartz Crystal Mass Measurement

Piezoelectric quartz crystal measurements are used to measure ultra low mass loading for applications such as thin-film growth. They have also found use in real-time measurements of biological interactions with thin-films deposited onto quartz crystal surfaces.

The Rayleigh hypothesis states "resonance in a mechanical system occurs at frequencies at which the peak kinetic energy U_k exactly balances the peak potential energy U_p" (Rayleigh, 1885). This results from the fact that energy is exchanged between kinetic and potential forms at resonance. When mass is adsorbed to the crystal surface, an increase in kinetic energy occurs, with no change in potential energy. To redress the energy change resulting from mass adsorption, the resonant frequency of the crystal changes, which acts to rebalance the kinetic and potential energies.

The peak kinetic energy density in the piezoelectric crystal occurs at the moment when particle velocity is maximum and displacement is zero as shown in equation 8 (Ballentine *et al*, 1997):

$$U_k = \frac{\omega^2 u^2_{xo}}{2}\left(\rho_s + \frac{\rho_q h_s}{2}\right) \tag{8}$$

Where ρ_s is the mass per surface area unit of quartz, ω is the angular frequency, ρ_q is the mass per unit volume of quartz, h_s is the thickness of crystal and u is the component of displacement.

The peak potential energy however occurs at the moment that displacement is at a maximum and velocity is zero, as shown in equation 9 (Ballentine *et al*, 1997):

$$U_p = \frac{1}{2}\,\mu_q k^2 u^2_{xo} \int_o^h \sin(ky)\,dy = \frac{\mu_q k^2 u^2_{xo} h_s}{4} \qquad (9)$$

Where μ_q is the shear modulus of quartz, k is the electromechanical coupling coefficient, u is the component of displacement and h_s is the thickness of crystal.

Using the Rayleigh hypothesis, at resonance, a relationship can be derived using equations 8 and 9. This shows the relationship between piezoelectric crystal resonant frequency and surface mass density - when mass loading on the surface is zero *i.e.* $\rho_s = 0$, as shown in equation 10 (Ballentine *et al*, 1997):

$$\left(\frac{\omega_0}{\omega}\right) = 1 + \frac{2\rho_s}{h_s \rho_s} \qquad (10)$$

Where ρ_s is the mass per surface area unit of quartz, ω_o is the unperturbed resonant frequency $\left(N\pi / h_s\right)\left(\mu_q / \rho_q\right)^{\frac{1}{2}}$, ω is the angular frequency; ρ_q is the mass per unit volume of quartz and h_s is the thickness of crystal.

When the surface mass is greater than zero but no more than 2 % of the crystal mass, equation 11 can be used as a linear approximation between adsorbed mass and resulting frequency shifts (Ballentine *et al*, 1997).

$$\frac{\Delta f}{f_o} = - \frac{\rho_s}{h_s \rho_s} \quad (11)$$

Where Δf is the change in resonant frequency, f_o is the original resonant frequency of the transducer, ρ_s is the mass per surface area unit of quartz, ρ_q is the mass per unit volume of quartz and h_s is the thickness of crystal.

Combining equation 12, with Equations 13, 14 and 15 gives the Sauerbrey equation (equation 16), which is commonly used in piezoelectric crystal mass detection (Ballentine *et al*, 1997).

$$h_s = N\left(\frac{\lambda}{2}\right) \quad (12)$$

Where piezoelectric crystal thickness is determined by: N, an integer and λ is the acoustic wavelength. This equation suggests that resonance occurs at half of the acoustic wavelength.

$$f_N = \frac{N v_s}{2 h_s} \quad (13)$$

Where resonant frequency is related to the N^{th} mode, N is an integer, v_s is the shear wave phase velocity and h_s is the thickness of crystal (Ballentine *et al*, 1997).

$$V_s = \left(\frac{\mu_q}{\rho_q} \right)^{\frac{1}{2}} \tag{14}$$

Where shear wave phase velocity: where μ_q is the shear stiffness and ρ_q is the mass density (Ballentine *et al*, 1997).

$$\Delta f = - 2.3 \times 10^6 . f_o^2 \frac{\Delta M_s}{A} \tag{15}$$

Where Δf is the change in resonant frequency (Hz), f_o is the fundamental frequency of the piezoelectric crystal in MHz, ΔM_s is the mass of material that is deposited or adsorbed onto the piezoelectric crystal electrode (g) and A is the coating area (cm^2) (Sauerbrey, 1959). The application of a voltage across a piezoelectric crystal results in mechanical strain, causing a vibrational/oscillatory motion of the crystal as shown in figure 10 (Tombelli *et al*, 2005).

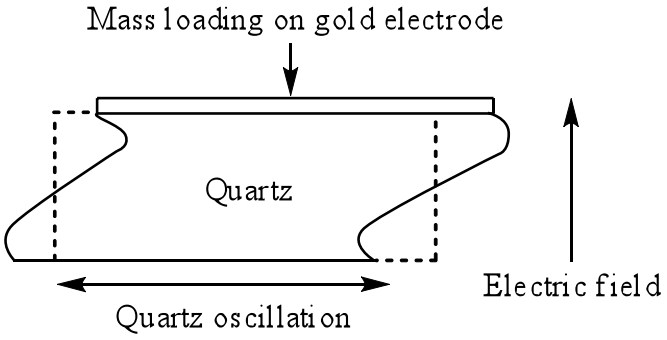

Figure 10. Piezoelectric quartz crystal operation. The path of the acoustic wave through the quartz and gold electrode is shown, with the electric field also being perpendicular.

Adsorption of any material onto the piezoelectric crystal electrode can be regarded as having increased the thickness of the electrode and thus the path length of the acoustic

waves, which consequently decreases the resonant frequency. Selectivity is therefore entirely dependent on the surface layer. This means that great care must be taken to tailor the surface chemistry to reduce the effects of non-specific binding. Soft coatings formed on the electrode will lead to viscoelastic coupling between the coating and the quartz crystal acoustic waves which means that the determination of the mass deposited can be complex. Detection of soft biomolecules can therefore be problematic.

Quartz crystal oscillators can be used in liquids, with all measurements in this study being carried out in liquid. Continuous liquid-phase operation requires the use of an appropriate oscillation circuit (Muramatsu *et al*, 1987, 1988) with only one side of the crystal exposed to the solution, to avoid short-circuiting when both sides were exposed. For the analysis of liquid-phase measurement, a number of equations have been developed, with the key amongst these being equation 16 (Kanazawa and Gordon, 1985a, 1985b).

$$\Delta f = - f_o^{\frac{3}{2}} \left(\frac{\rho_{l}\eta_{l}}{\pi \rho_{q} \mu_{q}} \right)^{\frac{1}{2}} \qquad (16)$$

Where: Δf is the change in piezoelectric crystal frequency (Hz), f_o is the fundamental frequency of the piezoelectric crystal in MHz, η_l is the viscosity of the liquid contacting the piezoelectric crystal, ρ_l is the liquid density contacting the piezoelectric crystal, ρ_q is the density of quartz and μ_q is the shear modulus of quartz (Kanazawa and Gordon, 1985a, 1985b).

Other models have been presented for liquid-based sensing (Bruckenstein and Shay, 1985) but the model presented by Kanazawa and Gordon (1985a, 1985b) is still the most widely used. One of the difficulties with solution-based detection is the increased number of factors that must be considered when taking measurements and relating frequency shifts to the binding mass. Some of these factors include; solution viscosity, viscoelastic properties of the adsorbed materials, solution temperature, solution density, interactions at the electrode-solution interface and electrode properties (e.g. roughness and coating uniformity) amongst many others. A further complication attributed to both dry- and liquid-phase measurement is that of solvent trapping within molecular layers. Using solution phase measurements, biomolecular films have been shown to have a mass ten times greater than that observed using optical measurements, which has been attributed to the binding and trapping of water molecules within the adsorbed biomolecular layer (Cho *et al*, 2004; Feiler *et al*, 2007). Liquid-phase analysis can be advantageous as it is real-time and has lower levels of solvent trapping than in the dry-phase.

2.1.11. Scanning Electron Microscopy

Scanning electron microscopy (SEM) was used to investigate the silver surfaces produced in this work. A diagrammatic representation of an SEM is shown in figure 11. The SEM produces a sample image by accelerated primary electrons being directed on to the sample produced using a tungsten filament, LaB_6 Schottky emitter or a tungsten field emission tip (‘electron gun’). Electrostatic or magnetic fields are applied at right angles to focus and control the electron beam on the sample. When the accelerated electrons enter a solid, they undergo both elastic and inelastic scattering.

The effect of these interactions creates a pear-shaped interaction volume (shown in figure 12). A Monte Carlo simulation of this is shown in figure 13.

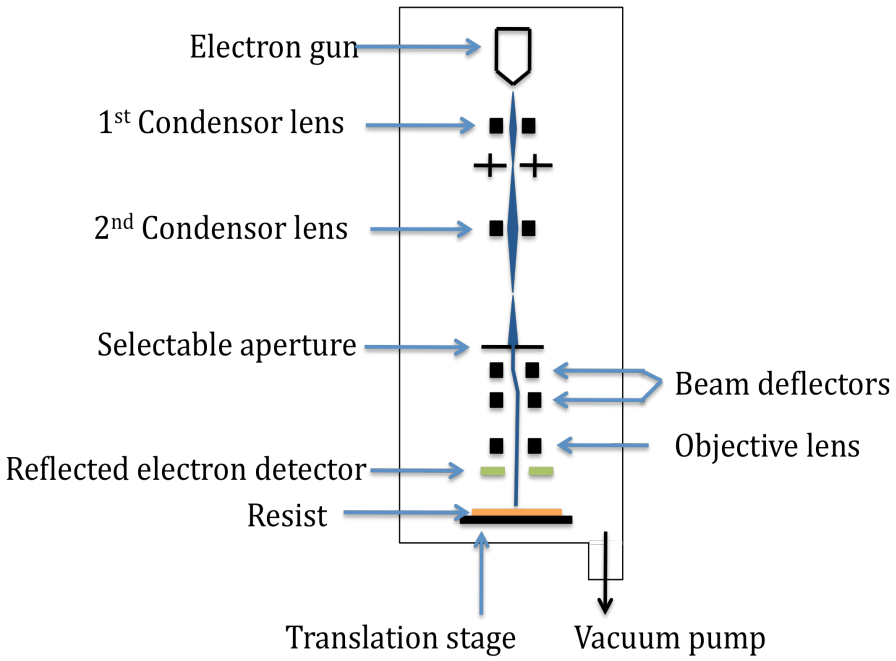

Figure 11. Schematic of a scanning electron microscope, showing primary electrons being accelerated by an electron gun, where they are focused onto a sample and detected as backscattered electrons.

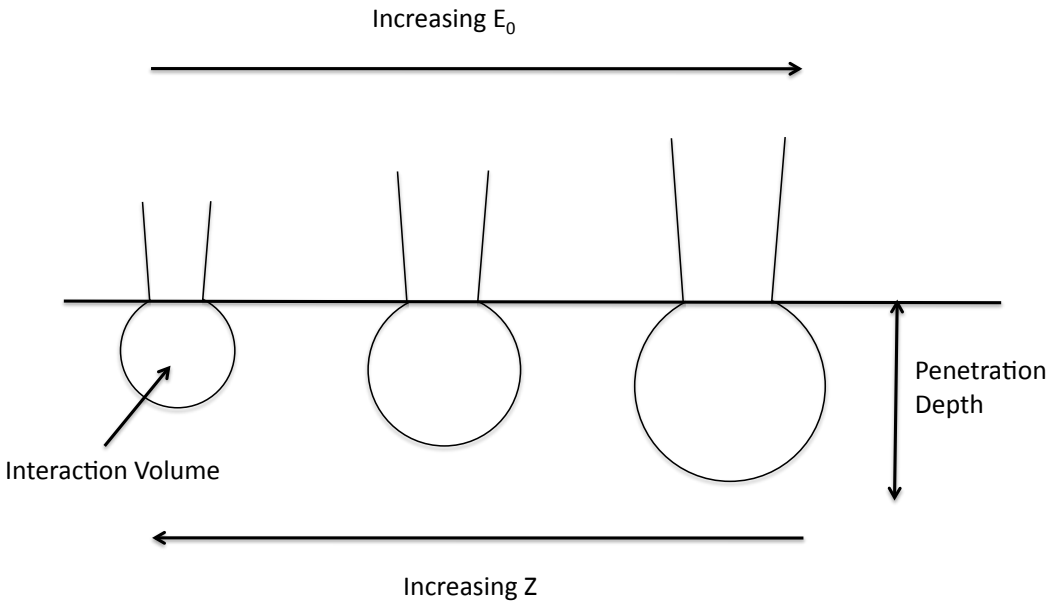

Figure 12. Schematic representation of the interaction volume and penetration depth as a function of incident energy E_0 and atomic number Z of the primary electrons.

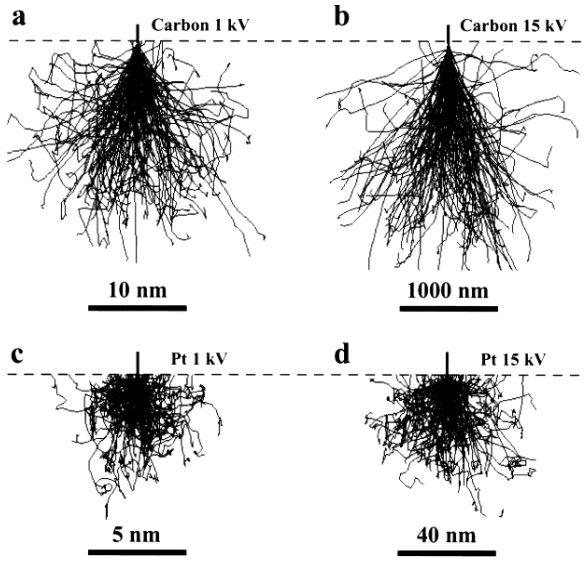

Figure 13. Monte Carlo simulation of electron scattering in carbon and platinum for incident beam energies of 1 and 15 keV respectively (Liu, 2000).

Elastic scattering occurs from electrostatic interactions with atomic nuclei and inelastic scattering results from interactions with the atomic electron cloud. Most of the accelerated electrons undergo forward scattering, which makes them difficult to detect, due to backscattering angles of < 90 °. However, a low number of primary electrons are elastically scattered at > 90 ° and may leave the sample into the vacuum, where they can be collected as backscattered electrons. The process of primary electrons leaving the sample as backscattered electrons occurs by the following processes: As primary electrons enter the sample and lose energy, this energy will be gained by surrounding atoms responsible for inelastic scattering (due to the law of conservation of energy). Energy gained by outer-shell electrons in these atoms may result in the release of weakly bound electrons being released with a loss of potential energy. Retained energy from the primary electrons will allow the escaping electrons to move through the sample as secondary electrons. Interactions between the secondary electrons and other atomic electrons will result in inelastic scattering,

resulting in further kinetic losses from the secondary electrons. The distance travelled by the secondary electrons within the material is averaged between 1 – 2 nm (Egerton, 2005), is a result of kinetic energy losses and can be represented by the probability that inelastic scattering depends inversely on kinetic energy, as shown in equation 17 (Egerton, 2005):

$$P_i(>\ \alpha) = \left(\frac{(\rho t)\left(\frac{Z}{A}\right) e^4}{\left(16\pi o^2 u E o^2 \alpha^2\right)} \right) \tag{17}$$

Where P_i probability of inelastic scattering, Z is the atomic number, E is the kinetic energy lost by the electron and gained by an atom, u is the atomic mass unit, A is the atomic mass number, ρt is the mass-thickness of the specimen, α is the scattering cross section of nucleus presented to each incident electron. This means that secondary electrons near to and traveling toward the surface may escape the surface and allow the production of a topographical image of the surface. By collection and detection of these secondary electrons at each SEM pixel, these electrons can be detected by their interaction with a scintillator/photomultiplier tube (PMT).

2.1.12. Inductively Coupled Plasma Mass Spectrometry

The loss of silver into solution by ionic leaching from silver-thin films must be quantified in order to understand the potentially competing factors affecting antimicrobial effects of the silver thin-films. Here, the concentration of silver in solution was investigated using the technique of inductively coupled plasma mass spectrometry (ICPMS).

ICPMS is one of the most versatile trace elemental analysis techniques available (Nelms, 2005) as it is capable of quantifying most elements in a range from pg/mL to μg/mL. This sensitivity is coupled with multi-element detection capabilities (Montaser and Golightly, 1992; Jarvis *et al*, 1992). ICPMS can also be used for aqueous samples with minimal operation (Ketterer and Szechneyl, 2008). This has led to ICPMS being used in a wide variety of industries, including the detection of arsenic in wine (Moreira *et al*, 2011), copper in ancient pottery (Aldrabee and Wriekat, 2011) and lead in environmental samples (Cocherie and Robert, 2007), to name a few examples. As the name ICPMS suggests, there is the combination of the inductively coupled plasma (ICP) and mass spectrometery (MS).

2.1.12.1. Inductively Coupled Plasma

The ICP (shown in figure 14) is used to ionise the sample, which can then be analysed using MS to separate and detect the ions based upon their mass. The plasma for the ICP is produced in the following way: argon gas is passed through a quartz torch (located in an induction coil) and to which a radio frequency (RF) field between 750

and 1700 W is applied. This creates an alternating current oscillation within this field. These oscillations produce electric and magnetic fields at the top of the torch (Nelms, 2005). The application of a spark to the argon gas via a Tesla coil strips off some of the electrons from the argon atoms leading to partial ionisation of the argon atoms ($Ar \rightarrow Ar^{+} + e^{-}$) These electrons become trapped in the magnetic field and are accelerated in closed circuit paths, a process known as inductive coupling. Electron collisions with argon atoms leads to further electrons stripped from the atoms, creating the high temperature of the plasma. Upon contact of the plasma with liquid samples, the liquid sample is ionised through the stages of desolvation, vaporisation, atomisation and finally ionisation. After passing through the plasma the sample is brought into the mass spectrometer for analysis.

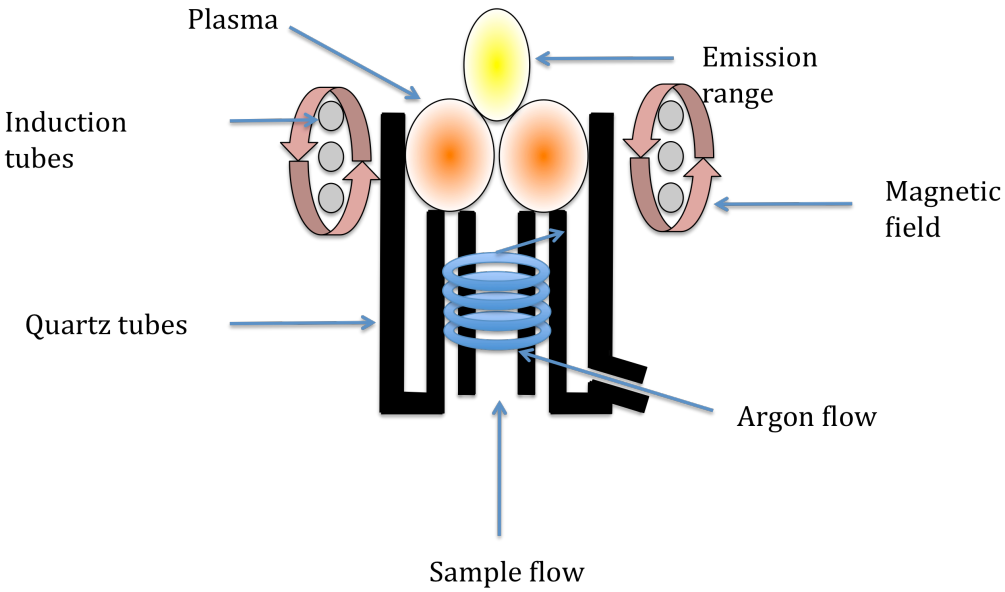

Figure 14. Schematic illustration of an Inductively Coupled Plasma. Argon gas passes through quartz tubes where a radio frequency radiation is applied, creating an alternating current oscillation. The application of a spark to the argon gas will strip off electrons, which undergo inductive coupling. Upon sample contact with the plasma, the sample is ionised and is passed into the mass spectrometer for analysis.

2.1.12.2. Mass Spectrometer

The principle for mass spectrometry has always been based upon the separation of an ionised sample by a magnetic field using the Lorentz force acting upon the moving charges. Figure 15 shows a schematic illustration of a MS. Where the sample ions are separated by a steady-state magnetic field, the method is known as 'static' MS. The alternative to this type of MS, is 'dynamic' MS, where electric fields are varied at a rate comparable with the transit time of the ions, such as the quadropole mass filter (QMF), ion trap and time-of-flight (TOF) mass spectrometer.

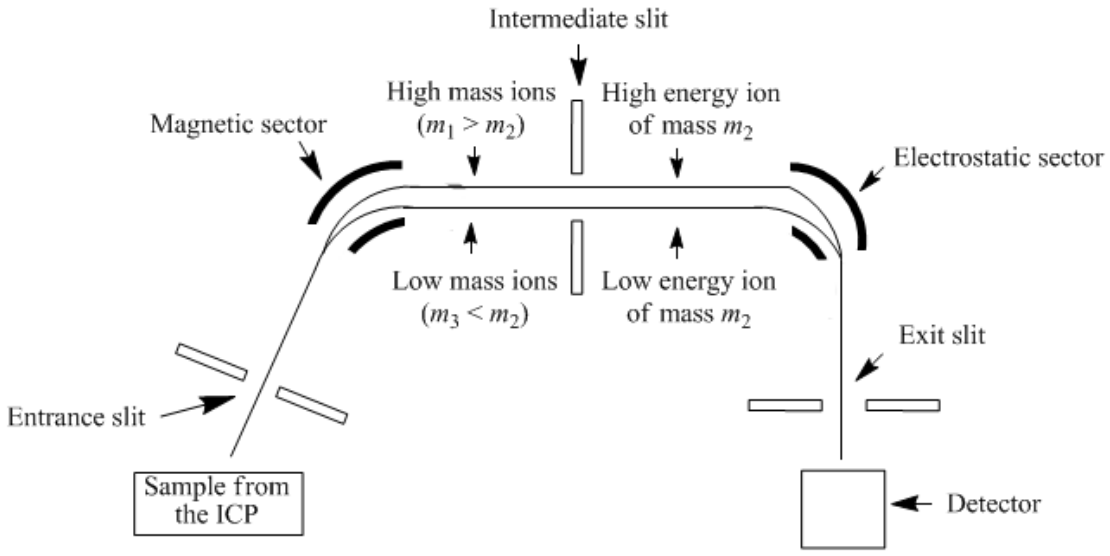

Figure 15. Schematic of a Mass Spectrometer, showing the sample coming from the inductively coupled plasma. The sample ions are accelerated, deflected depending on their mass and detected. Redrawn from Nelms, 2005.

As shown in figure 15, the main stages of MS are the ion source, mass separator or analyser and detector. Upon entrance of the ions into the MS stage of ICPMS, the ions are accelerated up to 10 ke V as it passes through the MS entrance slit. After acceleration, the positive ions (with uniform kinetic energy) are focused by a series of

ion lenses and traverse a curved flight path through the magnetic field according to their mass/charge ratio. The separation of charged particles in the magnetic field is shown in equations 18 to 22 (Nelms, 2005).

The kinetic energy *KE* of an ion of mass m and atomic number *z* is:

$$KE = zeV = \frac{1}{2} mv^2 \tag{18}$$

Where *e* is the electron charge, *V* is the acceleration voltage and *v* is the ion speed.

The path taken by ions of a given mass and charge is determined by the magnetic force F_m detailed in equation 19 and the centripetal force F_c shown in equation 20.

$$F_m = Bze \tag{19}$$

$$F_c = \frac{mv^2}{r} \tag{20}$$

Combining equations 19 and 20 gives the velocity of an ion in a magnetic field after acceleration (*v*), shown in equation 21:

$$v = \frac{Bzer}{m} \tag{21}$$

Substitution of equation 21 into equation 18 gives the mass/charge ratio with respect to field strength (equation 22) and assumes all ions passing through the magnet have uniform kinetic energy.

$$\frac{m}{z} = \frac{B^2 r^2 e}{2V} \tag{22}$$

Where z is the charge of the ion, e is the elementary charge, V is the acceleration voltage, m is the mass of the ion, B is the magnetic field strength and r is the radius of the magnetic field (Nelms, 2005).

Equation 22 shows that the path an ion takes through the magnet is dependent upon the acceleration voltage and the applied magnetic field strength. It is therefore possible to direct different ion masses on the detector by changing the field strength. The resolution of the MS is based upon the ability of the detector to differentiate different mass/charge ratios between ions. Equation 3.7 assumes that all identical ions have the same kinetic energy, which is only approximately correct, as the ions will have a statistical distribution of kinetic energies, due to electrostatic field fluctuations within the MS and increases the spread of the ions moving through the magnet to the detector, this limits the resolution of the system. The ability of MS to resolve different masses (R) is shown in equation 23:

$$R = \frac{m}{\Delta m} \tag{23}$$

Where Δm is the difference between two adjacent peaks and m is the nominal mass of the first peak.

2.2. Bacterial Interactions with Surfaces

Bacteria are ubiquitous throughout the biosphere and range in size, shape and biochemical activity. They are typically rod-like or spherically (cocci) shaped with dimensions no more than a few micrometres in length or diameter (Xu and Siedlecki 2012). Bacteria are commonly used in a wide variety of beneficial sectors, such as bioremediation and biotechnologies but are more commonly associated with pathogenicity – diseases affecting humans and animals (Watson and Brandly, 1949). Pathogenic bacteria are widely distributed in the environment and can be found in the soil, food, water and animals (Zoureb *et al*, 2008) and can be quickly and easily transferred between surfaces. One of the greatest current concerns with bacterial pathogenicity is that of hospital acquired infections, where a patient contracts a bacterial infection (either from a surface, liquid contact or inhalation). Once infected, the patient may act as a pathogenic vector and spread the disease to other patients, healthcare workers, or throughout the community. It has been stated that hospital acquired infections are one of the most common causes of morbidity in patients in the developed and developing world (Ponce de Leon, 1991; Richards and Russo, 2007). Beyond the loss of life, hospital acquired infections have been shown to have a significant economic impact (Ponce de Leon, 1991; Wakefield *et al*, 1988; Coella *et al*, 1993; Wenzel, 1995). They are also difficult to treat, with a wide variety of scientific and medical funding calls being released annually for novel treatments to reduce the spread of surface based infection. The interaction between the bacterial surface (known as a cell envelope) and a host organism is often of primary importance for a disease state.

2.2.1. Bacterial Cell Envelope

The bacterial cell envelope is the outermost region of the cell and provides stability to the cell, as well as protecting it from various external environments. Different cell envelope biochemistries allow different bacterial species to be identified by the cell envelope. A simple method often used is that of cell envelope staining, which exploits the binding of coloured reagents to cell envelopes depending on their biochemistries. The stained bacteria can be viewed with a light microscope and the bacterial species or certain biochemical properties can be identified. One of the most commonly used methods of envelope staining is the Gram stain (developed by Hans Christian Gram in 1884), which differentiates cell envelopes into two types. Bacteria that possess a bilayered outer membrane consisting of a thin peptidoglycan layer and a bilayered plasma membrane (Beveridge and Graham, 1991) are known as Gram-negative bacteria. Bacteria that possess a cytoplasmic membrane consisting of many polymer layers of peptidoglycan connected by amino acid bridges and a variable outer layer called the capsule (Jawets *et al*, 1987) are known as Gram-positive bacteria. The Gram's stain can also be indicative of different toxicological activities that result from different cell envelope chemistries and bacterial defence mechanisms to antimicrobial treatments. In this work, two model systems, one Gram-negative (*E. coli*) and one Gram-positive (*S. aureus*) bacteria were selected for study.

2.2.2. Gram-Negative Bacteria

The Gram-negative cell envelope is capable of withstanding extreme environmental factors. It has been recorded that it can withstand approximately 3 atmospheres of turgor pressure which is the internal pressure exerted from liquid inside a cell (Koch, 1998), variable temperatures and large pH shifts (with *Thiobacillus ferooxidans* being capable of growing at a pH of 1.5), and capable of expansion up to several times the normal surface area (Koch and Woeste, 1992). Although Gram-negative envelopes vary between bacteria, there is a high-level of structural and biochemical similarity between bacteria (Beveridge, 1999). The general structure is shown in figure 16.

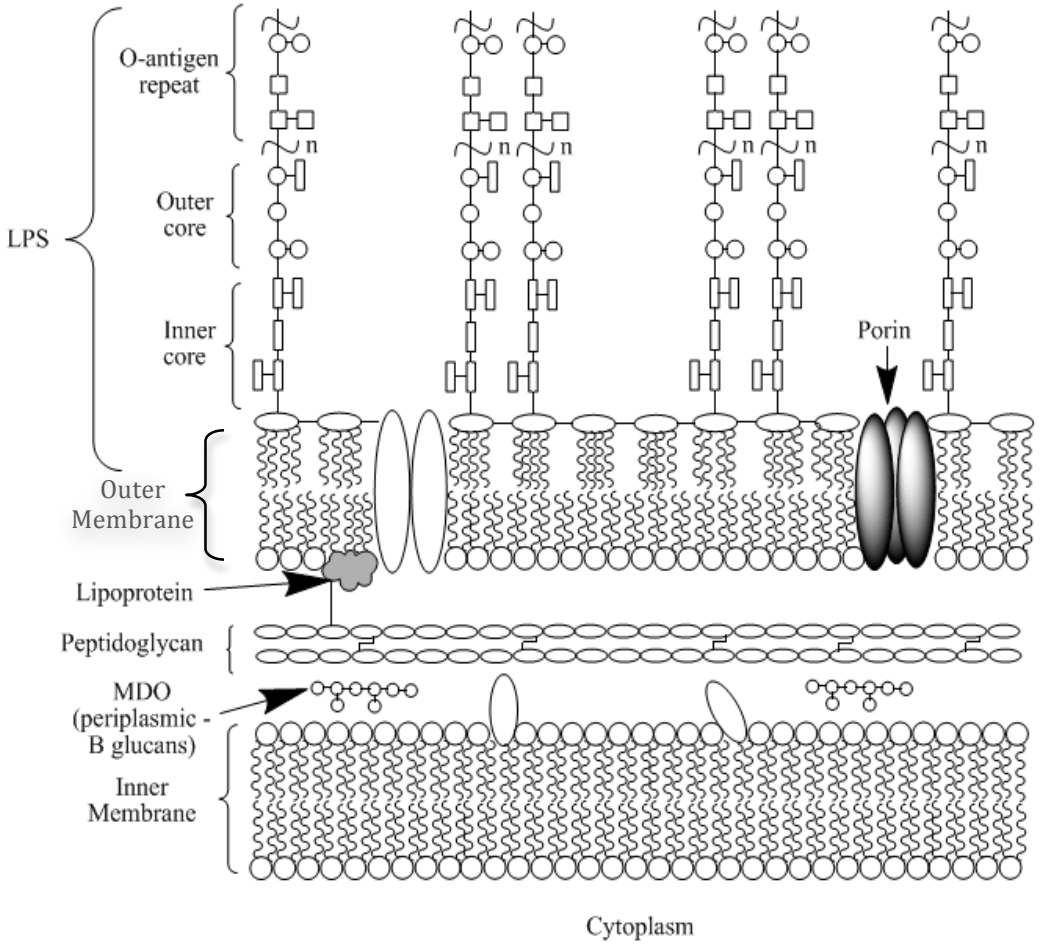

Figure 16. Schematic of a Gram-negative cell envelope. LPS = lipopolysaccharide. The thickness of the Gram-negative envelope is approximately 10 nm.

As shown in figure 16 the Gram-negative envelope is composed of the plasma membrane and the cell wall (outer membrane, peptidoglycan layer and periplasm) (Beveridge, 1981; Beveridge and Graham, 1991). The cell membrane is composed of an outer membrane, which is situated above a thin peptidoglycan layer. This lipid-protein bilayer contains phospholipids, proteins and lipopolysaccharides (LPSs). The requirement for bacterial nutrition through diffusion means that the outer membrane must be porous to certain substances and also capable of transporting others. Between the outer membrane and the plasma membrane is the periplasmic space, which contains the periplasm and peptidoglycan layer also known as the murein sacculus (Beveridge, 1995; Beveridge and Graham, 1991). In this study, *E. coli* was used as a model for Gram-negative bacteria. Examples of *E. coli* TEM images are shown in figure 17. This bacterium is rod shaped, and is approximately 2 μm in length with a diameter of 0.5 μm. This cell was chosen as it is has been well studied, with different strains such as 0157:H7 also being pathogenic and a source of global disease.

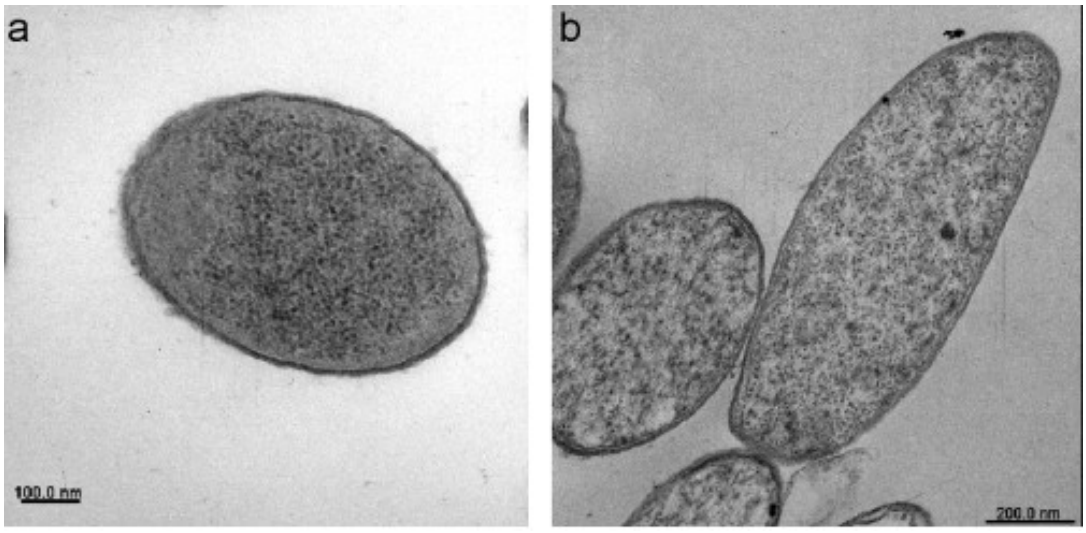

Figure 17. Transmisson electron micrograph of E. coli cells: (a) the cross section across the cell and (b) the cross section across and along the cell (Kim et al., 2007). The typical size of an E. coli cell is approximately 2 μm in length and 0.5 μm in diameter. The cells shown in this figure are of varying ages and thus different sizes.

2.2.3. Gram-Positive Bacteria

The Gram-positive cell envelope (figure 18) is substantially different to Gram-negative cell envelopes, as they do not contain an outer membrane but have a thicker and more cross-linked peptidoglycan layer. These differences result in the Gram-positive cell envelope being thicker (20 – 80 nm) than its Gram-negative counterpart (10 nm) and may be one factor for observed differences in antimicrobial activity between Gram positive and negative bacteria.

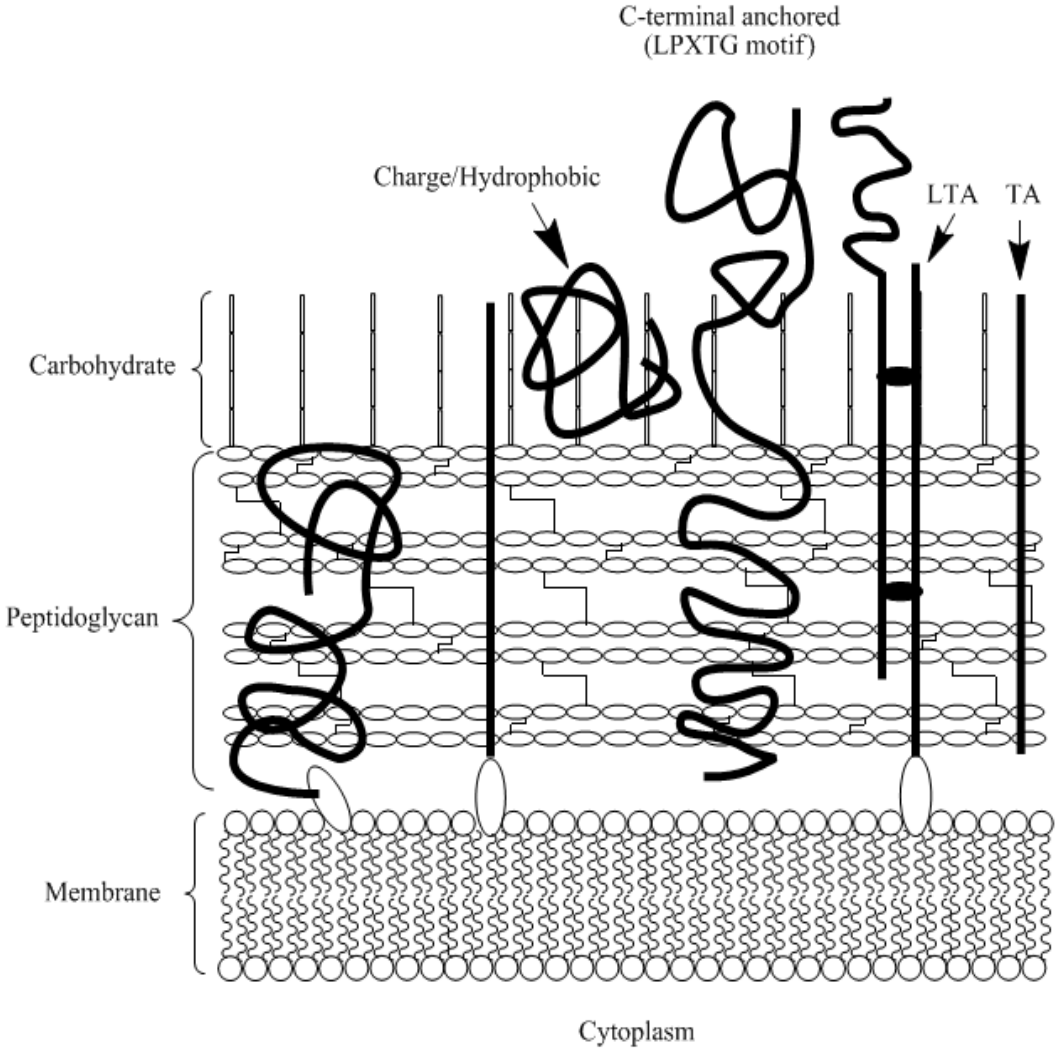

Figure 18. Schematic of a Gram-positive cell envelope. At the cell envelope surface are proteins, linked to the peptidoglycan layer. Techoic acid (TA) and lipotechoic acid (LTA) are commonly found at the surface along with proteins. Beneath the peptidoglycan layer is a lipid bilayer membrane.

At the cell envelope surface, Gram-positive bacteria have three classes of surface proteins, including: those that bind at their C-terminal ends via an LPXTG motif; those that bind via charge or hydrophobic interaction and those that bind through an N-terminal region such as lipoproteins. Fischetti *et al* (2000), have proposed that there are at least 25 different protein types on the cell envelope surface, enabling different activities and interactions for Gram-positive bacteria. Beneath the surface proteins is a relatively thick peptidoglycan layer, with a lipid bilayer membrane beneath it. Gram-positive cells can have a high-level of difference between membrane structures in comparison to Gram-negative bacteria (Beveridge, 1999; Beveridge *et al*, 1991; Giesbrecht *et al*, 1998; Higgins and Shockman, 1976). In this study, *S. aureus* was used as a model Gram-positive bacterium. TEM images of *S. aureus* from literature are shown in figure 19 *S. aureus* cells are cocci (spherical) and typically have diameters between 0.7 and 1.2 μm. This bacterium is regarded as amongst the hardiest of all non-spore forming bacteria (Sonenshein *et al*, 1993). Like *E. coli*, this bacterium is also of medical relevance as it also causes global pathogenicity through the strains called methicillin-resistant *staphylococcus aureus* (MRSA).

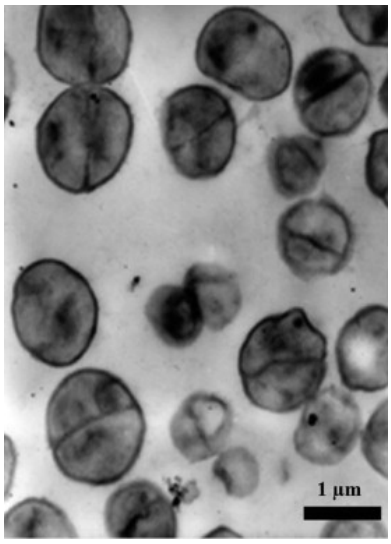

Figure 19. Transmission electron micrograph of S. aureus cells (Mirzanji et al, 2011). The diameter of the cells is approximately 0.7 to 1.2 μm.

2.2.4. Bacterial Growth

Bacterial growth is typically carried out in solution or on a surface such as agar. In this study, solution based bacterial growth was used. The solution used to support bacterial growth is referred to as a broth, which is composed of water, a carbon source such as glucose, salts and various additives specific to the bacteria being grown. Solution based growth is carried out by the insertion into (inoculation) a broth with a known number of the bacterial species under investigation (unless more complex experiments are desired and multiple microorganisms are inoculated). The bacterial population is monitored by real-time measurements or sampling and follows a common time profile that can be split into four different parts as shown in figure 20.

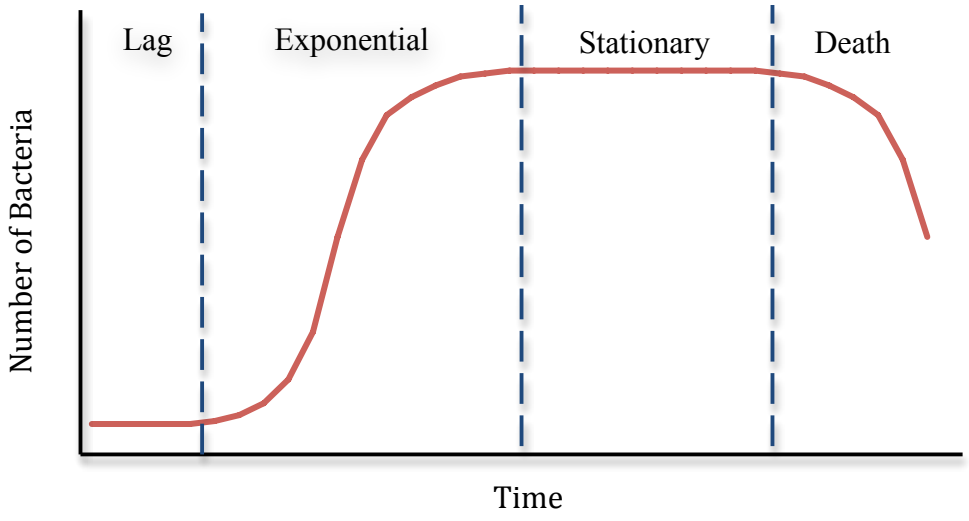

Figure 20. Theoretical bacterial growth curve; showing the four phases of bacterial growth, including a lag, exponential, stationary and death.

After bacterial inoculation, there is an initial lag phase as the bacteria are metabolically 'shocked' by the change of medium. This process often has the affect of temporarily stopping bacterial division for a few hours while the bacteria acclimatise leading to a period of static population size. After acclimatisation, the bacterial population move into a phase of exponential growth multiplying rapidly. This activity begins to both exhaust the nutrient supply and leads to a build up of toxic metabolic substances, resulting in the stationary phase – where the bacterial population growth slows rapidly and the population is large but static. Finally, as the remaining nutrients are consumed and the levels of toxic substances from metabolism build up, the bacterial population moves into a death phase, where large numbers of bacteria die and the population falls rapidly (Black, 2008).

The addition of a biostatic antimicrobial surface during the lag phase would be expected to increase the lag phase by inhibiting bacterial growth. Alternatively, if the antimicrobial were biocidal, the height of the growth curve would be expected to be lower due to bacterial death from the antimicrobial.

Population growth curves are a simplistic, yet highly effective and informative methodology for the determination of antimicrobial activity of surfaces. Measurement of growth curves can also be carried out in real-time.

2.2.5. Quantification of Bacterial Population Growth

There are numerous methods for the quantification of bacterial population growth. These methods can be split into the classical approach of light microscopy with cellular staining and the more modern methods based on electrochemistry and dynamic light scattering (DLS). Although the more modern methods allow a greater variety of bacterial growth parameters to be determined, such as real-time measurements, live and dead cell counts, and flocculation, they can be difficult to use with antimicrobial measurements on surfaces. In the case of electrochemical methods, the use of metallic surfaces can interfere with the solution-based conductivity. DLS systems can also be unsuitable for the measurement of antimicrobial activity on bacterial growth, as many systems are not suited to the introduction of an absorbing or reflective surface as it can interfere with light scattering and detection.

On this basis the classical method of light microscopy, bacterial staining and optical density were selected for this study. These methods and their use in bacterial population growth and antimicrobial detection are described in the following sections.

2.2.6. Absorbance Spectrophotometry

Absorbance spectrophotometry for bacterial quantification requires the use of the Beer-Lambert law (Wayne and Wayne, 1995), which allows absorption to be treated quantitatively and characterises the fraction of monochromatic light transmitted through an absorbing medium. It can be expressed by the following equation:

$$\frac{I_t}{I_o} = 10^{\varepsilon Cd} = e^{-\alpha Cd} \tag{24}$$

Where I_o is the incident light intensity, I_t is the transmitted light intensity, C is the concentration of absorber, d is the depth of absorber through which the light beam has passed, ε is the decadic absorption coefficient and α is the natural absorption coefficient (Wayne and Wayne, 1995).

For liquid measurements, and in particular bacterial detection in solution, the law is usually expressed as shown in equation 25 (Wayne and Wayne, 1995):

$$A = -\log_{10}\left(\frac{I_t}{I_o}\right) \tag{25}$$

Where A is the absorbance. While for simple biochemical detection, the term absorbance is generally acceptable; solutions containing bacteria may undergo greater amounts of light scattering, where the term optical density (OD) is preferred. As a method of bacterial and biomass quantification, OD measurements have often been

used (Bauchop and Elsden, 1960; Rosenberger and Elsden, 1960 and Coultate and Sundaram, 1975), as within certain limits OD is proportional to both bacterial quantity and biomass (Koch, 1981). Difficulties and limitations of OD measurements can arise, with low and high numbers of bacteria that are below the limit-of-detection or block light transmission from the monochromator to the detector, respectively.

For this study, a microplate absorbance spectrophotometer was used for OD measurements of the bacterial solutions. A simplified schematic of the system is shown in figure 21. In this technique, monochromatic light is passed through a quartz well containing the bacterial sample, where the intensity of the transmitted light is detected. Calibration of the absorbance spectrophotometer was achieved by using solutions containing known concentrations of bacteria.

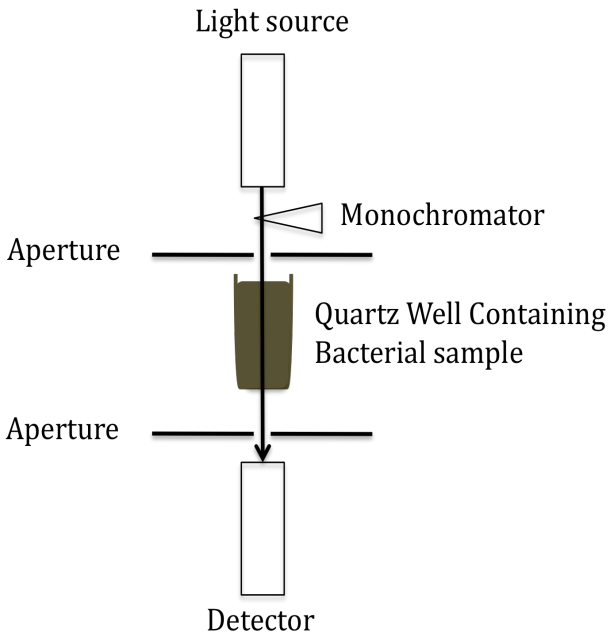

Figure 21. Absorbance microplate spectrophotometer setup, showing, the generation of a beam of light, the direction of the selected wavelength through an aperture, through the bacterial sample held in a quartz microplate well and then through a second aperture to a photodetector.

2.2.7. Light microscopy

Bright field light microscopy is a relatively simple, fast and inexpensive method for the examination of bacterial cells. A schematic of a bright field light microscope is shown in figure 22. In this system, light is transmitted through the sample and via a series of lenses to the eye, with bright areas indicating more transparent regions.

The light microscope allows ambient cellular examination and is more accessible than electron microscopy but suffers from more limited spatial resolution. Simplistically, if a feature is too small, it cannot be resolved. Resolution is limited in optical microscopy by instrument imperfections and vibration, but fundamentally by the ability to focus light through an aperture onto a sample (Dedecker, Hofkens and Hotta, 2008). In this study, an examination of bacterial cells was carried out using an optical microscope with cellular staining methodologies to characterise various aspects of cellular morphologies and biochemistries.

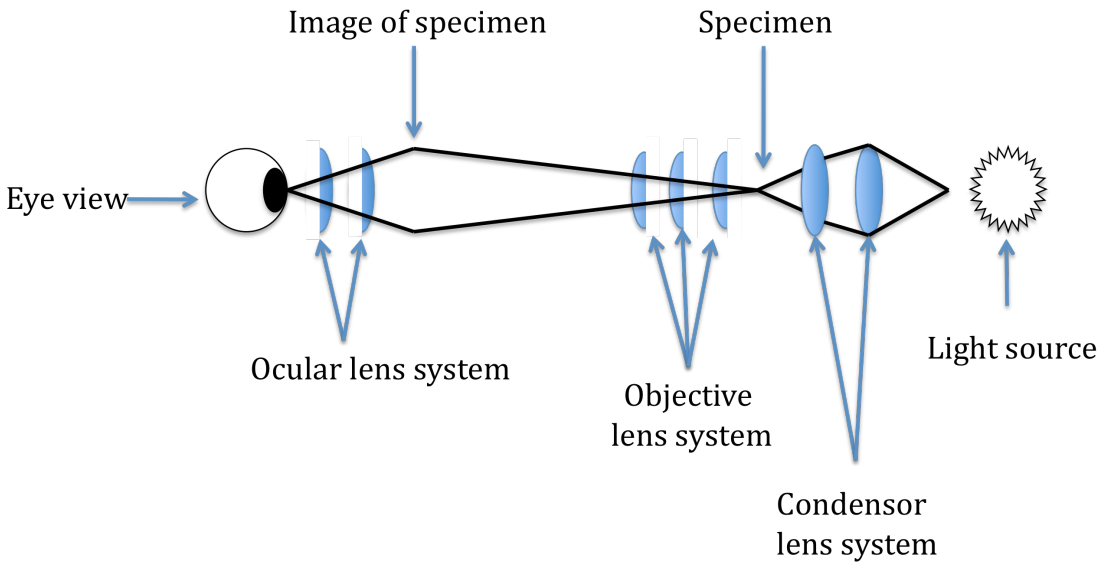

Figure 22. Schematic of a bright field light microscope, showing) the passage of light from the source, through a condenser system, specimen, objective lens system to the viewer's eye.

2.2.8. Bacterial Staining – Gram and Trypan Blue

In conjunction with optical microscopy, bacterial staining can be a rapid, low-cost and informative method for bacterial identification (Black, 2008). Principally, staining works to identify or characterise bacterial cells based upon their cellular envelope biochemistry.

Gram-staining:

The Grams stain is routinely used to differentiate bacterial cells into two categories based on cell envelope biochemistries (as detailed in section 2.2.2 and 2.2.3). The general method for staining bacterial cells by this method is as follows (Davies *et al*, 1983): The bacteria are placed on top of a microscope slide and are heat fixed using a Bunsen burner to the slide. Crystal violet (shown in figure 23) is then poured over the slide, whilst the slide is agitated by hand for 5 minutes.

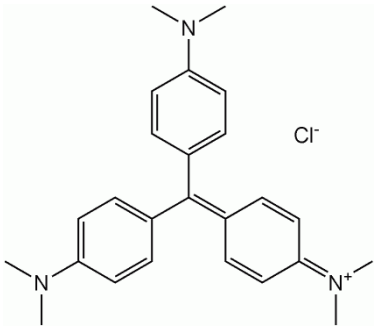

Figure 23. Molecular structure of Crystal violet (Tris(4-(dimethylamino)phenyl)methylium chloride), molecular formula: $C_{25}N_3H_{30}Cl$.

Iodine is subsequently added to the slide and the slide is agitated by hand for a further 5 minutes, before the bacteria are decolourised by the addition of 95 % alcohol. Finally, Safranin (figure 24) is then added to stain the cells, so that they can be visualised under a light microscope.

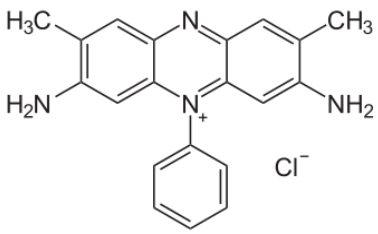

Figure 24. Molecular structure of Safranin, molecular formula: $C_{20}H_{19}N_4^+$, Cl^-.

As introduced earlier, the cellular envelope response falls into two types, which aid bacterial identification. Gram-negative bacteria have a lipid outer membrane and a peptidoglycan layer, the alcohol step of the Grams stain washes away the crystal violet and results in the safranin staining the bacteria red (Salton, 1963). The thicker Gram-positive cell membranes are able to hold the crystal violet stain, which colours the bacteria purple (Salton, 1963). Beyond the scope of this study, are members of the *Archaea* (regarded as ancient and more complex bacteria), which cannot be easily differentiated by Gram staining, as a result of their cell wall composition and structure (Beveridge, 1990; Beveridge and Schultze-Lam, 1997).

Trypan Blue Staining

Trypan Blue ($C_{34}H_{28}N_6O_{14}S_4$) (shown in figure 25) is a stain process that allows the differentiation of live and denatured cells in a liquid or surface sample.

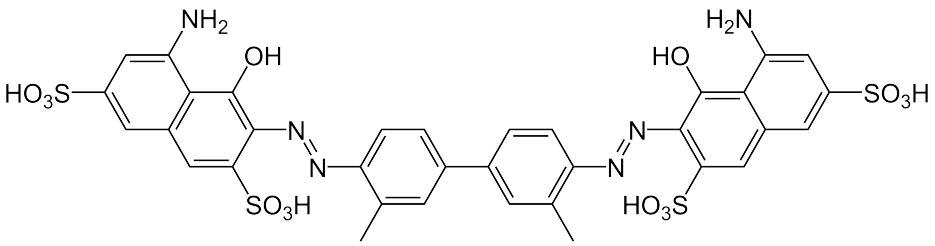

Figure 25. Molecular structure of Trypan Blue.

The ability to differentiate live and dead bacterial cells with Trypan Blue is based upon the ability of bacterial cells to uptake the stain into the cell. Under standard growth conditions, Trypan Blue is not up taken by living bacterial cells, as it is negatively charged and cannot penetrate the cell envelope or pass through ion channels within the cell envelope. Therefore, these cells do not take the stain and appear lightly stained under a light microscope. However, if the cell is denatured and lysis occurs, through the cell envelope not being able to selectively maintain equilibrium, Trypan Blue can enter and stain the cell. This is most likely to occur through cell death (Freshney, 1987). Examples of stained cells are shown in figure 26 where live cells appear lightly stained and denatured cells appear dark blue.

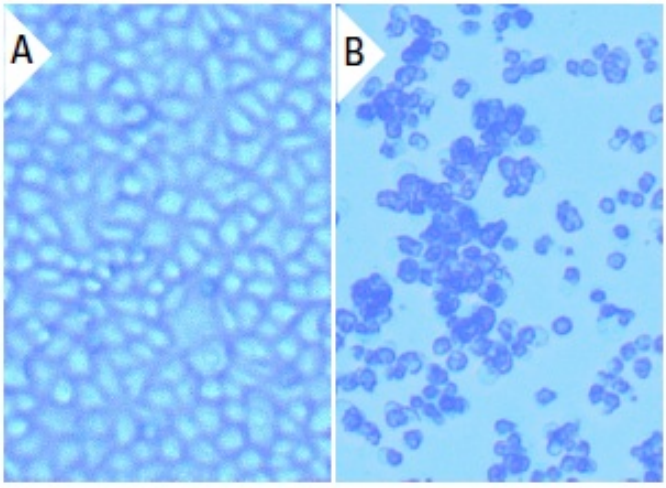

(a) (b)

Figure 26. Trypan Blue staining. Buffalo preantral cells (mammalian) cells are shown stained with Trypan Blue (http://www.scbt.com/pt/datasheet-216028-trypan-blue.html). Lightly stained cells (a) were alive and darkly stained cells (b) were denatured.

2.2.9. Silver as an Antimicrobial

Bulk scale silver has been used as a medical treatment for over 2,000 thousand years (Hippocrates, 400 B. C.). It has found wide usage against microorganisms, including Gram-positive and Gram-negative bacteria, fungi, protozoa and viruses (Balazs *et al*, 2004). Silver has also been found to display antimicrobial activity against antibiotic-resistant microorganisms (Stobie *et al*., 2008; Melayie and Youngs, 2005), to reduce infections in burned areas (Parikh *et al*, 2005; Ukur *et al*, 2005; Panacek *et al*, 2006), colonisation in textiles (Panácek *et al*, 2006; Imazato *et al*, 1998), in water (Chou *et al*, 2005) and on medical devices (Panácek *et al*, 2006; Rupp *et al*, 2004; Samuel and Guggenbichler, 2004; Strathman and Wingender, 2004; Ohashi *et al*, 2004; Bosetti *et al*, 2002). A driving factor for the use of silver is the variety of forms that silver can be used in, including: bulk, thin-film, ionic (Ag^{+}) and nanoparticles. Although there are many forms and antimicrobial uses of silver, there are however barriers to the use of this metal, including cost of the metal, potential toxicity in the environment and higher organisms and interferes with biochemical regulatory control (with the last factor being beyond the scope of this study).

2.2.10. Ionic silver Antimicrobial Activity

Ionic silver can be released from bulk, thin-films, nanoparticles, and composites or ionic silver can be obtained directly as a solution. Ionic silver prepared in solution form has been most widely examined, in part due to the complexity of measuring ionic silver release from surfaces.

Time-release systems typically include silver salt impregnated porous films that, upon contact with a solution, allow the diffusion of silver salts into the solution (Williams *et al*, 1989). Systems based on timed ionic release have been shown to be highly antimicrobial (Slawson *et al*, 1992; Russel and Chopra, 1996) and are usually non-toxic to mammalian cells (Williams *et al*, 1989; Berger *et al*, 1976), but the release of the ions is finite and the control of ionic concentrations over time is difficult (Sant *et al*, 1999). The situation is complicated by the fact that silver ions can potentially forming complexes with biological fluids. These factors have made the long-term use of impregnated films with silver salts an unattractive option for antimicrobial usage.

The mode of action of silver ion antimicrobial activity remains to be clarified. It is known that silver ions (Ag^{+}) interact strongly with electron donors (Brook *et al*, 2006) and that the ions can readily undergo metal-ligand reactions with protein groups containing thiols and sulfides (Clement *et al*, 1994; Fernández *et al*, 1996; Liau *et al*, 1997). These metal-ligand reactions can act to destabilise three-dimensional folding between amino acid residues. Silver is also known to interact with other cellular components such as nucleic acids (Jensen *et al*, 1996), which can interfere with DNA replication. Silver ions have been shown to inhibit phosphate uptake and exchange in *E. coli*, which causes an outward movement of accumulated phosphate from the cell,

potentially leading to cell death (Schreurs and Rosenberg, 1982). They have also been shown to cause a leakage of protons through membranes of *V. chloerae*, which led to the collapse of the proton motive force, through the binding to membrane proteins (Dibrov, 2002). Silver also has a high affinity to cysteine residues, which are located in NADH reductases, in bacteria such as *E. coli*, which can reduce the production of energy within cells (Bragg *et al, 1974*; Friedrich, 1998). The binding of silver ions to these bacterial respiratory chain enzymes can result in inefficient transportation of electrons to oxygen at the terminal oxidase. In turn, this will result in large quantities of reactive oxygen species and accounts for the low levels of silver ions required for antimicrobial activity in bacteria such as *E. coli* (Holt and Bard, 2005). Interestingly, these reactions are predominantly located inside the bacterial cell envelope, resulting in the need for silver ions to penetrate the cellular envelope to produce the antimicrobial response.

2.2.11. Silver Nanoparticle Antimicrobial Activity

Silver nanoparticles have found wide use as antimicrobials. Not only have silver nanoparticles been used directly in solution as antimicrobials but have also been immobilised onto surfaces including, catheters (Stevens *et al*, 2009), wound dressings (Maneerung *et al*, 2008), surgical masks (Li *et al*, 2006) and food packaging (Fernández *et al*, 2010). They have also been incorporated into three-dimensional platforms such as; cellulose membranes (Yang *et al*, 2011), chitosan/starch films (Yoksan and Chirachanchai, 2010), graphene oxide (Das *et al*, 2011), cotton (Kim *et al*, 2010) and ceramics (Lv *et al*, 2009) to name but a few materials currently being

used. The bacterial 'workhorse' of *E. coli* has been well studied to try to elucidate the mechanisms of silver nanoparticle based antimicrobial activity (Yang and Pon, 2003). Various methods have been suggested, including, the release of silver ions, penetration of nanoparticles within the bacterial cell envelope and structural damage to the envelope through puncturing.

Silver ions can be released from the large surface area of nanoparticles and therefore all ionic mechanisms can result. In addition the penetration of silver nanoparticles within the cell envelope can potentially result in any of the disruptive effects described in the previous section, if silver ions are released within the cell. It can also lead to metal-ligand reactions between nanoparticles and the internal organelles. Other effects however may be important. The shape of nanoparticles can play an important role in the biological response (Albanese *et al*, 2010; Liu *et al*, 2009; Hutter *et al*, 2010). Of particular interest is the geometry of the nanoparticle, with needle-shapes having been shown capable of impaling entire cells (Donaldson *et al*, 2006; Poland *et al*, 2008; Warheit *et al*, 2004; Miyawaki *et al*, 2008). Studies carried out on carbon nanotubes also show that cylindrical nanoscale materials are capable of physically puncturing cell membranes (Kang *et al*, 2007; Kang *et al*, 2008; Liu *et al*, 2009). In a study by Martinez-Gutierrez *et al* (2009), the antimicrobial concentrations of silver nanoparticles for a range of microorganisms were investigated (shown in table 1).

Microorganism	Description	Antimicrobial Concentration (μg/L)
Bacillus subtilis	Gram Positive Bacteria	1.7 ± 0.2
Mycobacterium bovis	Gram Positive Bacteria	1.1 ± 0.1
Mycobacterium smegmatis	Gram Positive Bacteria	0.5 ± 0.3
MRSA (methicillin-resistant staphylococcus aureus)	Gram Positive Bacteria	0.5 ± 0.2
Staphylococcus aureus	Gram Positive Bacteria	0.4 ± 0.1
Actinobacter baumani	Gram Negative Bacteria	0.5 ± 0.2
Escherichia coli	Gram Negative Bacteria	0.5 ± 0.2
Pseudomonas aeruginosa	Gram Negative Bacteria	0.4 ± 0.1
Aspergillus niger	Fungi	25 ± 0.0
Candida albicans	Fungi	6 ± 0.4
Cryptococcus neoformans	Fungi	3 ± 0.0

Table 1. Antimicrobial activity of silver nanoparticles, measured against different microorganisms (Martinez-Gutierrez et al, 2009).

The concentration of silver nanoparticles required to cause an antimicrobial effect in bacteria has however been found to be much lower than the concentration causing mammalian cellular toxicity. Silver nanoparticle toxicity has been linked to cell death through the production of reactive oxygen species that have the capability to alter protein function or DNA structure, which in turn can alter the state of the cell leading to death (Nel *et al*, 2006). Reactive oxygen species are known to be highly reactive and it has been suggested by AshaRani *et al* (2009) that the oxidation of silver nanoparticles from contact with cell culture media or proteins in the cytoplasm may liberate Ag^+ ions, which could increase the toxicity.

Examining the potential toxicity of silver nanoparticles to higher organisms, the study by Braydich-Stolle *et al* (2005) is worth considering. This study exposed a mouse spermatological stem cell line to silver nanoparticles, to determine the toxicity. It was found that concentrations of silver nanoparticles between 5 μg/L and 10 μg/L were capable of inducing cell death. Not surprisingly, this study left many questions unanswered, such as the mechanism of cell toxicity, whether ionic silver was present and the toxicity of different nanoparticle sizes, crystal structures and reaction conditions.

A challenge for determining the antimicrobial activity and toxicity of nanoparticles is the variation between nanoparticles based on sizes, shapes and surface chemistries. As Albanese *et al* (2010) stated: "*while there have been significant research activities on this topic, it has been somewhat frustrating for researchers not to be able to say conclusively, nanoparticle parameter(s) x causes effect y*".

2.2.12. Nanoscale Structures and Surfaces Antimicrobial Activity

As the availability, understanding and demand for the production of structured thin-films has increased, so has the exploration of different surface structures. Often in the production of thin-film patterning for antimicrobial applications, the rationale has been towards increasing the surface area of the material in potential contact with microorganisms (Sabbani *et al*, 2010). This is however somewhat of an incomplete view, as the architecture of the structures and chemical composition must also be considered, alongside whether ionic or molecular release from the thin-film takes place.

In contrast to nanoparticles, only a limited amount of work on nanostructures and surfaces have been examined for activity as antimicrobials. Silver nanoclusters (averaging 50 nm in diameter) patterned onto micrometre-sized zeolite squares (Sabbani *et al*, 2010), showed a high-level of antimicrobial activity at a kill rate of over 90 %, within three hours against *E. coli*. The high-level of activity is not surprising due to the micron sized zeolite structures containing silver ions as well as being coated with silver clusters. The authors of this study attributed the mode of antimicrobial action as being predominantly through the release of silver ions from the zeolite. The release of zeolite would be finite and does not take into account surface architecture of the silver structures. Nanocrystalline silver has also been shown to partially dissolve through release of atomic (Ag^0) and ionic (Ag^{+1}) at concentrations of up to 70 ppm (Ricketts *et al*, 1970; Spacciapoli *et al*, 2001; Hall *et al*, 1987; Maple *et al*, 1982). Depletion of silver ion concentrations from solution, potentially through the uptake into cells, has been shown to further increase ionic release from the surface (Dowling *et al*, 2003).

The formation of roughnened silver surfaces has received little attention for antimicrobial applications. Known studies have included ion implantation of Ag^+ (Pham *et al*, 1998), sputtering (Rönnow *et al*, 1999; Eisenhammer and Muggenthaler, 1994), and thermal evaporation, which was used in this study.

The potential mechanisms of antimicrobial activity of silver surfaces with nanoscale roughness and features surface can be likened to the antimicrobial activity of nanoparticles and ionic silver but provides a more controlled system, which integrates ionic and structured effects. Unless atomically smooth and flat, fabricated surfaces have potential structures that would puncture bacterial cell envelopes. There is however the potential for bacteria to bind to surfaces through bio-fouling, which is the process of 'sludge' like layers forming on the surface.

2.2.13. Chromium Adhesion Layer Toxicity

An area that is often not explored with the formation of thin-films and antimicrobial activity is the effect of the adhesion layer on antimicrobial activity. In this study, a 3 nm chromium layer was deposited onto silicon dioxide, with subsequent silver deposition on the silver. Chromium is a transition metal capable of existing in several oxidation states, with each oxidation state having a different level of toxicity associated with it. Cr (VI) is considered the most toxic form (Cervantes *et al*, 2001). The study by Dreyfuss (1964) showed that chromate could be transported across bacterial cell envelopes and once inside cells, is reduced to Cr (III). The transport of chromate, with resulting bacterial toxicity has so far been demonstrated with

Escherichia coli (Karbonowska, Wiater and Hulanicka, 1977; Sirko *et al*, 1990), *Pseudomonas fluorescens* (Ohtake, Cervantes and Silver, 1987) and *Alcaligenes eutrophus* (Nies, Nies and Silver, 1989).

The mechanism of chromium toxicity has been related to the process of Cr (VI) reduction to lower oxidation states (Kawanishi, Inoue and Sano, 1986), where free radicals are generated (Kadiiska, Xiang and Mason, 1994). Free radicals have been associated with triggering DNA alterations as well as other toxic effects (Shi and Dalal, 1990). Oxidative damage to DNA is considered the basis of genotoxic effects produced by chromium (Aiyar *et al*, 1991; Itoh *et al*, 1995; Luo *et al*, 1996).

Although a silver layer was fabricated on top of a chromium adhesion layer in this study, with the films being very thin, and with cleaning there was a potential for bacterial cells to be exposed to the chromium.

2.3. Surface Fouling and Cleaning

Surface fouling from contacting materials can result in undesired adsorbed layers, particularly from complex biological solutions. It is most likely to occur when the surface is chemically reactive to the species present in solution. Fouling is problematic for antimicrobial surfaces as it has the potential to cover parts of the surface and reduce its antimicrobial activity. Surface roughness and imperfections have been shown to increase fouling, due to the increased surface area for attachment and nucleation of reactive species on the surface (Yoon and Lund, 1994). For surfaces with complex features and architectures, cleaning can be problematic as it may change

the structures present on the surface. For commercial applications, there are often large drivers to develop simple and cost effective methodologies to clean and regenerate fouled surfaces. There is also the possibility of developing antimicrobial surfaces that can be disposed or reapplied once fouled, but this is often not possible for numerous applications such as medical coatings. These issues also relate to nanoscale materials surfaces where functionality is based upon the structuring of the surface.

As the silver thin-film surfaces had shown antimicrobial activity against *E. coli* and *S. aureus*, but had been fouled, the potential for simply cleaning a fouled surface was of interest, both commercially and scientifically. The challenge for a cleaning methodology with a nanostructured surface would be to remove the adsorbed fouling species, with limited damage to the surface. Although many cleaning reagents methods are commonly used for removing fouling, there is little literature on removing fouling from nanostructures. Indeed, many methods, focussing on heavy acids, alkalis and ablation are not only entirely unsuitable for many commercial uses but would potentially remove the thin-film from the substrate. A simple, low-cost and regularly used cleaning agent in the semi-conductor industry is isopropyl alcohol (IPA), which was examined in this study as a method of removing fouling from nanostructured surfaces. The use of IPA is lower in cost than alternative methods such as plasma cleaning and autoclaving, and also does not require specialist operator skills.

Chapter 3. Materials and Methods

In this chapter, the materials and methods used to fabricate silver-thin films and their interactions with the bacteria E. coli and S. aureus are examined.

The set-up and use of oblique angle thermal evaporation is described for producing nanostructured thin-films, alongside AFM, RBS, ellipsometry and ICPMS to characterise surface roughness, material thickness and material desorption.

Methodologies for bacterial growth and determining antimicrobial activity by bacterial staining with light microscopy and absorbance spectrophotometry are described. Methods for both surface and solution based antimicrobial activity are presented, in conjunction with appropriate controls, to indicate the effect of the nanostructuring.

Finally, IPA cleaning methods to remove biological fouling from surfaces is presented, along with the examination of the thin-films after cleaning, by ellipsometry and AFM.

3.1. Thin-Film Sample Preparation

Thin-films of silver with nanoscale surface features were prepared by thermal evaporation onto angled silicon dioxide substrates. The substrates were prepared from a wafer of thermally oxidised silicon. Each sample substrate was cut into a 5 mm × 5 mm chip before being cleaned prior to deposition. The first stage of cleaning was carried out by chip immersion in 99 % acetone, with sonication for 30 seconds. The chips were subsequently nitrogen dried before being immersed in 99 % isopropylalcohol (IPA) for 30 seconds with sonication. After nitrogen drying, the chips were considered clean and were immediately attached to the sample holder (figure 27) to the holding angles of 0 °, 18 °, 40 ° and 70 ° to the horizontal by poly-methyl methacrylate (PMMA). The sample holder was then attached to the thermal evaporator ready for evaporation. The angled substrate holder was made in house, with a goniometer being used to measure the fabricated angles.

Figure 27. Thermal evaporator sample holder - that can hold samples between the angles of 0 ° and 70 °. The four angles used throughout this study are highlighted on the sample holder. The sample holder is held at the top of the thermal evaporator chamber.

Once the samples were attached to the thermal evaporator, the crucibles at the bottom of the evaporator were filled individually with 99.99 % pure silver and 99.99 % pure chromium. A rotary pump and turbo pump were then used to create a high vacuum inside the evaporator chamber (between 10^{-6} – 10^{-8} Torr). Passing a high current through the conducting crucibles resulted in the metals evaporating onto the substrates. A piezoelectric quartz rate monitor measured the rate and mass of metal during deposition. The first layer deposited was 3 nm of chromium. This was followed by a 20 nm deposition of silver, without breaking vacuum. The chromium layer was used to form an adhesive layer between the silver and silicon dioxide.

Immediately after thin-film deposition on the silicon dioxide substrates and thermal evaporator cooling, the substrates were removed from the thermal evaporator by tweezers and were stored in sealed plastic boxes. The boxes were not purged and were not altered from ambient conditions.

3.1.1. Scanning Electron Microscopy

To more clearly understand the thin-film surfaces, a Hitachi SU-70 FEG scanning electron microscope, was used to image the surfaces at a magnification of × 100,000 within one hour of thin-film deposition, at an accelerating voltage of 1.5 - 3.00 kV.

3.1.2. Material Thickness

Film thickness measurements were carried out using an Ellipsometer (single-beam Sentech SE500 operated in a class 100 fume hood) and an RBS (5SDH Pelletron Ion Beam Accelerator made by National Electrostatics Corporation). Before thin-film measurement, a silicon dioxide chip was used to calibrate the ellipsometer and RBS for a chip without metal deposition. Prior to the chip measurement, the chip was cleaned by immersion in 99 % acetone with sonication for 30 seconds. The chip was subsequently nitrogen dried before being immersed in 99 % IPA for 30 seconds with sonication. After nitrogen drying, the chips were considered clean and were measured by ellipsometer and RBS.

Initial thin-film measurements were taken within 30 minutes of removal from the thermal evaporator. These measurements were compared to the values taken from the Quartz Rate Monitor in the thermal evaporator, which had measured metal deposition at a quartz substrate at 0 °. Due to the design of the thermal evaporator, all measurements of metal deposition are taken with the quartz rate monitor being at an angle of 0 °. It was unknown whether an increasing angle of substrate would alter the deposition thickness of the film as only substrates at an angle of 0 ° could be measured.

3.1.3. Post Deposition Changes

To examine post deposition changes through oxidation and ambient contamination, the thin-films were moved into a Class 100 Clean Room environment within 30 minutes of deposition. Ellipsometry measurements were repeated over a 16-week period to measure any changes in the film thickness.

3.1.4. Metal Desorption

The loss of silver and chromium from the thin-films was measured using a NexION 300S ICP-MS. The nanostructured thin-films were incubated in deionised water at 37 °C (± 1 °C) for 48 hours with measurements being taken at 0, 0.5, 1, 2, 4, 8, 16, 24 and 48 hours. All measurements were taken in triplicate.

3.2. Biological Experimental Methods

In this section, the details of biological stocks, their preparation and experimental details of bacterial growth and antimicrobial testing will be detailed

3.2.1. Biological and Biochemical Stocks

The bacteria *Escherichia coli* ATCC 10536 and *Staphylococcus aureus* ATCC 6538 were purchased from ATCC Laboratories (USA) and were individually stored on refrigerated nutrient agar slopes at 4 ºC.

Sterile nutrient agar and nutrient broth were purchased from Fisher Scientific (UK) in agar plates and 250 ml shake flasks respectively and were refrigerated at 4 °C.

Phosphate buffered saline (PBS) was used to prepare bacteria for antimicrobial testing and to wash bacterial samples after centrifugation. PBS (137 mM NaCl; 2.7 mM KCl; 10 mM Na_2HPO_4; 2 mM KH_2PO_4) was made up from the following (Sambrook and Russell, 2001):

NaCl	8.0 g
KCl	0.2 g
Na_2HPO_4	11.5 g
KH_2PO_4	0.2 g

The buffer was made up using 1 litre of distilled water. The pH was adjusted to 7.0 using 1 M NaOH (prepared from 99.998 % NaOH pellets).

3.2.2. Bacterial growth Methodology

All bright field microscopy measurements were taken with a Fisher Brand FB7048 microscope at × 100 magnification.

All absorbance measurements were carried out using a PowerWave HT Microplate Spectrophotometer. The Microplate Spectrophotometer was attached to a 2 GHz processor powered PC and used BioTek's Gen 5 software. An 8-well quartz plate (2 cm diameter well) was used for all bacterial measurements, with a single beam of monochromatic light at 600 nm.

All autoclaving was carried out using an Astell Scientific ASB260BT+AVC001 autoclave. Glassware was sterilised by heating the autoclave to 100 °C at 1 atmosphere pressure for 15 minutes. Biological samples were sterilised by heating the autoclave to 121 °C at 1 atmosphere pressure for 30 minutes.

E. coli and S. aureus were both grown separately by the following method. Separate bacterial colonies were removed from refrigerated slopes and were streaked out over nutrient agar plates. The plates were subsequently incubated at 37 °C for 24 hours. Separate bacterial colonies were taken from the nutrient agar plates and were placed into two separate nutrient agar shake flasks, containing 100 ml of nutrient broth. The shake flasks were incubated in an orbital incubator at 37 °C under agitation at 50 rpm for 24 hours. Two separate sub-cultures (2 ml each) were taken at the end of the 24-hour period and were inoculated into two new nutrient broth shake flasks (containing 100 ml of fresh nutrient broth) and were incubated overnight at 37 °C under agitation

at 50 rpm. All bacterial work was undertaken using aseptic techniques in a Category 2 laboratory.

3.2.3. Solution Based Antimicrobial Activity

All of the antimicrobial testing was carried out in conjunction with the Molecular Workstation Ltd in Newcastle (UK).

E. coli and *S. aureus* were grown as detailed in section 3.2.2 with separate bacterial solutions concentrations of 1.0×10^8 bacteria being inoculated into 10 ml tubes containing 2 ml of nutrient broth. The tubes were prepared with negative and positive controls and with the addition of 5 mm x 5 mm coated silicon dioxide chips, as detailed in table 2. Negative controls included the measurement of nutrient broth without bacteria, and positive controls included the use of silicon dioxide chips not coated with silver.

Test Name	Bacteria	
	E. coli	*S. aureus*
Control 1	2 ml nutrient broth	2 ml nutrient broth
Control 2	2 ml nutrient broth, 1.0×10^8 bacteria, uncoated 5 mm × 5 mm chip	2 ml nutrient broth, 1.0×10^8 bacteria, uncoated 5 mm × 5 mm chip
Control 3	2 ml nutrient broth, 1.0×10^8 bacteria	2 ml nutrient broth, 1.0×10^8 bacteria
Evaporated sample 0 °	2 ml nutrient broth, 1.0×10^8 bacteria, coated 5 mm × 5 mm chip	2 ml nutrient broth, 1.0×10^8 bacteria, coated 5 mm × 5 mm chip
Evaporated sample 18 °	2 ml nutrient broth, 1.0×10^8 bacteria, coated 5 mm × 5 mm chip	2 ml nutrient broth, 1.0×10^8 bacteria, coated 5 mm × 5 mm chip
Evaporated sample 40 °	2 ml nutrient broth, 1.0×10^8 bacteria, coated 5 mm × 5 mm chip	2 ml nutrient broth, 1.0×10^8 bacteria, coated 5 mm × 5 mm chip
Evaporated sample 70 °	2 ml nutrient broth, 1.0×10^8 bacteria, coated 5 mm × 5 mm chip	2 ml nutrient broth, 1.0×10^8 bacteria, coated 5 mm × 5 mm chip

Table 2. Table of controls and experimental procedures for determining antimicrobial activity.

The growth tubes were subsequently incubated at 37 °C in an orbital incubator at 50 rpm for 48 hours. At the time points of 0, 0.5, 1, 2, 4, 8, 12, 16, 24 and 48 hours, 50 μl samples of nutrient broth containing bacteria were removed from the tubes and analysed for absorbance, at 600 nm. All measurements were taken in triplicate. Antimicrobial activity was calculated according to:

$$\text{Antimicrobial Activity} = \left(\frac{\text{Bacterial Growth with Cr Coated } SiO_2 \text{ - Control 1}}{\left(\frac{\text{Control 2 + Control 3}}{2} \right)} \right) \times 100 \quad (26)$$

3.2.4. Surface Bound Antimicrobial Activity

All of the antimicrobial testing was carried out in conjunction with the Molecular Workstation Ltd in Newcastle (UK).

E. coli and *S. aureus* were grown as detailed in section 3.2.1. with separate bacterial solutions concentrations of 1.0×10^8 bacteria being pipetted into 10 ml growth tubes containing 2 ml of nutrient broth. Each growth tube also contained chromium and silver deposited films for the four different surface structures. The growth tubes were subsequently incubated at 37 °C in an orbital incubator at 50 rpm for 48 hours. At the time points of 0, 0.5, 1, 2, 4, 8, 12, 16, 24 and 48 hours, 50 μl samples of broth containing bacteria were removed from the tubes, and rinsed in 0.1 M PBS for 30 seconds to remove unbound cells from the surfaces. The surfaces were then covered with a 0.1 ml solution of 0.4 % Trypan Blue Stain. The slides were allowed to stand for 3 minutes before being examined with optical microscopy under 100 × magnification. Three areas of 100 μm^2 were examined using a graticule for live and dead cells. The determination of live and dead cells was carried out is in accordance with Freshney (1987).

3.2.5. Bacterial Adsorption on Surfaces

To allow real-time measurement of potential bacterial adsorption and build up on the thin-films, quartz crystals were coated with 3nm chromium and 20 nm silver in the thermal evaporator at the angles of the four different surface structures. Each silver coated quartz crystal mounted into the rate monitor assembly was subsequently immersed in a bacterial broth of *E. coli* or *S. aureus*, under agitation at 37 ° C for 48 hours. The quartz rate monitor was used to continuously record the mass loading over a 48-hour period, thus allowing measurement of the rate of deposition and the total mass of bacterial binding to the surfaces. The quartz crystals were mounted vertically to avoid producing a false-positive effect from gravitational accumulation.

3.3. Thin-Film Cleaning

To determine the effect of surface cleaning on non-fouled silver thin-film surfaces 100 % isopropyl alcohol (IPA) was poured over each surface for 30 seconds before being wiped with a 6200 polyester wipe, followed by drying for 30 seconds with dry nitrogen gas. The cleaning procedure was repeated up to a maximum of three times for each surface. After cleaning the surfaces, physical examination was carried out by RBS to determine material thickness and by AFM to determine surface roughness after each cleaning procedure.

Chapter 4. Results and Discussion:

Nanostructured Thin-Films

In this chapter, silver nanostructured thin-films formed by thermal evaporation were physically examined by AFM, RBS, ellipsometry and ICPMS. AFM data showed that as the angle of thin-film deposition increased, the RMS surface roughness increased, along with an increase in x, y and z-nanostructure sizes. This trend was coupled with a decrease in thin-film thickness, when examined by RBS and ellipsometry. Island formation, measured by SEM also indicated an increase in nanostructure size, with increasing angle of deposition. Storage of the thin-films in class 100 clean room conditions showed post-deposition increases in thin-film thickness, over a 16-week period of approximately 10 %. Stability of the thin-films in aqueous conditions was tested by ICPMS and showed negligible desorption of silver and chromium over a 48-hour period.

4.1. Surface Structuring Thin-Film Island Formation

SEM images of the thin-films were taken to examine visual differences between the surfaces, based on the deposition angle during thermal evaporation (as shown in figure 28). The lower angles of deposition show smaller island sizes and nanostructuring, which increases with deposition angle. This is in agreement with AFM data discussed later (shown in figures 29 and 30). Interestingly, all thin-film surfaces appear to show a lack of continuity (with voids and defects between crystallites) within the film and are potentially showing the chromium adhesion layer and silicon dioxide substrate. The largest defects within the films are shown at the highest angle of deposition. It is speculated that these observations are not only a consequence of oblique angle deposition but also of the maximum deposition of a film being 23 nm.

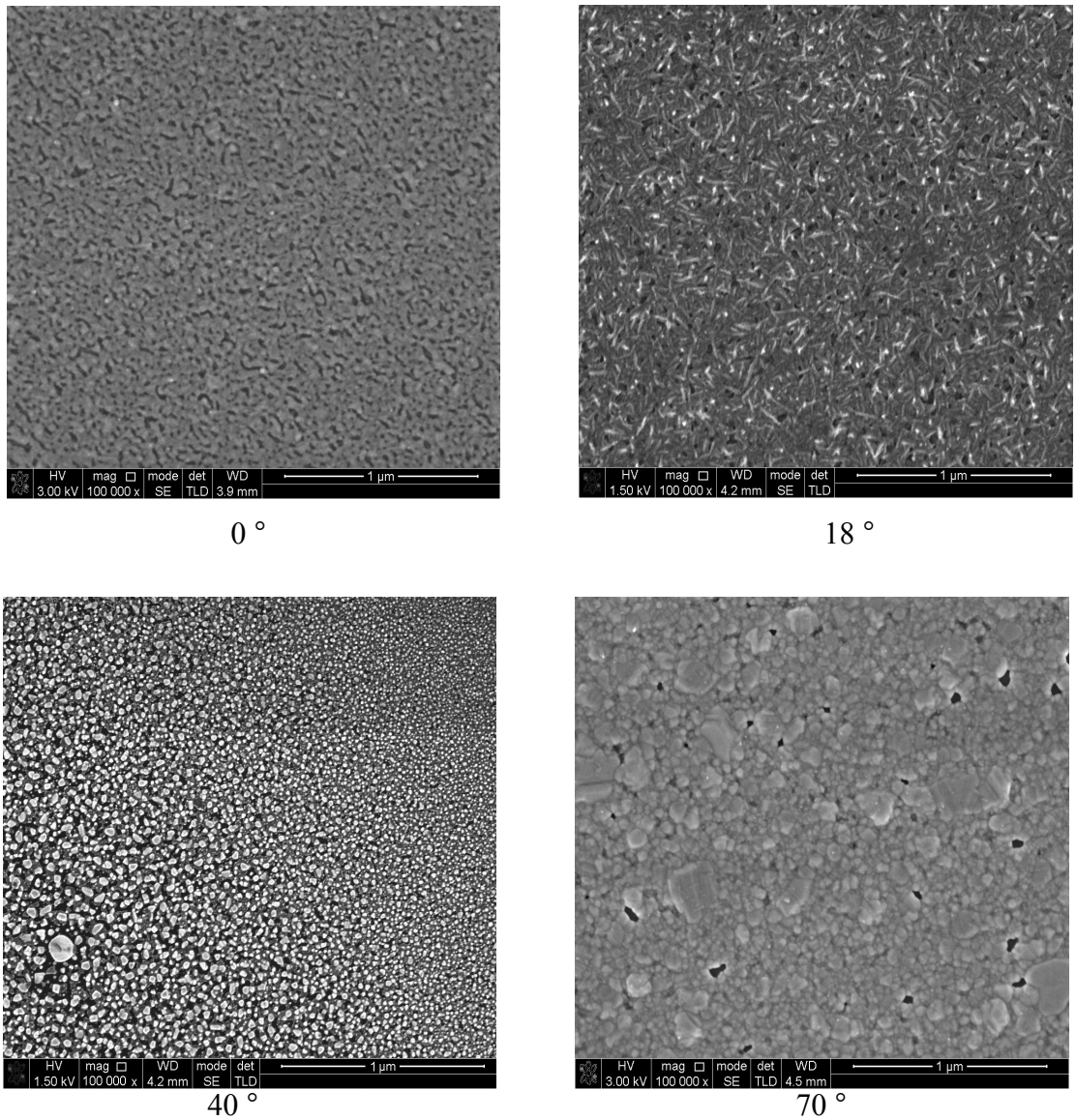

Figure 28. Scanning electron microscopy images of the thin-film silver-chromium surfaces. The four thin-films deposited at angles of 0 °, 18 °, 40 ° and 70 ° were imaged within 1 hour of being deposited.

Tapping mode AFM measurements of 5 µm × 5 µm sections of the fabricated thin-films showed that the surface topography has increased roughness for films deposited at higher angles. Three-dimensional surface plots and two-dimensional line scans are shown in figure 29 and figure 30 respectively. No measurement was taken to assess the effect of deposition angle on exposed chromium.

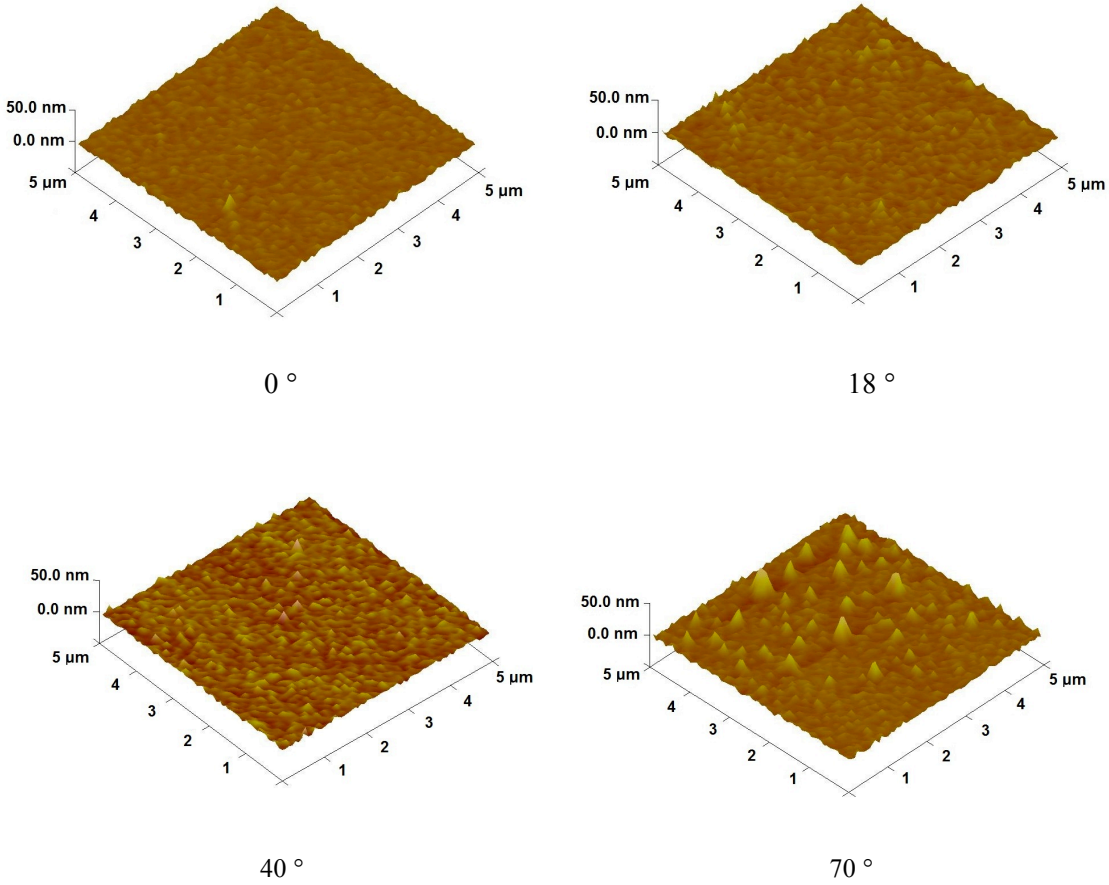

Figure 29. Examples of tapping AFM images of 5 µm × 5 µm silicon dioxide chips coated with 3 nm chromium and 20 nm silver deposited at 0 °, 18 °, 40 ° and 70 °. The images were taken randomly from the AFM scans.

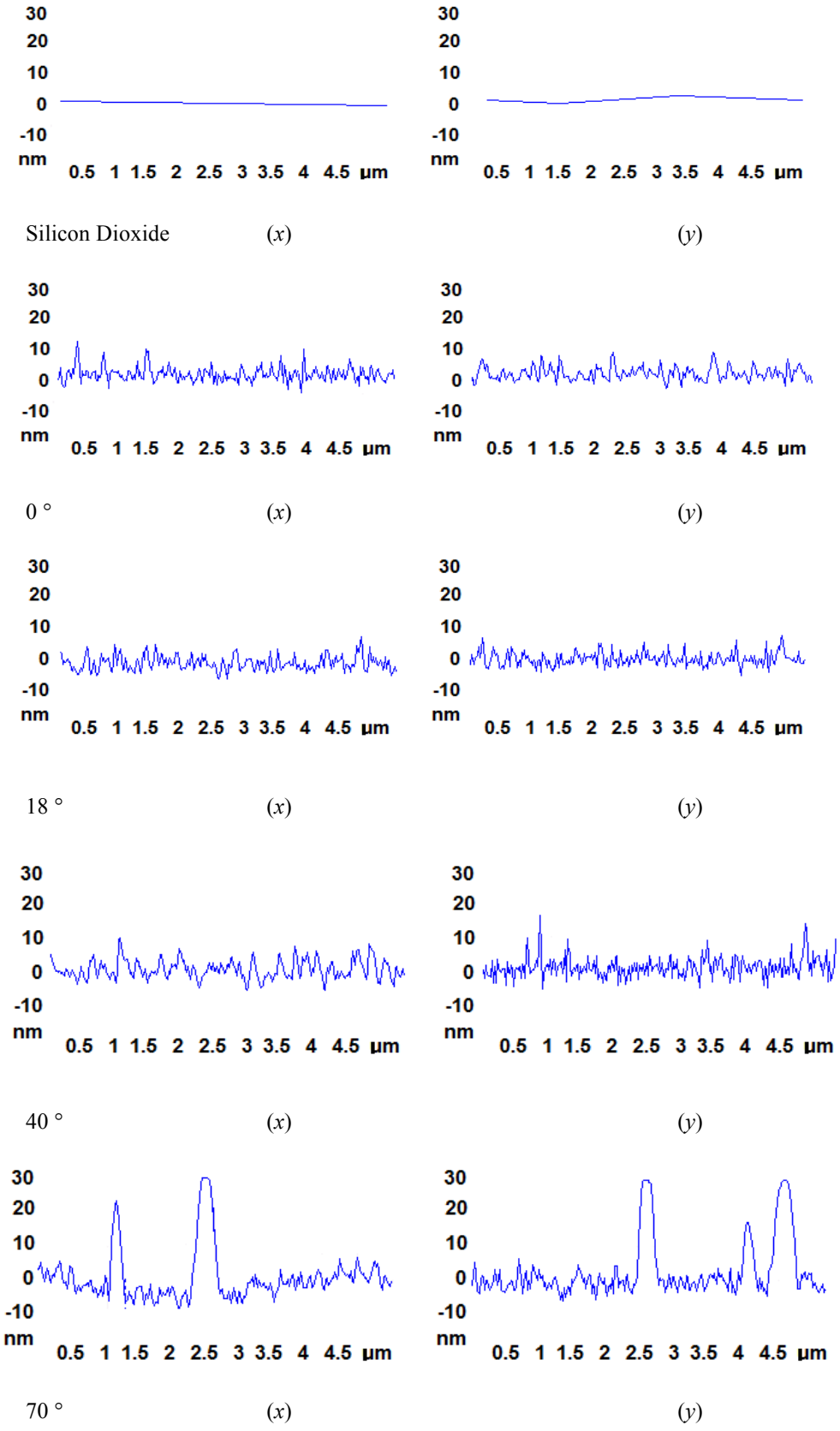

Figure 30. AFM line profiles, along the x and y-axes of silicon dioxide, 0 °, 18 °, 40 ° and 70 ° silver deposition (20 nm) on top of chromium (3nm). The images were taken randomly from AFM scans.

Both figures 29 and 30 show an increase in surface structures with an increase in deposition angle. At the lower angles few features are shown, but as the angle of deposition increases, relatively large lateral structures occur. Some of these features are more than 10 nm high for the 40 ° sample and exceed the nominal film thickness for the samples deposited at 70 °. There is no obvious structural anisotropy apparent throughout any of the samples. Using the VEECO V613r1 software, the RMS surface roughness was calculated and is shown in figure 31.

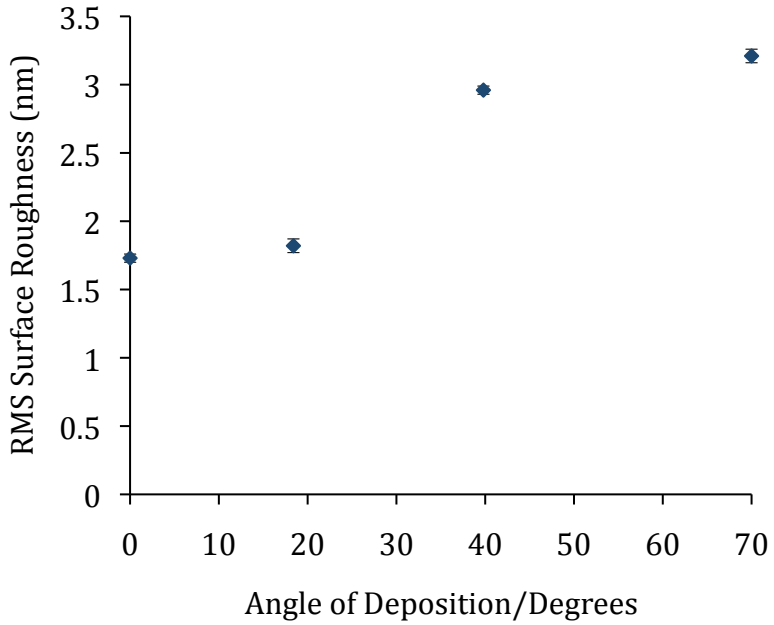

Figure 31. RMS silver surface roughness (nm) by angle of deposition. 3 nm chromium and 20 nm silver were deposited onto silicon dioxide (5 mm x 5 mm) chips, at angles of 0 °, 18 °, 40 ° and 70 °.

Observation of the line profiles indicates that formation of a small number of sharp high amplitude peaks, particularly at the highest deposition angle. Furthermore, as mentioned previously there is no apparent structural anisotropy in the appearance of the peaks, in contrast to expectation from other work on angle dependent deposition, which shows anisotropic structuring. In light of this the use of RMS roughness could

be limiting, so analysis of the peak structuring was also undertaken. The average peak widths were calculated for both *x* and *y*-axes and are shown in figure 32. Examining nanostructure peak widths along both *x* and *y*-axes showed an increase in peak widths with angle of deposition. The peak widths along *x* and *y*-directions are very similar for films deposited at angles up to 40 ° and diverge somewhat for films deposited at 70 ° supporting the earlier observation of little or no structural anisotropy being induced in thin-films of the order of 20 nm by oblique incidence deposition. The effect of deposition angle on silver coverage of the chromium adhesion layer is unknown, as is the potential chromium component of surface roughness and nanostructures.

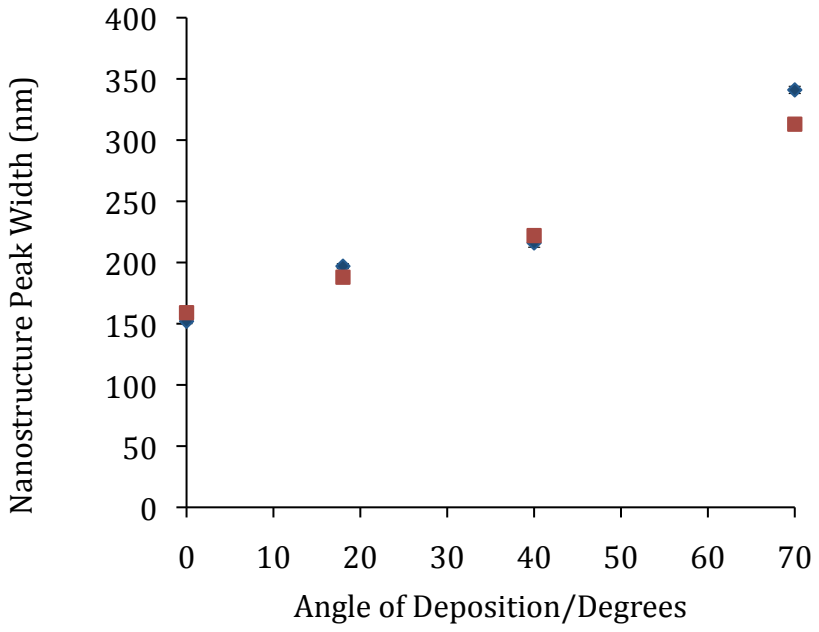

Figure 32. The average width of the large intermittent peaks measured at the half maximum (FWHM). Measurements were taken along the slope of deposition for x and y-axes for 20 nm silver deposited on 3 nm chromium at the angles of 0 °, 18 °, 40 ° and 70 °.

4.2. As-Deposited Film Thickness

The theoretical total nominal thickness of all films was 23 nm. This was subsequently measured by RBS and ellipsometry, with results shown in figure 33. Measurements by RBS and ellipsometry are in reasonable agreement for all films measured. Both showed a near linear decrease in film thickness with increasing angle of deposition. It is clear from SEM and AFM analysis that the surface topography is strongly dependent upon the angle of deposition and this may lead to the effective change in film thickness that is obtained by RBS and ellipsometry at this scale of deposition.

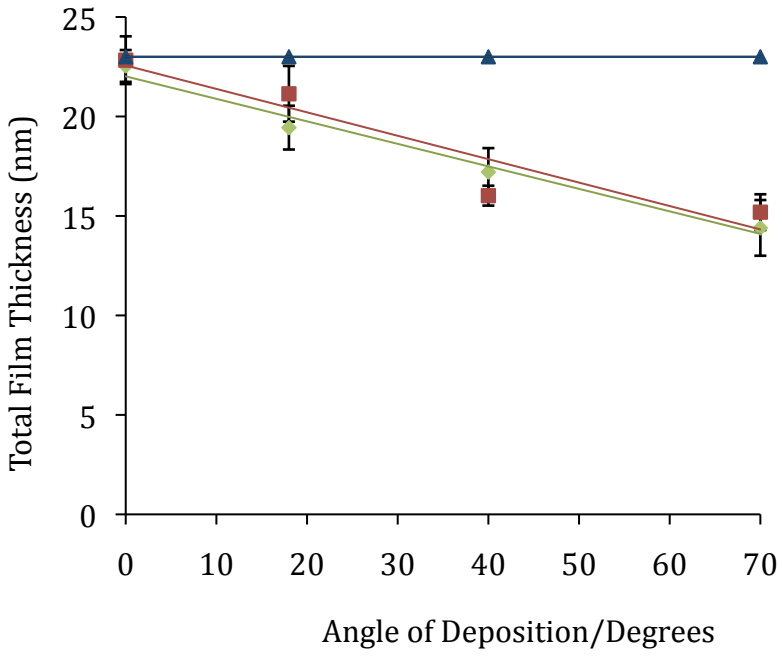

Figure 33. Total film thickness (nm) of chromium and silver deposited onto silicon dioxide measured by RBS ■ and ellipsometry ◆ , with a theoretical total thickness of 23 nm (3 nm chromium and 20 nm silver) determined by a quartz crystal rate monitor ▲

4.3. Post Deposition Surface Changes

Silver and chromium may undergo various chemical reactions in non-vacuum and ambient conditions. These reactions range from the oxidation of the surfaces, through to the fouling of the surface by commonly occurring biochemical molecules via metal-ligand reactions such as thiols (R-SH) and amines ($R\text{-}NH_2$). Beyond such reactions, the surface may foul from bulk-scale contamination such as grease from human contact – which can often be a great problem for commercialisation of thin-film technology for antimicrobial usage. To examine oxidation and other surface changes due to ambient environmental exposure of the thin-films, the thin-films were removed directly to a Class 100 Clean Room environment within 30 minutes of deposition. Ellipsometry measurements were repeated over a 16-week period to measure the film thickness (as shown in figure 34).

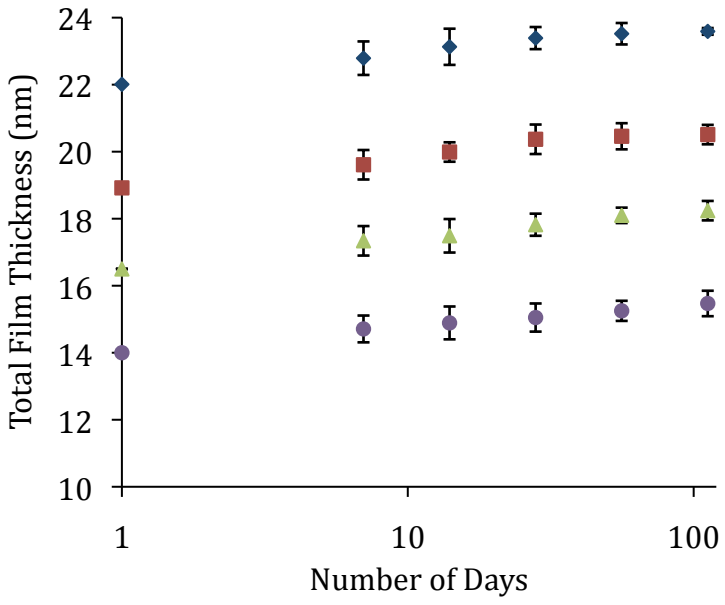

Figure 34. Total film thickness (nm) over a 16-week period. The four substrates (evaporated 3 nm chromium and 20 nm silver on silicon dioxide at the angles of 0 °, 18 °, 40 ° and 70 °) were stored in a class 100 environment immediately after evaporation and had the total film thickness measured over the 16-week period.

Changes to all thin-film thicknesses were plotted in figure 35 and in all cases, the thickness increased over a 16-week period. The increase of film-thicknesses was not uniform, although similar trends were observed for all films. The increase was attributed to oxidation of the silver, exposed chromium and ambient contamination from the class 100 environment. The growth mechanism and topography of these thin-film growth mechanisms is at this time unknown. Interestingly, a difference in film thickness was measured between all films, most pronounced between the highest and lowest deposition angles. This may be attributable to less material being present at higher deposition angles, or changing ratios of surface silver and chromium, which undergo different post-deposition growth.

In the antimicrobial testing, the time from deposition of a thin-film to immersion in an active broth was typically 1 day, suggesting an oxidation coating of less than 1 nm.

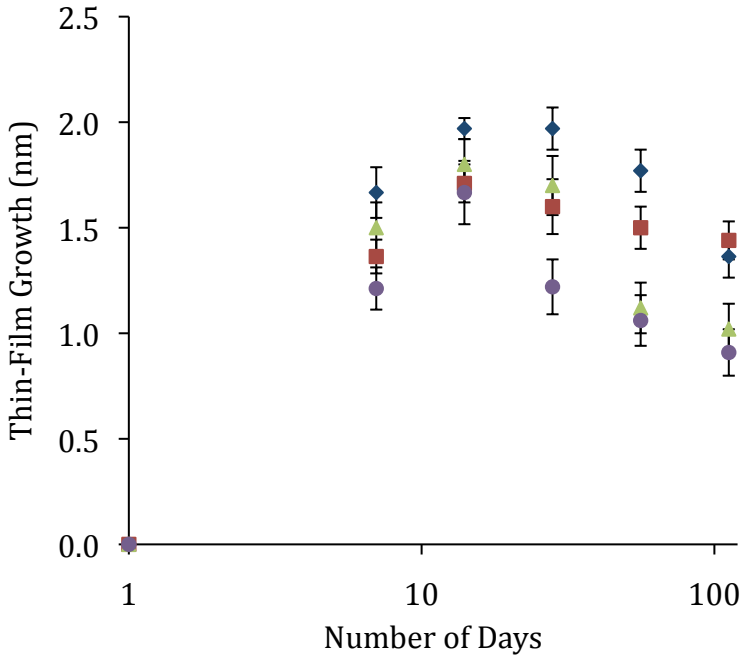

Figure 35. Rate of film growth (nm) on top of the silver surfaces over a 16-week period. The four surfaces deposited at angles of 0 °, 18 °, 40 ° and 70 ° were stored in a class 100 environment immediately after thermal evaporation.

4.4. Desorbed Silver and Chromium from Nanostructured Surfaces

In order to understand the potential role of ionic/atomic loss from the films in antimicrobial activity, ICPMS was used to quantify the desorption of chromium (figure 36) and silver (figure 37) in deionised water over a 48-hour period.

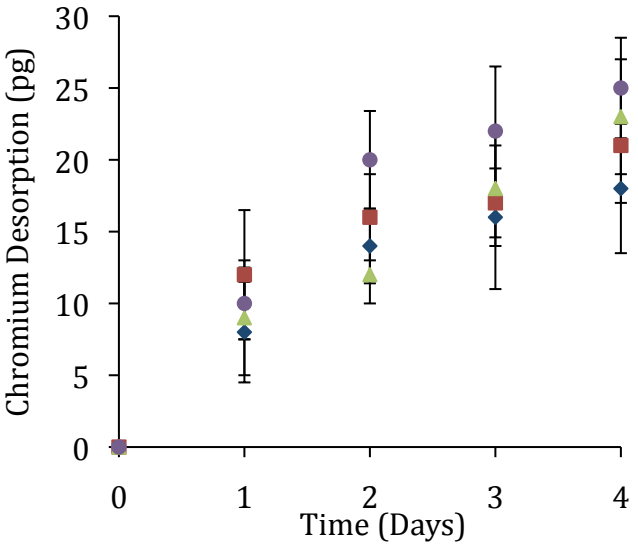

Figure 36. Loss of chromium from thin-films. ICPMS, was used to measure chromium from 0 ° ◆ , 18 ° ■ , 40 ° ▲ and 70 ° ● angled films. Measurements were taken from 5 mm × 5 mm chips stored at 37 ℃ over a 48-hour period.

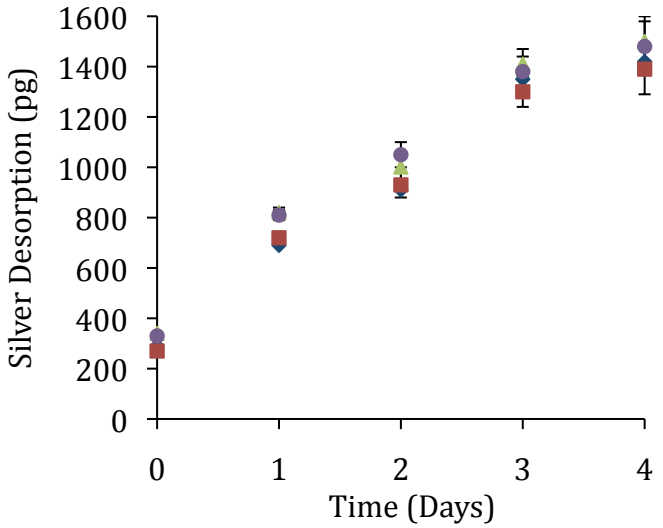

Figure 37. Loss of silver from thin-films. ICPMS, was used to measure silver from 0 ° ◆ , 18 ° ■ , 40 ° ▲ and 70 ° ● angled films. Measurements were taken from 5 mm × 5 mm chips stored at 37 ℃ over a 48-hour period.

ICPMS data showed an increase in the levels of chromium and silver lost from the surface over a 48-hour period for all surfaces. For both metals, the losses from the surfaces were similar with the thin-films deposited at 70 ° showing the greatest losses. Although the material thickness of metal varied between chromium (3 nm) and silver (20 nm), the losses of silver were far higher than for chromium, with the highest loss of silver being measured at 1563 pg (± 3 pg) in comparison to 77 pg (± 2 pg) of chromium. Measuring silver and chromium losses from the thin-films did not provide any further information on the exposed surface composition of silver and chromium.

Chapter 5. Results and Discussion: Bacterial Interactions with Fabricated Surfaces

This chapter examines the interactions of the thin-films with E. coli and S. aureus. Incubation of these bacteria with the thin-films showed that all nanostructured thin-films had an antimicrobial effect against solution and surface bound bacteria. The highest levels of antimicrobial activity were observed for the thin-films with the greatest surface roughness. Using silver and chromium thin-film coated quartz crystal rate monitor, incubation of the thin-films in the bacterial solutions showed that over a 48-hour period, surface fouling increased. This was correlated to a decrease in antimicrobial activity of the thin-films. To determine that the antimicrobial effect of the thin-films was not a consequence of silver or chromium desorption, ICPMS values of desorbed metals were tested for antimicrobial activity. No antimicrobial activity was observed for chromium and a limited amount of activity was observed for silver. No measurement was carried out for the effect of exposed surface bound chromium and potential subsequent antimicrobial activity.

5.1. Biological Reproducibility

For experimental rigour each series of biological measurements was carried out in triplicate, for each of the nanostructured surfaces, with both *E. coli* and *S. aureus*. Data points were analysed and averaged with standard deviations (sd) calculated using the formula (Miller and Miller, 1993):

$$sd = \sqrt{\frac{\sum_{i}\left(x_i - \bar{x}\right)^2}{\left(n - 1\right)}} \tag{27}$$

Where x_i is each value within the sample, n is the number of values in the sample and $\bar{x}$ is the averaged mean of the sample.

5.2. Solution Based Antimicrobial Activity

The antimicrobial effect of the silver coated silicon dioxide chips was examined by incubating the chips in a broth inoculated with either *E. coli* and *S. aureus* over a 48 hour-period. Figure 38 shows raw optical density data for the *E. coli* growth broth growth with no thin-film coated chips present. This data showed the consistency in population growth behaviour observed across all normalised bacterial growth plots. It also showed the lag, exponential and stationary stages associated with bacterial growth.

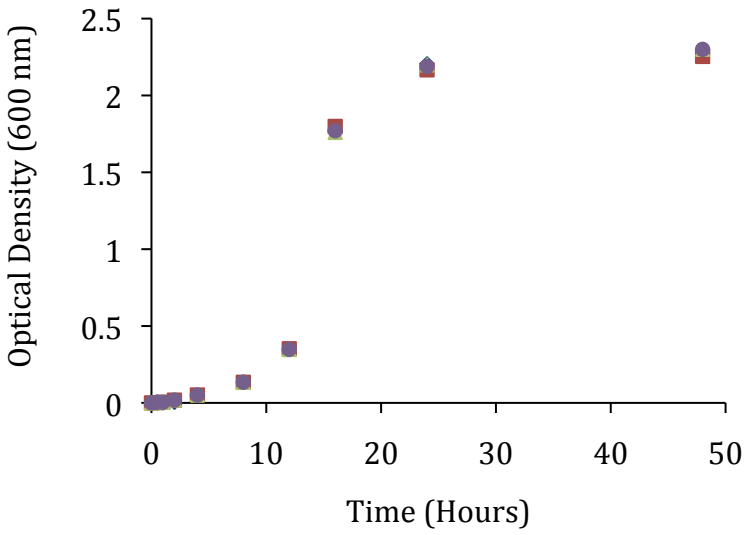

Figure 38. Raw data optical density of E. coli growth at 37 ° C over a 48 hour-period. Three readings were taken at 600 nm - reading 1 reading 2 and reading 3 that were averaged

Normalised solution based optical density measurements were collected for both bacterial samples over this time period and are shown in figures 39 and 40. The data was analysed by normalisation using the respective raw data growth curves for *E. coli* and *S. aureus* without chips and with uncoated chips. This produced maximum growth curves, with silver structured chips producing reduced growth curves. The percentage reduction in growth for the nanostructured surfaces was attributed to antimicrobial activity, shown in figures 41 and 42.

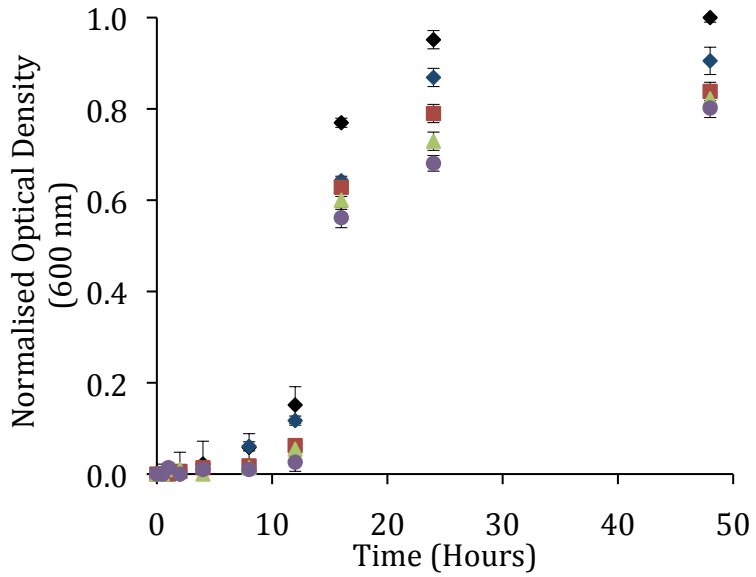

Figure 39. Normalised E. coli growth curves. E. coli cells were incubated at 37 ° over a 48 hour-period, with angled silver surfaces of 0 ° ◆ , 18 ° ■ , 40 ° ▲ and 70 ° ● . Optical Density measurements at 600 nm were taken over this period, with all results being recorded in triplicate. A positive control (averaged growth of bacteria with uncoated silicon dioxide chips present and with no chips) is also shown ◆ . Measurements were carried out in triplicate.

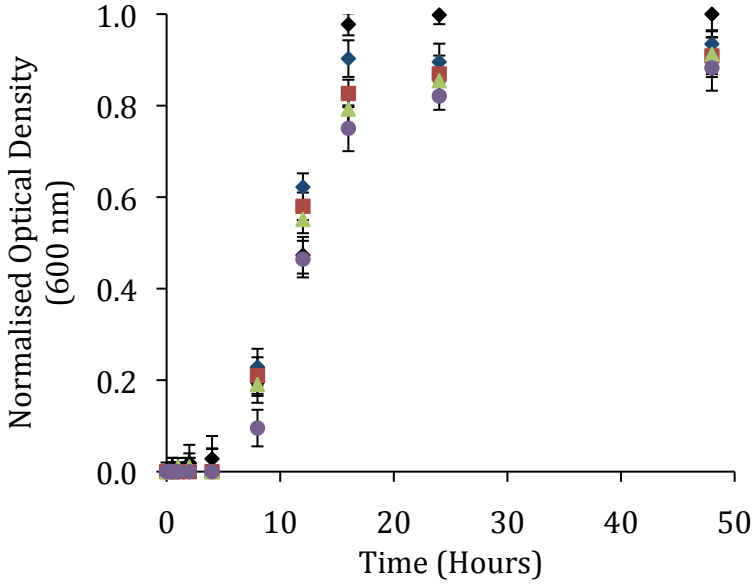

Figure 40. Normalised S. aureus growth curves. E. coli cells were incubated at 37 ° over a 48 hour-period, with an angled silver surface of 0 ° ◆ , 18 ° ■ , 40 ° ▲ and 70 ° ● . Optical Density measurements at 600 nm were taken over this period, with all results being recorded in triplicate. A positive control (averaged growth of bacteria with uncoated silicon dioxide chips present and with no chips) is also shown ◆ . Measurements were carried out in triplicate.

The optical density measurements showed that both *E. coli* and *S. aureus* populations displayed sigmoidal growth for all samples with clear lag, exponential and stationary phases observed in with the typical behaviour described earlier in chapter 2. The positive controls (*i.e.* no antimicrobial material to inhibit bacterial growth) showed the highest optical density over the 48-hour period, indicating the largest bacterial population both types of bacteria.

Growth of the bacterial populations was detrimentally affected in all cases when a silver coated chromium surface was present. The effect was smallest for the smoothest surfaces and increased with increasing roughness of the surfaces, indicating that increasing surface roughness enhances antimicrobial activity.

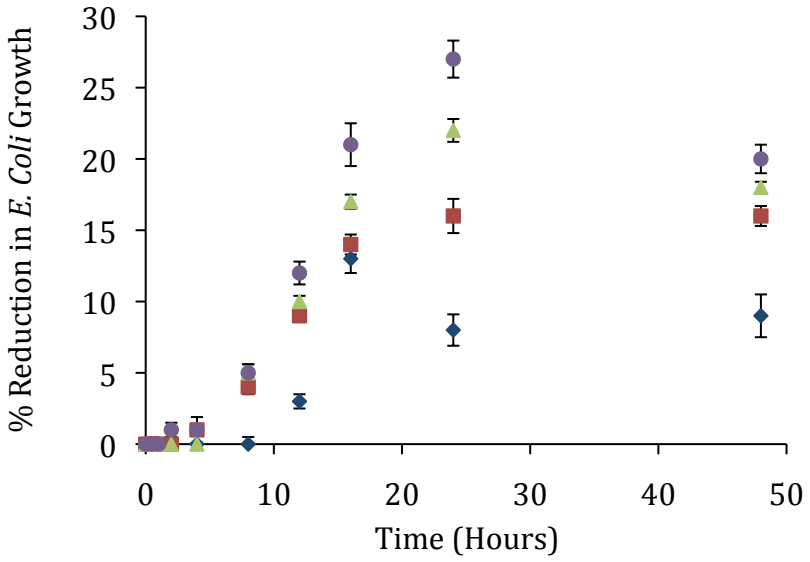

Figure 41. Reduction in E. coli growth. Data from figure 39 was used to calculate the reduction in growth. The effect of silver angled surface deposition of 0 ° ◆ *, 18 °* ■ *, 40 °* ▲ *and 70 °* ● *and percentage reduction in E. coli growth are shown over a 48-hour period, measured by Optical Density at 600 nm. All results were recorded in triplicate.*

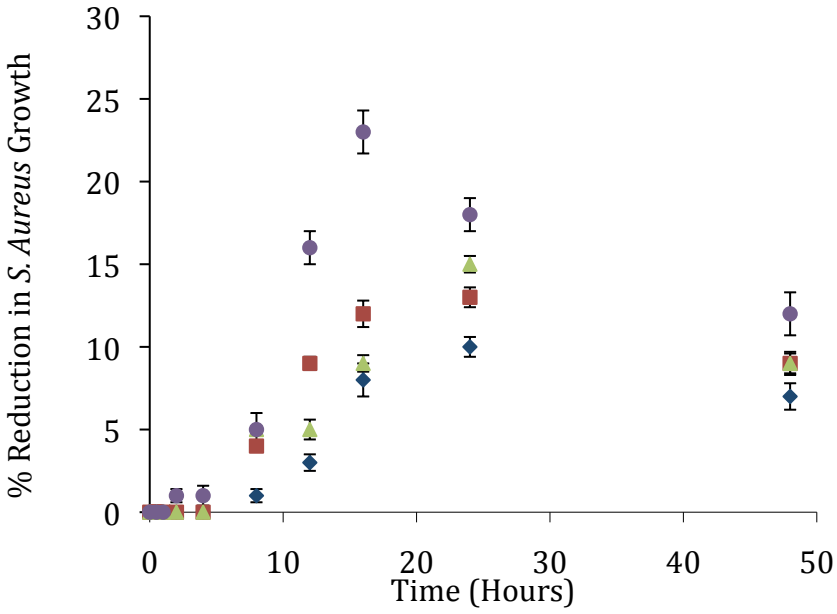

Figure 42. Reduction in S. aureus growth. Data from figure 40 was used to calculate reduction in growth. The effect of silver angled deposition of 0 ° ◆ *, 18 °* ■ *, 40 °* ▲ *and 70 °* ● *and percentage reduction in S. aureus growth are shown over a 48-hour period, measured by Optical Density at 600 nm. All results were recorded in triplicate.*

Antimicrobial activity was measured as the reduction in bacterial growth over this time period with the presence of the silver coated chips in comparison to the positive controls. For both *E. coli* and *S. aureus*, the highest reduction in bacterial was attained with the silver structured surfaces deposited at the highest angle of incidence. The reduction in bacterial density was highest with the roughest surfaces and decreased as surface roughness decreased. For both bacteria, an increase in antimicrobial activity was observed over the first 24 hours for *E. coli* and 18 hours for *S. aureus*. After these times, reductions in antimicrobial activity were measured. This suggests two possible mechanisms, first the surface was fouled by biological material or second the surface effect was 'exhausted' through loss of material from the surface into solution. The silver surfaces showed the highest antimicrobial at an earlier time with *S. aureus*, in comparison to *E. coli* but the antimicrobial effect reduced at an earlier time with *S. aureus*. The greater antimicrobial activity was observed against *E. coli*.

5.3. Desorbed Silver and Chromium Antimicrobial Activity

To ascertain whether these levels of chromium and silver in solution were responsible for the antimicrobial activity, previous measurements of desorbed chromium and silver were used in tests of antimicrobial activity. The highest recorded levels of chromium (77 pg ± 2 pg) and silver (1563 pg ± 3 pg) were added to bacterial broths containing *E. coli* and *S. aureus* over a 48-hour period. Figure 43 shows the percentage reduction bacterial growth resulting from the addition of chromium and silver at the start of the 48-hour period.

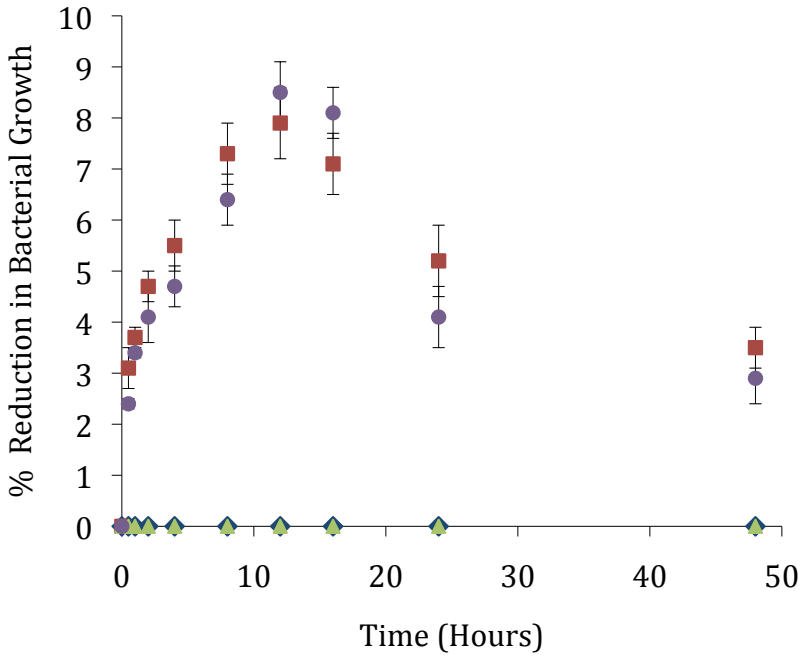

Figure 43. Solution based chromium and silver reduction in bacterial growth. E. coli and S. aureus were grown over a 48-hour period, at 37 ℃ under agitation. The highest cumulative concentration of chromium (77 pg) and silver (1563 pg) were pipetted into the bacterial solutions at time zero, with reductions in bacterial growth being recorded by optical density at 600 nm. The four following solutions were tested: E. coli with 77 pg chromium ▲, E. coli with 1563 pg silver ■, S. aureus with 77 pg chromium ◆ and S. aureus with 1563 pg silver ● . All measurements were carried out in triplicate.

The addition of 77 pg of chromium to bacterial solutions of *E. coli* and *S. aureus* showed no antimicrobial activity. This suggests that the very small loss of chromium from the thin-films was not significant in the antimicrobial behaviour. The addition of 1563 pg of silver did however show reductions in both *E. coli* and *S. aureus* activity. For both bacteria, the silver had an antimicrobial effect throughout the 48-hour period, with the highest reduction in bacterial growth being observed at 12 hours. It is interesting to note that the antimicrobial effect increased up to the 12-hour period and reduced after this time. Importantly the ionic silver loss from all of the surfaces was very similar indicating that the enhanced antimicrobial activity from rough surfaces is not due to increased release of ionic silver. Importantly, the percentage reduction in bacterial growth due to ionic silver also aids in understanding the mechanisms of antimicrobial activity.

5.4. Surface Binding of Bacteria and Antimicrobial Activity

The addition of silver and chromium coated chips into the bacterial broths had the potential of producing antimicrobial activity not only by the release of silver and chromium into solution, contact between the cells and the surfaces, but also with surface bound bacteria. To determine the antimicrobial activity and the percentage of live and dead bacteria on the surfaces, the silver and chromium coated chips were incubated with *E. coli* and *S. aureus* and were examined using Trypan Blue staining and light microscopy on samples taken after over a 48-hour period (figures 44 and 45). In each microscopy count, three areas of 100 μm^2 were recorded for live and dead cells. No fewer than 200 cells were counted for each sample.

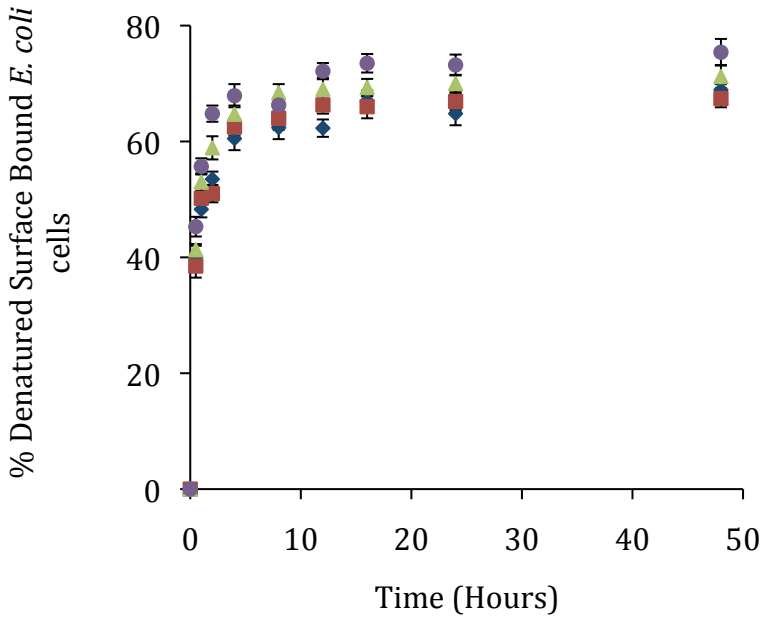

Figure 44. Percentage of denatured E. coli cells bound to the silver surfaces analysed by Trypan Blue staining. The four surfaces of 0 °, 18 °, 40 ° and 70 ° on 5 mm × 5 mm chips were used in broth at 37 °C over a 48-hour period. All measurements were carried out in triplicate, with error bars showing the standard deviation.

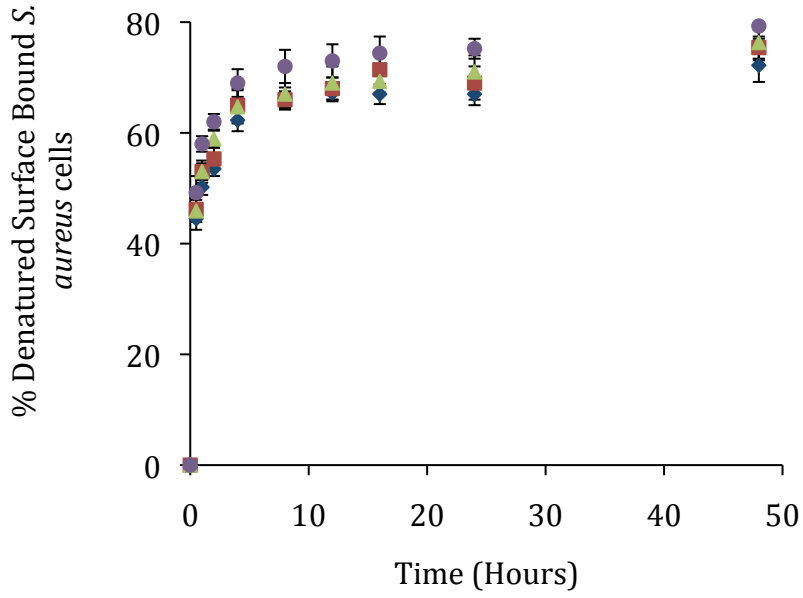

Figure 45. Percentage of denatured S. aureus cells bound to the silver surfaces analysed by Trypan Blue staining. The four surfaces of 0 °, 18 °, 40 ° and 70 ° on 5 mm × 5 mm chips were used in broth at 37 °C over a 48-hour period. All measurements were carried out in triplicate, with error bars showing the standard deviation.

Examination of all structured silver surfaces showed that numbers of denatured 'dead' cells of both *E. coli* and *S. aureus* increased over the 48-hour period. For both *E. coli* and *S. aureus*, the surfaces with the greatest roughness showed the highest levels of antimicrobial activity (> 75 %). It was observed that after 8 hours, the percentage of denatured cells on the surface began to reach a plateau. Comparing the antimicrobial levels between bacteria, the thin-films showed a slightly higher denaturing rate against *S. aureus*. The data suggests that direct interaction with the surface is an important process in the antimicrobial activity of these structured surfaces and that enhanced surface structures increase the antimicrobial activity. One effect of this surface interaction is the trend in both sets of data suggests a fouling of the surface with denatured bacteria. No account was made for potential chromium antimicrobial behaviour by this method.

5.5. Surface Fouling

To determine the level of potential surface fouling from the bacterial broths, silver thin-films were deposited at oblique incidence onto a chromium adhesion layer on top of quartz crystals, used as the sensor in a quartz crystal rate monitor. Frequency shifts (Hz) observed from immersing the thin-film coated quartz crystals in both *E. coli* (figure 46) and *S. aureus* (figure 47) broths over a 48-hour period were used to measure bacterial adsorption. It is worth noting that the original surface of the quartz crystal is not likely to be as smooth as the silicon dioxide used elsewhere in this work.

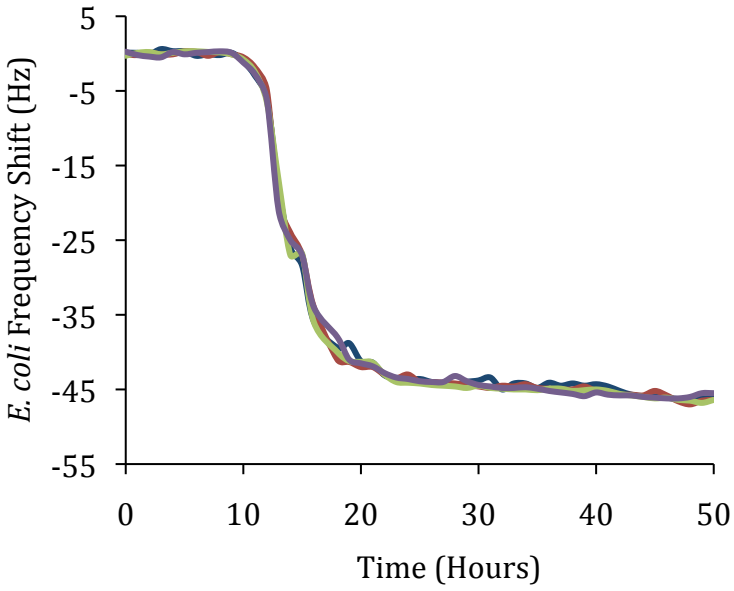

Figure 46. Frequency shifts observed on quartz crystals coated with silver deposition angles of 0 °, 18 °, 40 ° and 70 °, incubated at 37 °C for 48 hours with E. coli. Quartz crystal frequencies were recorded throughout, with measurements being taken in triplicate. Error bars are not large enough to be visible.

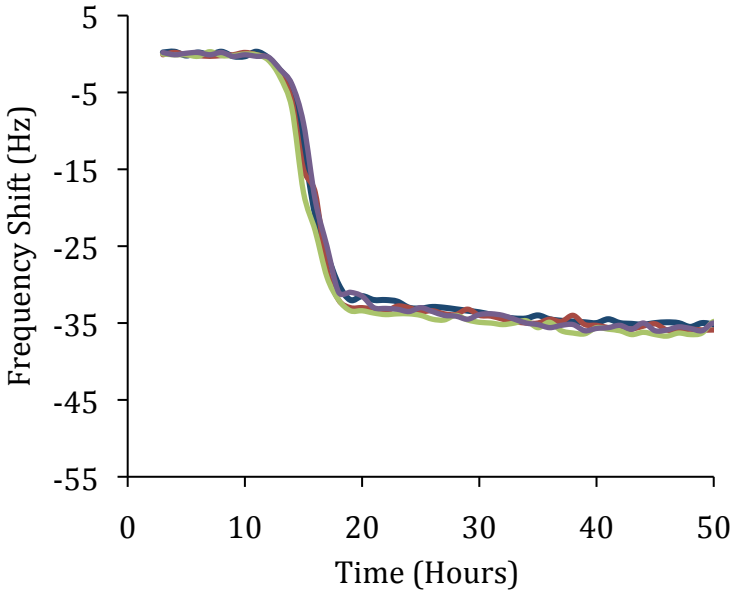

Figure 47. Frequency shifts observed on quartz crystals coated with silver deposition angles of 0 °, 18 °, 40 ° and 70 °, incubated at 37 °C for 48 hours with S. aureus. Quartz crystal frequencies were recorded throughout, with measurements being taken in triplicate. Error bars are not large enough to be visible.

Both *E. coli* and *S. aureus* broth solutions fouled the silver coated quartz crystals. Noticeable fouling and adsorption to the surfaces was recorded after 10-12 hours for both. Exponential mass adsorption occurred over the next several hours, before the surfaces appeared to saturate with bacterial cells at approximately 20 hours. After this time, negligible frequency shifts attributable to adsorption were noted. No difference in adsorption was recorded between the surfaces based on the surface roughness of the silver thin-films. The greatest frequency shifts were observed for *E. coli* cells with over 5 Hz difference between *E. coli* and *S. aureus*.

From the recorded frequency shifts, the effective bound mass was determined using the Kanazawa-Sauerbrey equation. The effective bound mass for both bacterial samples are shown as a function of time in figures 48 and 49.

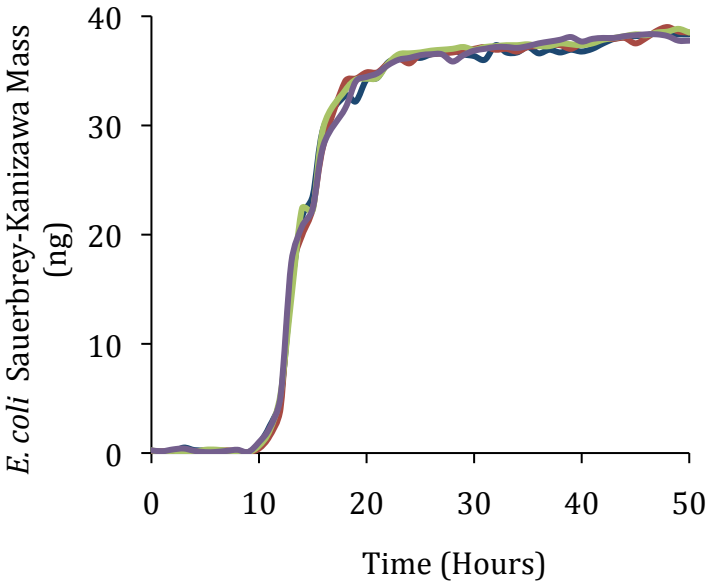

Figure 48. E. coli mass adsorption to silver coated quartz crystal oscillators, calculated from the Sauerbrey-Kanazawa equation. Bacteria were grown in broth and were incubated at 37 °C for 50 hours with an silver coated quartz crystal at the following deposition angles: 0 ° ◆ *, 18 °* ■ *, 40 °* ▲ *and 70 °* ● *. Measurements were taken in triplicate. Error bars are not large enough to be visible.*

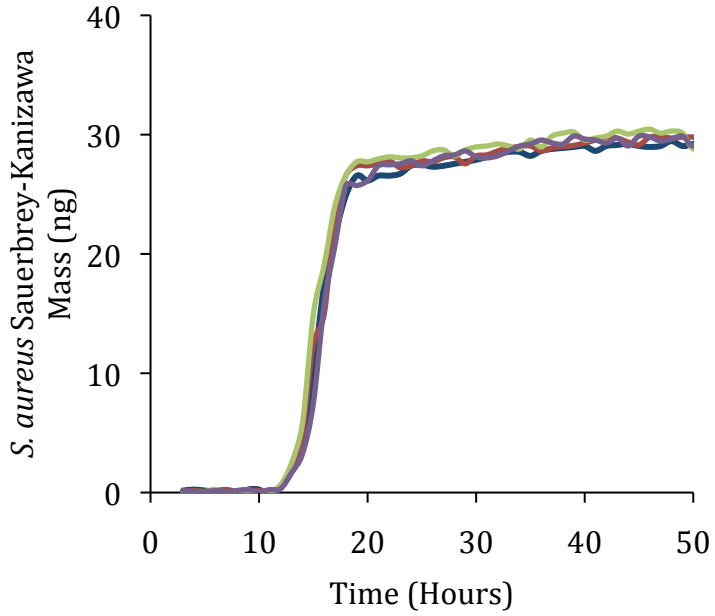

Figure 49. S. aureus mass adsorption to silver coated quartz crystal oscillators, calculated from the Sauerbrey-Kanazawa equation. Bacteria were grown in broth and were incubated at 37 °C for 50 hours with an silver coated quartz crystal at the following depositions angles: 0 ° ◆ *, 18 °* ■ *, 40 °* ▲ *and 70 °* ● *. Measurements were taken in triplicate. Error bars are not large enough to be visible.*

Chapter 6. Results and Discussion: Surface Cleaning and Antimicrobial Activity

In this chapter, the effect of cleaning the thin-film surfaces was examined as a method of increasing the longevity of the surfaces after biological fouling. The thin-films were cleaned three times with IPA, with subsequent antimicrobial activity measurements being recorded alongside changes in thin-film roughness and thickness. After each clean, a minor loss of antimicrobial activity was observed alongside a reduction in film thickness, a reduction in nanostructure size and surface roughness. No account was made for changing the exposed silver and chromium ratios due to cleaning.

6.1. Thin-Film Cleaning and Antimicrobial Activity

Surface fouling from biological materials is problematic for antimicrobial activity and potentially reduces the active area contacting the microorganisms. Commercially and medically, this often results in disposal of a thin-film, cleaning or the re-application of a new surface layer. As disposal and re-application can be costly and not suited to unskilled personnel, a simple cleaning method using IPA was examined to regenerate a fouled surface. The thin-films were examined for loss of nanostructuring and film thickness.

6.2. Surface Structure

Before and after cleaning with IPA, surface roughness (RMS) measurements were taken using a Veeco Nanoscope IV Probe Microscope in a Class 100 clean room. Tapping mode was used to raster scan 5 µm x 5 µm sections of the four fabricated thin-films. These measurements showed that the surface roughness and nano-structures changed after each clean. Two-dimensional line scans are shown in figure 50.

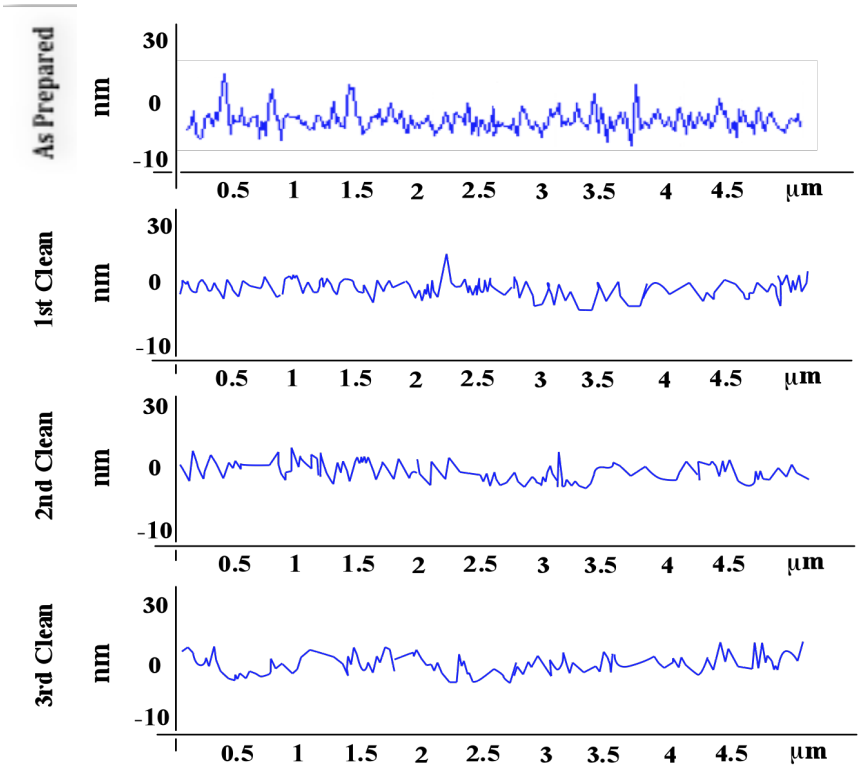

0 ° Deposition

Figure 50. AFM line profiles along the x-axes of 0 °, 18 °, 40 ° and 70 ° silver deposition (20 nm) on top of chromium (3nm), before and after cleaning with 100 % IPA. The images were taken randomly from the AFM scans.

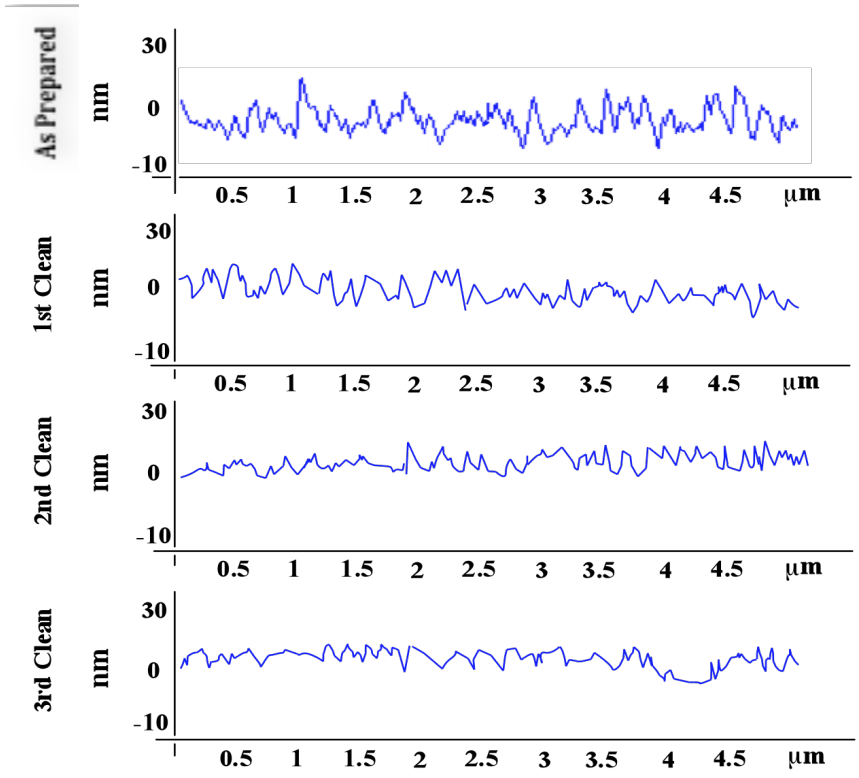

18 ° Deposition

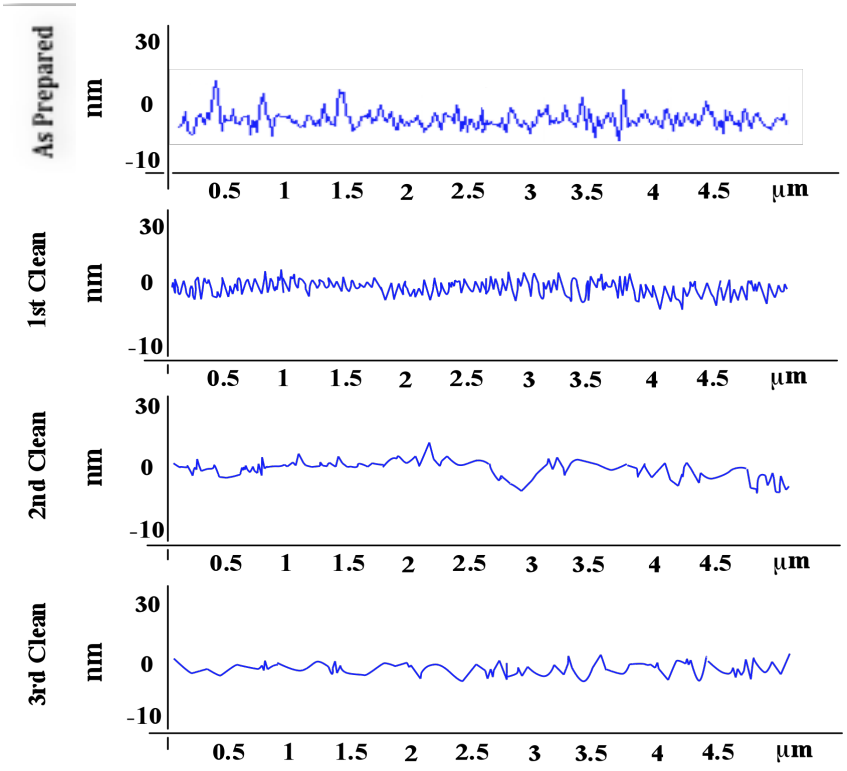

40 ° Deposition

Figure 50. AFM line profiles along the x-axes of 0 °, 18 °, 40 ° and 70 ° silver deposition (20 nm) on top of chromium (3nm), before and after cleaning with 100 % IPA. The images were taken randomly from the AFM scans.

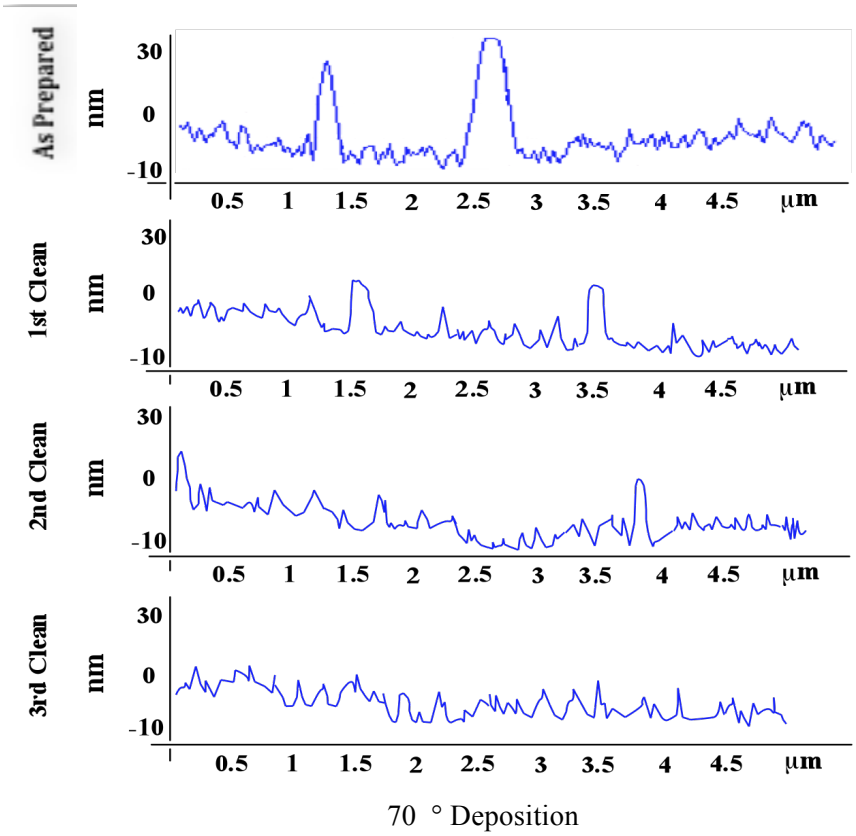

Figure 50. AFM line profiles along the x-axes of 0 °, 18 °, 40 ° and 70 ° silver deposition (20 nm) on top of chromium (3nm), before and after cleaning with 100 % IPA. The images were taken randomly from the AFM scans.

With changes to thin-film thickness and nanostructuring due to cleaning, it is possible that more of the chromium adhesion layer was exposed, which in turn could affect the antimicrobial activity of the thin-films.

Using the VEECO V613r1 software, the RMS surface roughness was calculated from 100 μm^2 areas and is shown in figure 51.

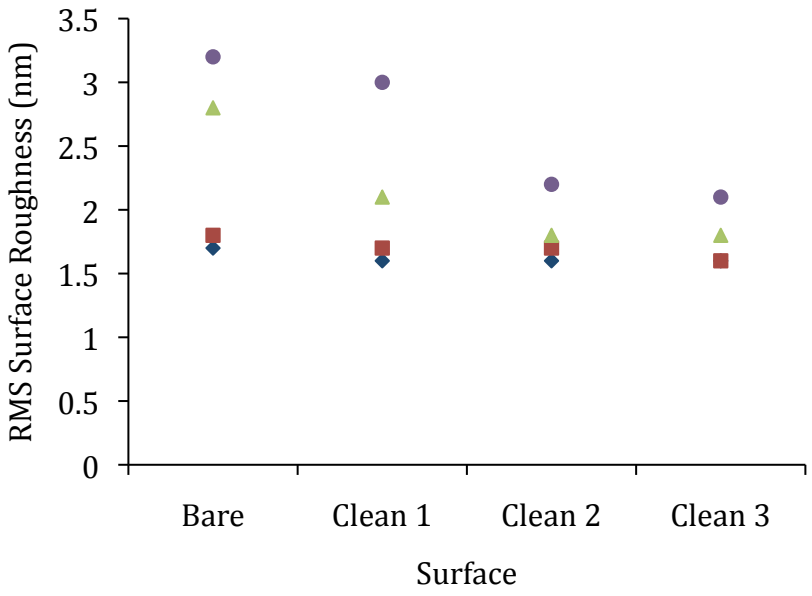

Figure 51. The effect of cleaning on RMS surface roughness. The four silver surfaces deposited at angles of 0 ° ◆ *, 18 °* ■ *, 40 °* ▲ *and 70 °* ● *, had their RMS surface roughness before and after cleaning with 100 % IPA and wiping. This procedure was carried out a total of three times. Error bars were calculated but are not large enough to be visible.*

This figure alongside the line scans shown in figure 50 show that the surface roughness for each nanostructured thin-film decreased after each cleaning stage (with only three cleaning stages being carried out). The greatest decreases in surface roughness were observed for the thin-films deposited at angles of 40 ° and 70 °, which had the largest initial surface roughness before cleaning. With three stages of cleaning, the surface roughness of these two films decreased to levels close to the thin-films deposited at lower angles (18 ° and 40 °). The two thin-films deposited at the lower angles, surface had a negligible surface decrease after cleaning. Using the AFM data, the average peak widths of the nanostructured surfaces were examined (table 3).

0 ° Surface	RMS Surface Roughness (nm)	Average peak width along x axis (nm)	Average peak width along y axis (nm)
As Prepared	1.7	152 ± 4	159 ± 5
Clean 1	1.6	136 ± 5	140 ± 5
Clean 2	1.6	133 ± 4	135 ± 4
Clean 3	1.6	134 ± 3	132 ± 4

18 ° Surface	RMS Surface Roughness (nm)	Average peak width along x axis (nm)	Average peak width along y axis (nm)
As Prepared	1.8	197 ± 7	188 ± 8
Clean 1	1.7	162 ± 7	159 ± 9
Clean 2	1.7	147 ± 6	140 ± 6
Clean 3	1.6	144 ± 7	137 ± 7

40 ° Surface	RMS Surface Roughness (nm)	Average peak width along x axis (nm)	Average peak width along y axis (nm)
As Prepared	2.8	216 ± 3	222 ± 4
Clean 1	2.1	202 ± 8	206 ± 5
Clean 2	1.8	182 ± 6	176 ± 3
Clean 3	1.8	155 ± 3	159 ± 6

70 ° Surface	RMS Surface Roughness (nm)	Average peak width along x axis (nm)	Average peak width along y axis (nm)
As Prepared	3.2	341 ± 5	313 ± 5
Clean 1	2.9	288 ± 5	270 ± 4
Clean 2	2.5	215 ± 4	191 ± 3
Clean 3	2.0	184 ± 6	169 ± 5

Table 3. The RMS and average peak width of the large intermittent peaks measured at the half maximum (FWHM) across the AFM profiles. Measurements were taken along the slope of deposition for x-axes for 20 nm silver deposited on 3 nm chromium at the angles of 0 °, 18°, 40 ° and 70 °, before and after cleaning with 100 % IPA and wiping.

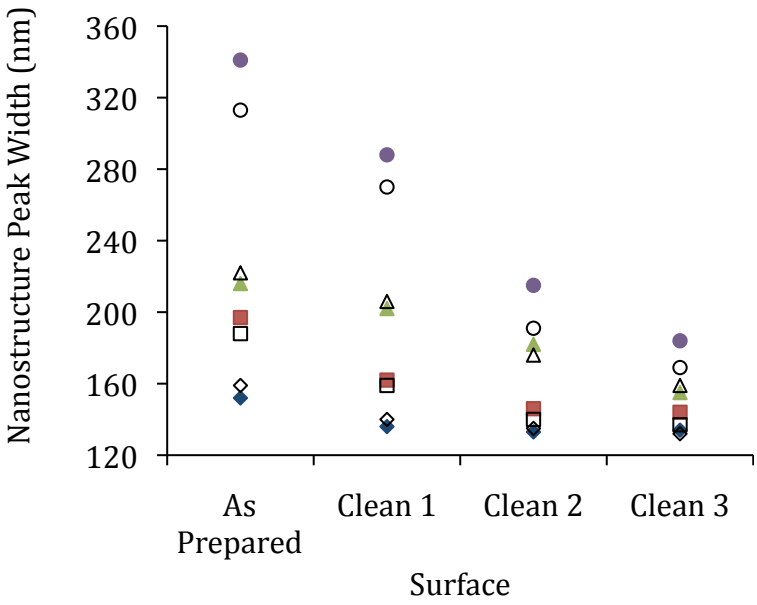

Figure 52. Average width of the large intermittent surface peaks measured at the half maximum (FWHM) from AFM profiles measured after cleaning, up to three times with 100 % IPA. The four deposited silver surfaces, were measured in both x: 0 ° 18 ° 40 ° 70 ° and y-dimensions: 0 ° 18 ° 40 ° 70 °

Examination of figure 52 shows a decrease in the large intermittent peak half maximum measurements for nanostructures in both *x* and *y*-axes, with cleaning. This trend was observed for all deposition angles and with subsequent decreases in FWHM after each of the three cleaning stages.

6.3. Material Thickness after Cleaning

To determine whether the cleaning process to remove fouling was reducing the thin-film thickness, measurements were carried out using RBS and an ellipsometer. Measurements were taken on unmodified silver thin-films taken from the thermal evaporator, within 30 minutes of evaporation. After initial measurements of the unmodified surfaces the surfaces were cleaned three times as detailed in section 4.2, with ellipsometer, RBS and quartz crystal rate monitor measurements being taken after each cleaning stage (figure 53). All three measurements showed that cleaning reduced the thin-film thickness. The greatest reduction in film thickness was observed with the lower deposition angles of 0 ° and 18 °. Interestingly, even after three cleaning procedures, the thin-film thickness was not measured below 4 nm. It is speculated that reducing the film thickness, has a potential to increase the exposure of the chromium adhesion layer to bacterial cells.

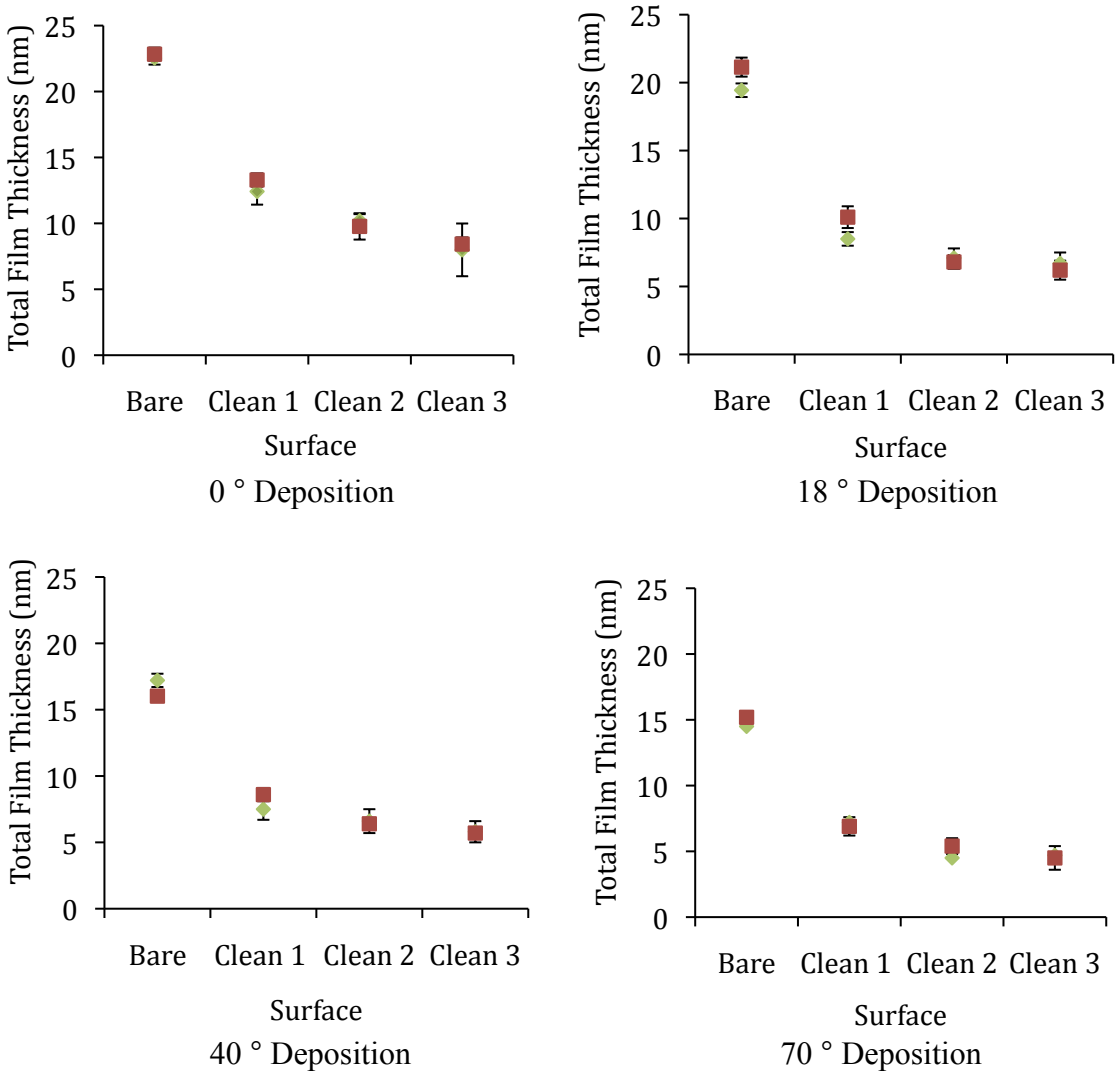

Figure 53. Total film thickness (nm) of a 23 nm film (3 nm chromium and 20 nm silver) deposited onto silicon dioxide, (defined as bare) with three IPA cleaning steps. The film thickness was measured ■ by RBS and ▲ ellipsometry after each cleaning step.

6.4. Effect of Cleaning on Fouled Thin-Films

Prior to the cleaning procedures, the nanostructured silver thin-films had shown the following antimicrobial trends for both *E. coli* and *S. aureus* and 70 ° > 40 ° > 18 ° > 0 °. Although the surface roughness decreased for each thin-film surface after each cleaning procedure, these trends were maintained and are shown with *E. coli* and *S. aureus* in figure 54 and 55 respectively. The shape of the antimicrobial curves showed little variation other than a reduction in antimicrobial activity after each subsequent cleaning stage. Each cleaning procedure was shown to reduce the antimicrobial activity of all the thin-films against *E. coli* and *S. aureus*, which led to a total reduction in activity between 50 – 80 %, by the end of the third clean.

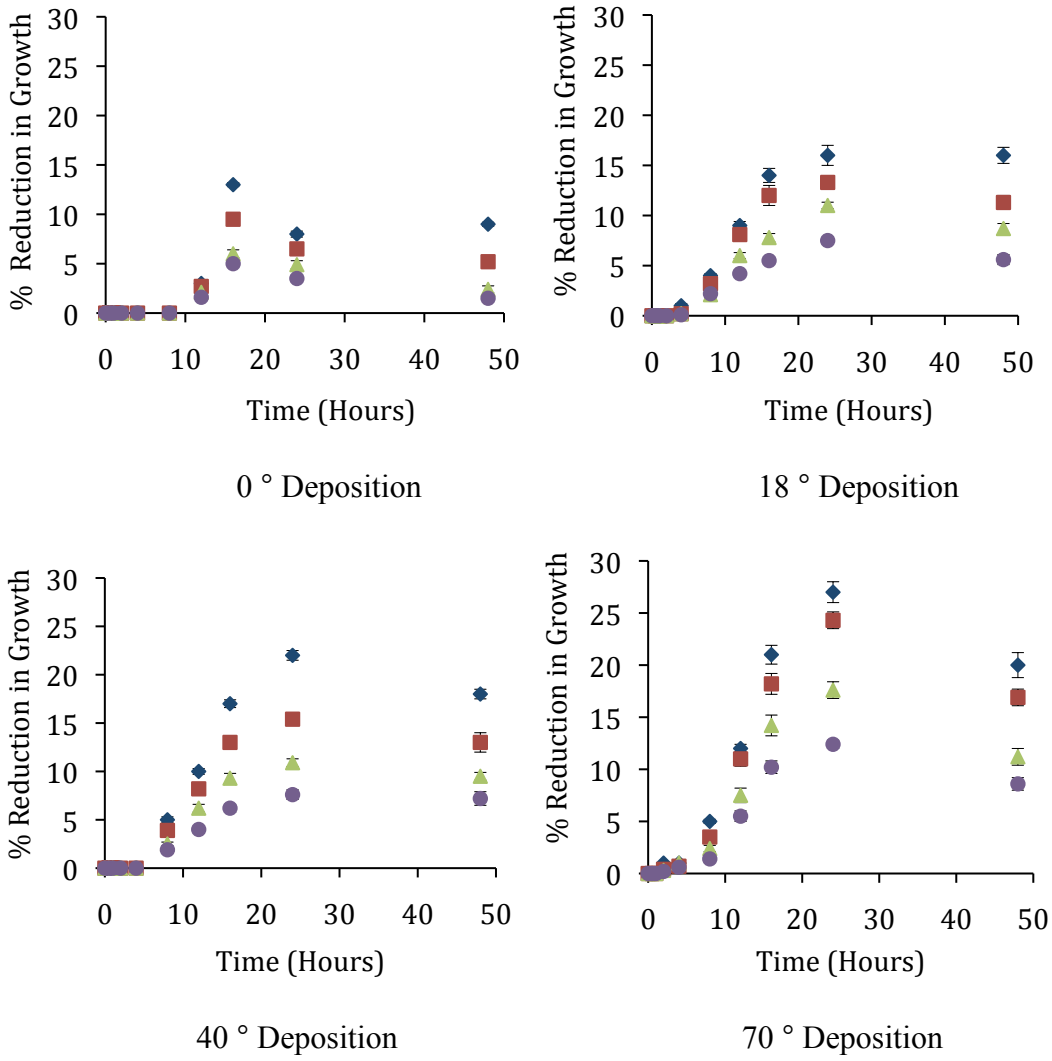

Figure 54. Effect of IPA cleaning on silver mediated, E. coli antimicrobial activity. E. coli was incubated at 37 °C for 50 hours with 5 mm x 5 mm silver coated chips deposited at different angles. Three IPA cleaning procedures were carried out, with antimicrobial activity being measured for a bare ◆ surface, after one ■ two ▲ and three ● cleaning procedures. All measurements were carried out in triplicate.

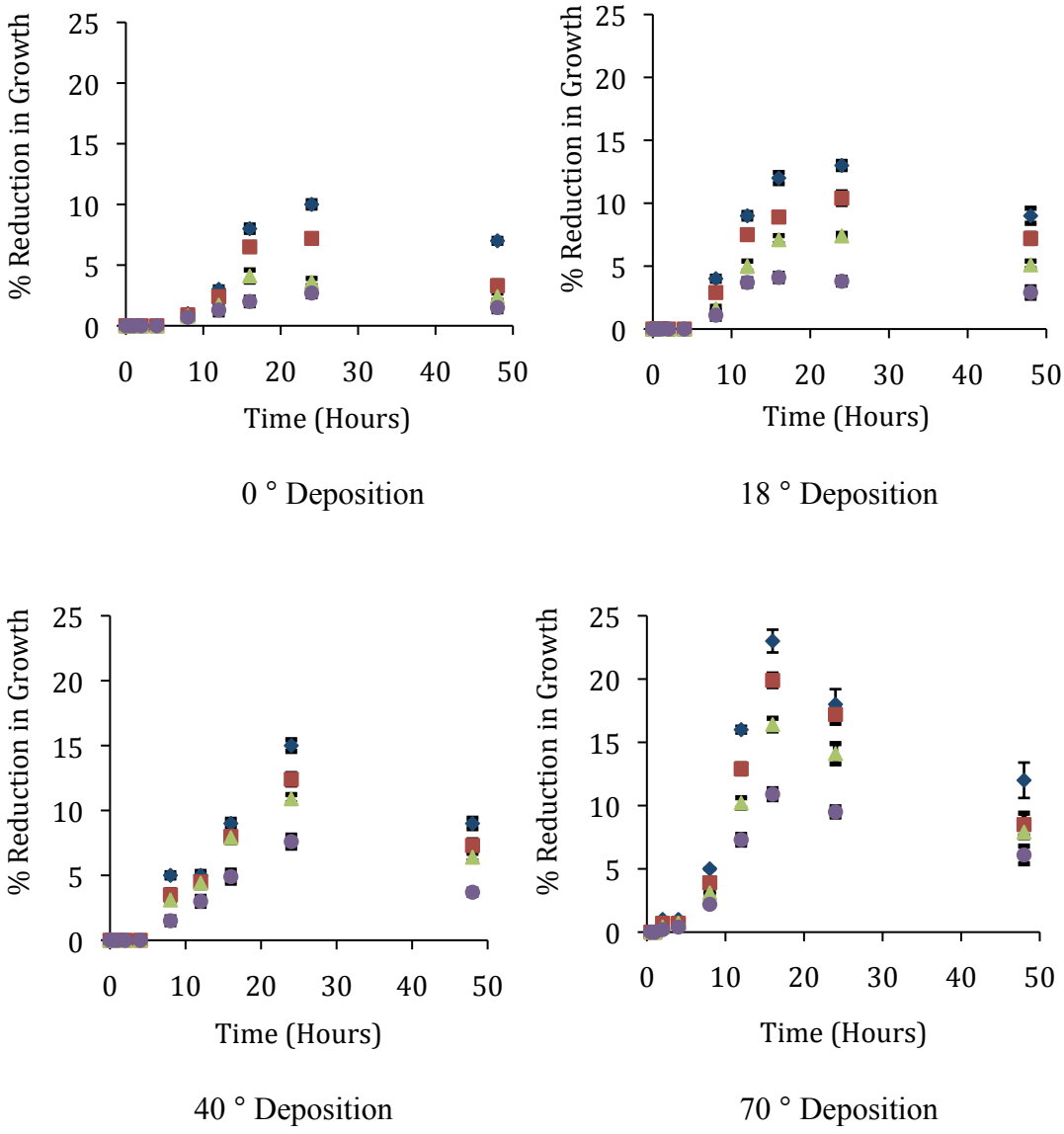

Figure 55. Effect of IPA cleaning on silver mediated, S. aureus antimicrobial activity. S. aureus was incubated at 37 °C for 50 hours with 5 mm x 5 mm silver coated chips deposited at different angles. Three IPA cleaning procedures were carried out, with antimicrobial activity being measured for a bare ◆ surface, after one ■ two ▲ and three ● cleaning procedures. All measurements were carried out in triplicate.

Chapter 7. Conclusions

In this chapter, an overview of this work is carried out, with consideration of main findings and limitations that will be used to suggest future work in Chapter 8.

7.1. Thin-Film Fabrication and Characterisation

This is a complex interdisciplinary study, which has some clear results and has led to a number of open questions for future work. The aim of this study was to understand the influence of nanoscale structuring to enhance the antimicrobial activity of silver thin-films that could be reused after biological fouling. Oblique angle thermal evaporation is a low cost and potentially simple method for nanostructuring surfaces and was used throughout this study. The structure of the thin-films were measured using a variety of techniques to obtain thickness, surface roughness, ambient contamination and antimicrobial activity against two model bacteria – *E. coli* (Gram negative) and *S. aureus* (Gram positive).

The use of oblique angle deposition at increasing angles was expected to produce different surface topographies, based on the angle of deposition, and in this study was measured by AFM. This showed that the surface roughness increased with an increase in deposition angle. Interestingly, above 40 ° sharp peaked features were observed, with the most pronounced nanostructuring being observed at 70 °. At this angle of deposition, the nanostructuring was almost three times greater than at

any lower angle. It is likely that the increase in peak height of nanostructures at higher deposition angles is due to the effect of shadowing during the thermal evaporation process. SEM of the thin-films also showed an increase in nanostructuring with deposition angle.

Further examination of the thin-films by RBS and ellipsometry showed that as the angle of material deposition increased, thin-film thickness decreased. It is speculated that the film thickness decreased as a consequence of shadowing and steering, which resulted in less material being uniformly deposited but would lead to increased nanostructuring. Further to this, measurements of rough surfaces can become more complex for RBS and ellipsometry, particularly with such low level of material deposition. It is also possible that at higher angles of deposition, a greater number of atoms missed the target surface, which led to the films being of reduced thickness. Although the increased nanostructuring and surface roughness was coupled with thinner films, it was not believed to be a detriment to the antimicrobial activity of the thin-films. The concerns for reduced thickness are potentially problematic for cleaning the surfaces, which removes part of the thin-film.

In ambient conditions, silver is capable of undergoing various chemical reactions, with some of the most common being oxidation and fouling with reactive molecules via metal-ligand reactions. To assess the changes to the thin-films from these effects, post thin-film deposition growth was measured by ellipsometry over a 16-week period and for each nanostructured thin-film showed an increase in the thickness in all thin-films over this period. Using ellipsometry, it was not possible

to ascertain the topography of the metal oxidation. Interestingly, the greatest increase in post-evaporation thin-film growth was observed with the films deposited at the lowest angles and had the thickest films before ambient growth. This may be attributable to the thickest films having more material to undergo oxidation and bind incoming contaminating molecules. Although, measurements were carried out to assess the rate and thickness of ambient condition thin-film growth, no measurement was carried out on the subsequent effect on antimicrobial activity, film stability and cleaning. This was coupled with no work being carried out to assess the ratio of exposed silver and chromium with subsequent antimicrobial effects.

7.2. Bacterial Interactions with Thin-Films

Silver surfaces have the potential to denature bacterial cells in solution by the release of ionic silver (Williams *et al*, 1989), release of nanoparticles (Maneerung *et al*, 2008; Stevens *et al*, 2009), through surfaces structures that act as spikes (Liu *et al*., 2009) and by adsorbing the cells onto the surface. The chromium adhesion layer also has a potential antimicrobial effect (Dreyfuss, 1964).

Measurement of *E. coli* and *S. aureus* optical density for 48 hours with the thin-films was used to produce bacterial growth curves over this time, including the lag, exponential and stationary phases. Using the growth curves, the percentage reduction in solution antimicrobial activity for each thin-film was calculated. This showed that as the surface roughness increased, the percentage reduction in

antimicrobial activity for both bacteria increased. The highest level of antimicrobial activity was observed with *E. coli*, which has a thinner cell envelope than *S. aureus*. For both bacteria though, the antimicrobial activity was not uniform over the 48-hour period, with reductions taking place after 24 hours for *E. coli* and 18 hours for *S. aureus*. A limitation of using optical density, as a method of determining antimicrobial activity via growth curves is that the information shows only a reduction in the growth of cells and not the number of live and denatured bacteria. Further work, would see samples of bacteria being removed from the broth, with Trypan Blue being added, to determine the live and denatured ratios for each thin-film.

As the antimicrobial activity of the thin-films reduced after 24 hours for *E. coli* and 18 hours for *S. aureus*, quartz crystals had silver thin-films deposited on them to measure potential surface fouling by bacteria. The quartz crystals were incubated with both bacteria for 48 hours and showed fouling for all thin-films, with fouling increasing with surface roughness. Considering the small size of the nanostructures in comparison to the size of the bacterial cells, it is not believed that the increased surface area from the nanostructures created a larger surface area for adsorption. It is speculated however that the surfaces with the greatest number of nanostructured fouled most easily due to their higher level of antimicrobial activity, due to an increased number of denatured cells and debris. This has not been tested, but using an environmental SEM, or Trypan Blue with a light microscope, it would be possible to determine if this is the case.

Comparing the surface fouling with the percentage of thin-film antimicrobial activity it was observed that after the highest levels of antimicrobial activity had occurred, surface fouling reached a maximum. This suggests that fouling is a limiting factor in silver nanostructured antimicrobial activity.

Although the thin-films had shown antimicrobial activity against *E. coli* and *S. aureus* in solution, it was not known what effect if any, desorbing chromium and silver ions had on the bacteria. The release of chromium and silver into solution was measured by ICPMS over a 48-hour period. This data showed increasing losses of chromium and silver from the thin-films, which were higher as the surface roughness increased. The highest cumulative losses from the films were measured from the 70 ° films, at 77 pg for chromium and 1563 pg for silver. To determine the antimicrobial effect of these metals, they were incubated with *E. coli* and *S. aureus* for 48 hours. Exposure of the bacteria to chromium showed no antimicrobial activity, whereas silver showed the following antimicrobial rates: 8.5 % with *E. coli* and 8 % with *S. aureus*. Interestingly, a reduction in antimicrobial activity was observed with both bacteria after 18 hours, suggesting an exhaustion of silver ions. This could be verified by ICPMS.

The addition of silver coated chips into the bacterial broths had the potential of producing antimicrobial activity not only by the release of silver into solution, contact between cell and surface but also through cellular adsorption. To determine the antimicrobial activity and the percentage of live and dead bacteria on the surfaces, the silver coated chips were incubated with *E. coli* and *S. aureus* and were examined with Trypan Blue using a light microscope over a 48-hour

period. All thin-films showed a high denaturing rate of both bacterial cells, with the roughest surfaces producing the highest denaturing rates at over 75 %. The increased denaturing rates observed at the higher surface roughness suggest that the nanostructuring on the surfaces enhanced the antimicrobial activity of silver. It would be of great benefit to this study to be able to determine the percentage of denatured cells that were in direct contact with the silver surfaces. It would also show if multiple cell layer binding inhibited the uppermost layers from being denatured. No account was made for potential exposure of chromium, which could vary as a consequence of angled deposition.

7.3. Thin-Film Cleaning and Antimicrobial Activity

Surface fouling from complex biological species can result in adsorbed biological layers that reduce the activity of the surface. For nanostructured surfaces produced under vacuum conditions, it is often not a simple or cost effective task to reapply a layer, when fouling has occurred. Many cleaning regimes would also damage the nanostructuring and also be problematic for non-skilled operators to use, thus reducing the commercial potential. The challenge for a cleaning procedure is to remove the fouled layer but maintain the antimicrobial activity of the surface. With this remit, IPA surface wiping was examined for removal of biological fouling and to understand the effect of cleaning on the thin-film surface and antimicrobial activity. To showcase multiple cleaning regimes each surface was cleaned three times.

AFM imaging of the thin-films showed a decrease not only in surface roughness after each clean but also peak width. The greatest reductions in surface roughness and peak width were observed with the thin-films that had the greatest surface roughness and peak widths before cleaning. These reductions suggest the loss of material from the thin-films. To determine if material had been lost during cleaning, the films were examined using RBS and an ellipsometer between cleaning. For all surfaces examined, the cleaning process was shown to reduce the film thickness after each clean. The greatest losses of film thickness were shown with the thin-films deposited at the lower angles of 0 ° and 18 °, which were the films with the greatest thicknesses before cleaning.

As the characterisation of the thin-films showed a reduction in surface roughness, peak nanostructure widths and a loss of material from the films, the antimicrobial behaviour of the films after cleaning also needed to be examined. Incubation of the thin-films with *E. coli* and *S. aureus* subsequent cleaning showed a reduction in antimicrobial behaviour for all thin-films with both bacteria. The reduction of antimicrobial activity was observed after each clean for each thin-film. The most pronounced decreases were observed for the thin-films with the greatest levels of nanostructuring, with the thin-film deposited at 70 ° having its antimicrobial activity reduced from 27 % to 11 % by the third clean against *E. coli*. The thin-films deposited at lower angles showed proportionally lower reductions but had little antimicrobial activity left by the third clean. This was shown from the film deposited at 0 ° which had could produce only a 3 % reduction by the third clean against *E. coli*. Interestingly, although the percentage reduction in antimicrobial activity fell, the shape of the antimicrobial curves over the 48-hour periods varied

little. This suggests that the process of fouling still occurred for each film after cleaning. No assessment was made of cleaning and antimicrobial behaviour for bacteria adsorbing directly onto the thin-film surfaces.

Even through the surface nanostructuring was reduced after each clean, it still showed enhanced activity in comparison to lower structured/smoother surfaces. The use of IPA wiping may not be the optimal method for cleaning but suggests that simple chemical and mechanical cleaning is a viable method for removal of biological fouling, with a nanostructured surface.

Chapter 8. Future Work

Limitations often lie within material constraints for nanostructure fabrication and their use with biological systems. Such constraints include, the antimicrobial properties of the material, ability to be fouled, cleaned, toxicity to higher organisms and economic considerations. In this study, only silver was examined against the relatively non-pathogenic bacterial species of *E. coli* ATCC 10536 and *S. aureus* ATCC 6538. One of the most pertinent expansions of this work would be the testing of silver nanostructured surfaces against more pathogenic strains of these bacteria, potentially including *E. coli* 0157:H7 and methiciliin resistant *S. aureus* (MRSA). Such work would have great clinical relevance as bacteria such as *E. coli* 0157:H7 and MRSA, are of great concern due to their high pathogenicity and resistance to many clinical antimicrobial agents.

The claim made in this study that nanostructured surfaces enhance antimicrobial activity must be more deeply interrogated. Results from within this study have shown that nanostructuring is capable of enhancing antimicrobial activity, but the questions that follow are: what is it about nanostructuring that enhances antimicrobial activity, and by what mechanism? Looking at the work of (Liu *et al*., 2009), surface spikes are capable of puncturing and denaturing bacterial cells and it is suggested that this is the mechanism by which the antimicrobial activity occurs. It is however unknown if the silver nanostructures denature the cells simply by irreparably puncturing the bacterial cell envelopes or whether more complex mechanisms are in place, such as ionic release from the nanostructures into the cells, which results in the cells denaturing. It would be interesting to

remove denatured cells from solution after exposure to the thin-films and examine the level of silver bound externally and internally to the cells by elemental analysis or ICPMS. Likewise the use of UV-visible spectroscopy could be of great use to determine if the cells are being punctured. Current literature suggests that if punctured, the cells would lyse and release their cytoplasmic constituents (including DNA and RNA), which absorb strongly at an absorbance of 260 nm (Liu *et al*., 2009).

The use of ICPMS in this study has confirmed that it is not simply silver release from the thin-films that are denaturing the bacterial cells, but these results indicate that part of the antimicrobial activity is linked to this release. This raises the further question of what percentage of antimicrobial activity can be attributed to nanostructuring. To answer this more fully, other factors not examined in this study must be taken into account. The first is surface area and which it can be assumed that increasing the area of an antimicrobial film in contact with bacteria would increase the antimicrobial effect. Due to the size of the nanostructures and the bacterial cells (less than 27 nm in height for the nanostructures and micrometre dimensions for the bacteria), it is speculated that this had little effect due to steric hindrance from the larger size of the bacteria. ICPMS data also showed little difference between the thin-film nanostructures and the release of silver, indicating this factor was negligible. To examine this further though, it would be interesting to calculate the different surface areas of the nanostructured thin-films. The second factor of great interest is the form of silver desorbing from the thin-films in solution. Using ICPMS, it was not possible to determine if the silver was ionic or if the nanostructures had also desorbed. It is suggested that the

use of DLS would be able to determine if nanostructures had been released from the surface, which could mimic nanoparticles. Perhaps one of the most pertinent tests for nanostructures enhancing antimicrobial activity would be the use of a non-antimicrobial material that could be nanostructured and exposed to bacteria.

Perhaps beyond the scope of this study, but of great interest commercially and medically is the issue of toxicity, particularly for higher organisms. The incubation of the nanostructured thin-films with mammalian cells as a model for higher organism toxicity would determine the applicability of nanostructured thin-films for medical and commercial usage. It would be of interest to examine the effect of IPA cleaning on changing the surface area of exposed chromium, due to chromium being antimicrobial.

References

Aiyar, J., Berkovits, H. J., Floyd, R. A., Wetterhahn, K. E. (1991). Reaction of chromium (VI) with glutathione or with hydrogen peroxide: Identification of reactive intermediates and their role in chromium (VI)-induced DNA damage.

Alameda, J. M., Carmona, F. (1996). Effects of the initial stages of film growth on the magnetic anisotropy of obliquely-deposited cobalt thin films. *J. Mag. Magn. Mater*. **154**. 249.

Albanese, A., Sykes, E. A., Chan, W. C. W. (2010). Rough around the edges: The inflammatory response of microglial cells to spiky nanoparticles. *ACS Nano*. **4**. (5). 2490-2493.

Aldrabee, A., Wriekat, A-H. (2011). Archaeometric characterization of ancient glazed pottery sherds from Khirbet Faris, Jordan by inductively coupled plasma mass spectrometry (ICP-MS). *J. Microchem*. **99**. (2). 289-295.

Allison D. P., Hinterdorfer P., Han W. (2002). Biomolecular force measurements and the atomic force microscope. *Curr. Op. Biotech*. **13**. (1). 47-51.

Alexander S., Hellemans L., Marti O., Schneir J., Elings V., Hansma P. K., Longmire M., Gurley J. (1989). *J. Appl. Phys.* **65**. (1). 164-167.

Amar, J. G. (2003). Effects of long-range interactions in metal epitaxial growth. *Phys. Rev. Lett. B*. **67**. 165425-165430.

AshaRani, P. V., Mun, G. L. K., Hande, M. P., Valiyeveettil, S. (2009). Cytotoxicity and genotoxicity of silver nanoparticles in human cells.

Azzam, R. M. A., Bashara, N. M. (1977). Ellipsometry and polarized light. North Holland Publishing Company. New York, USA. **1**, 1.

Bai, S., Li, S., Yao, T., Hu, Y., Bao, F., Zhang, J., Zhang, Y., Zhu, S., He, Y. (2011). Rapid detection of eight vegetable oils on optical thin-film biosensor chips. *Food*. *Cont*. **22**. (10). 1624-1628.

Balazs, D.J., Triandafillu, K., Wood, P., Chevolot, Y., van Delben, C., Harms, H. (2004). Inhibition of bacterial adhesion on PVC endotracheal tubes by RF-oxygen glow discharge, sodium hydroxide and silver nitrate treatments. *Biomaterials*, **25** (2004). 2139-2151.

Ballentine D. S., White R. M., Martin S. I., Ricco A. J., Zellers E. T., Frye G. C., Wohltjen. (1997). Acoustic Wave Sensors. Theory, Design, and physico-chemical applications. *Academic. Press*. **5**. 30-37.

Basso, M, Giarre, L, Dahleh, M, Mezic, I. (1998). Numerical analysis of complex dynamics in atomic force microscopes. *Proc. IEEE. Conf. Control. Appl.* 1026–1030.

Bauchop T., and Elsden S. R. (1960). The growth of micro-organisms in relation to their energy supply. *J. Gen. Microbiol*. **23**, 457-469.

Bennett, J. M. (1992). Recent developments in surface roughness characterization. *Meas. Sci. Tech*. **3**. (12). 1119-1127.

Berger, T. J., Spadaro, J. A., Chapin, S. E., Becher, R. O. (1976). Electrically generated silver ions. *Antimicrob*. *Agents*. *Chemother*. **9**. 357–358.

Beveridge, T. J. (1981). Ultrastructure, chemistry, and function of the bacterial wall. *Int*. *Rev*. *Cytol*. **72**. 229-317.

Beveridge, T. J., (1990). Mechanism of gram variability in select bacteria. *J. Bacteriol*. **172**. (3). 1609-1620.

Beveridge, T. J. (1995). The periplasmic space and the concept of the periplasm in Gram-positive and Gram-negative bacteria. *ASM*. *News*. **61**. 125-130.

Beveridge, T. J. (1999). Structures of Gram-negative cell walls and their derived membrane vesicles. *Am*. *Soc*. *Microbiol*. **181**. (16). 4725-4733.

Beveridge T J. The ultrastructure of gram-positive cell walls. In: Fischetti. V., Novick. R., Ferretti, J., Portnoy, D., Rood, J., editors. (1999). Gram-positive pathogens. Washington. USA. *Amer*. *Soc*. *Microbiol*. Chapter 1. 3–10.

Beverdige, T. J., Graham, A. A. (1991). Surface layers of bacteria. *Microbiology Review*. **55**, 684-705.

Beveridge, T. J., Graham, L. L. (1991). Surface layers of bacteria. *Microbiol*. *Rev*. **55**. 684–705.

Beveridge, T. J., Schultze-Lam, S. (1997). The response of selected members of the *Archaea* to the Gram stain. *Microbiol*. **142**. 2887-2895.

Binnig G., Quate C. F., Gerber C. H. (1986). Atomic Force Microscope. *Phys. Rev. Lett*. **56**. 930-933.

Black, J. G. (2008). Microbiology: Principles and Explorations. John Wiley and Sons, London, UK. **6**. 150-155.

Bosetti, M., Massè, A., Tobin, E., Cannas, M. (2002). Silver coated materials for external fixation devices: in vitro biocompatibility and genotoxicity. *Biomaterials*. **23**.. 887–892.

Bragg P. D., Rainnie, D. J. (1974). The effect of silver ions on the respiratory chain of *Escherichia* coli. Canadian *Journal of Microbiolology*. **20**. 883-889.

Braydich-Stolle, L., Hussain, S., Schlager, J. J., Hofmann, M. C. (2005). In vitro cytotoxicity of nanoparticles in mammalian germline stem cells. *Toxicol*. *Sci*. **88**. 412–419.

Brook, L. A., Evans, P., Foster, H. A., Pemble, M. E., Steele, A., Sheel, D. W., Yates, H. M. (1994). Highly bioactive silver and silver/titania composite films grown by chemical vapour deposistion. *Journal of Photochemistry and Photobiology.* **187**. (1). 55-63.

Brunoldi, G., Guerrieri, S., Alberici, S. G., Ravizza, E., Tallarida, G., Wiemer, C., Marrangon, T. (2005). Self-annealing and aging effect characterization on copper seed thin films. *Microelect. Engin*. **82**. (3-4). 289-295.

Bruckenstein S., Shay M. (1985). Experimental aspects of use of the quartz crystal microbalance in solution. *Electrochim. Acta*. **30**. (10). 1295-1300.

Bubendorff, J. L., Garreau, G., Zabrocki, S., Berling, D., Jaafar, R., Hajjar, S., Mehdaoul, A., Pirri, C. (2009). Nanostructuring of Fe films by oblique incidence deposition on a $FeSi_2$ template onto Si(1 1 1): Growth, morphology, structure and faceting. *Sur. Sci*. **603**. (2). 373-379.

Butt Hans-Jürgen., Capella B., Kappl M. (2005). Force measurements with the atomic force microscope: Technique, interpretation and applications. *Sur. Sci. Rep*. **59**. (1-6). 1-152.

Carja, G., Kameshima, Y., Nakajima, A., Dranca, C., Okada, K. (2003). Nanosized silver-anionic clay matrix as nanostructures ensembles with antimicrobial activity. *Int*. *J*. *Anti*. *Agen*. **34**. (6). 534-539.

Cervantes, C., Campos-Garcia, J., Devars, S., Gutierrez-Corona, F., Loza-Tavera, H., Torres-Guzman, J. C., Moreno-Sanchez, R. (2001). Interactions of chromium with microorganisms and plants. 25. (3). 335-347.

Chládek, M., Valvoda, V., Dorner, V., Holý, C., Grim, J. (1996). Quantitative

study of interface roughness replication in multilayers using X-ray reflectivity and transmission electron microscopy. *App. Phys. Lett.* **69**. (9). 1318-1320.

Checco, A., Cai Y., Gang, O., Ocko, B. M. (2006). High resolution non-contact AFM imaging of liquids condensed onto chemically nanopatterned surfaces. *Ultramicros*. **106**. (8-9). 703-708.

Cho Yoon-Kyoung., Kim S., Kim Y. A., Lim H. K., Lee K., Yoon DaeSung., Lim G., Pak E., Ha T. H., Kim K. (2004). Characterization of DNA immobilization and subsequent hybridization using in situ quartz crystal microbalance, fluorescence spectroscopy, and surface plasmon resonance. *J. Colloid. Interface. Sci*. **278**. (1). 44-52.

Choi, Y. S., Piehler, H. R., Rollett, A. D. (2007). Introduction and application of modified surface roughness parameters based on the topographical distributions of peaks and valleys. *Mat*. *Char*. **58**. (10). 901-908.

Chou, W.L. Yu, D.G., Yang, M.C. (2005). The preparation and characterization of silver-loading cellulose acetate hollow fiber membrane for water treatment. *Polym*. *Adv*. *Technol*. **16**. 600–607.

Clement J. L., Jarrett, P. S. (1994). Antibacterial silver. *Metal-Based Drugs* **1**. 467-482.

Cocherie, A., Robert, M. (2007). Direct measurement of lead isotope ratios in low concentration environmental samples by MC-ICP-MS and multi-ion counting. *Chem*. *Geol*. **243**. (1-2). 90-104.

Coella, R. (1993). The cost of infection in surgical patients: a case study. *Journal of Hospital Infections*. **25**. 239-250.

Coultate, T. P., and Sundaram, T. K. (1975). Energetics of *Bacillus stearothermophilus* growth: molar growth yield and temperature effects on growth efficiency. *J. Bacteriol*. **121**. 55-64.

Das, M. R., Sarma, R. K., Saikia, R., Kale, V. S., Shelke, M. V., Sengupta, P. (2011). Synthesis of silver nanoparticles in an aqueous suspension of graphene oxide sheets and its antimicrobial activity. *Coll*. *Sur*. *B*. *Biointer*. **83**. (1). 16-22.

Davies, J. A., Anderson, G. K., Beveridge, T.J., Clark, H. C. (1983). Chemical mechanism of the Gram stain and synthesis of a new-electron opaque marker for electron microscopy which replaces the iodine mordant of the stain. *J*. *Bacteriol*. **156**. (2). 837-845.

Dedecker, P., Hofkens, J., Hotta, J-I. (2008). Diffraction-unlimited optical microscopy. Materials Today. 11. 12-21.

Deitch, E. A., Marino, A. A., Gillespie, T. E., Albright, J. A. (1983). Silver-nylon: a new antimicrobial agent. *Antimicrobial Agents Chemotherapeutics* **23**. (3) 356-359.

Desiraju, G. R., Steiner, R. (1999). The weak hydrogen bond in structural chemistry and biology. *Oxford Science Publications*. Oxford, UK. **1**, 5-12.

Dibrov, P., Dzioba, J., Gosink, K. K., Hase, C. C. (2002). Chemiosmotic mechanism of antimicrobial activity of Ag^{+} in *vibrio cholerae*. *Antimicrob*. *Agents*. *Chemother*. **46**. 2668-2670.

Donaldson, K., Aitken, R., Tran, L., Stone, V., Duffin, R., Forrest, G., Alexander, A. (2006). Carbon nanotubes: A review of their properties in relation to pulmonary toxicology and workplace safety. *Toxicol*. *Sci*. **92**. 5-22.

Dowling, D. P., Betts, A. J., Pope, C., McConnell, M. L., Eloy, R., Arnaud, M. N. (2003). Anti-bacterial silver coatings exhibited enhanced activity through the addition of platinum. *Sur. Coat*. *Tech*. **163-164**. 637-640.

Dreyfuss, J. (1964). Characterization of a sulfate and thiosulfate transporting system in *Salmonella typhimurium. J. Biol. Chem.* 239. 2292-2297.

Eastwood, D. S. (2010). Grazing incidence X-ray scattering from magnetic thin films and nanostructures. *Durham E-Theses*. **1**. 13.

Eisenhammer, T., Muggenthaler, F. (1994). Deposition of dielectric and metallic materials on thin silver films: in-situ measurement of reflectance and dc-resistance changes. *SPIE*. **2255**. 508-518.

El Badawy, A. M., Silva, R. G., Morris, B., Scheckel, K. G., Suidan, M. T., Tolaymat, T. M. (2010). Surface charge-dependent toxicity of silver nanoparticles. **45**. 283-287.

El Rifai, O. M., Youcef-Toumi, K. (2001). Coupling in piezoelectric tube scanners used in scanning probe microscopes. *Proc. Amer. Cont. Conf.* 3251-3255.

Fan, F. F. -R., Bard, A.J. (2002). Chemical, Electrochemical, Gravimetric, and Microscopic Studies on Antimicrobial Silver Films. *Journal of Physical Chemistry B*. **106**. 279-287.

Feiler A. A., Sahlholm A., Sandberg T., Caldwell K. D. (2007). Adsorption and viscoelastic properties of fractionated mucin (BSM) and boving serum albumin (BSA) studied with quartz crystal microbalance (QCM-D). *J. Colloid. Inter. Sci*. **315**. (2). 475-481.

Fernández, A., Picouet, P., Lloret, E. (2010). Cellulose-silver nanoparticle hybrid materials to control spoilage-related microflora in absorbent pads located in trays of fresh-cut melon. *Int*. *J*. *Food*. *Micro*. **142**. (1-2). 222-228.

Fernández, R. O., Pizarro, R. A. (1996). Lethal Effect Induced in *Pseudomonas aeruglnosa* Exposed to Ultraviolet-A Radiation. *Journal of Photochemistry and Photobiology*. **64**. 334-339.

Fischetti, V. A., Novick, R. P., Feretti, J. P, Portnoy, D. A., Rood, J. I. (2000). Gram-Positive Pathogens. ASM Press. Washington. USA. Chapter 2. Page 12.

Fotiadis, D., Scheuring, S., Müller, S. A., Engel, A., Müller, D. J. (2002). Imaging and manipulation of biological structures with the AFM. *Micron*. **33**. (4). 385-397.

Frederix, P. L. T. M., Akiyama, T., Staufer, U., Gerber, Ch., Fotidadis, D., Müller, D. J., Engel, A. (2003). Atomic Force bio-analytics. *Curr. Op. Chem. Biol*. **7**. (5). 641-647.

Freshney, R. (1987). Culture of Animal Cells: A Manual of Basic Technique, Alan R. Liss, Inc., New York. 117,

Friedrich, T. (1998). The NADH: uniquinone oxidoreductase (Complex I) from *Escherichia coli*. *Biochim*. *Biophys*. *Acta*. **1364**. 134-146.

Fung, R., Huang, S. (2001). Dynamic modeling and vibration force microscope. *ASME. J. Vib. Acoust.* **123**. 502–509.

Garcia, R., Pérez, R. (2002). Dynamic atomic force microscopy methods. *Sur. Sci. Rep*. **47**. (6-8). 197-301.

Georgiev, Y. M., Henschel, W., Fuchs, A., Kurz. H. (2004). Surface roughness of hydrogen silsesquioxane as a negative tone electron beam resist. *Vacuum*. **77**. (2). 117-123.

Ghosh, S., Kaushik, R., Nagalakshmi, K., Hoti, S. L., Menezes, G. A., Harish, B. N., Vasan, H. H. (2010). Antimicrobial activity of highly stable silver nanoparticles embedded in agar-agar matrix as a thin film. *Carb*. *Res*. **345**. (15). 2220-2227.

Giesbrecht, P., Kersten, T., Maidhof, H., Werke, J. (1998). *Staphylococcal* cell wall: morphogenesis and fatal variations in the presence of penicillin. *Microbiol*. *Mol*. *Biol*. *Rev*. **62**.1371–1414.

Glover, J. L., Chantler, C. T., de Jonge, M. D. (2009). Nano-roughness in gold revealed from X-ray signature. *Phys. Lett. A*. **373**. (12-13). 1177-1180.

Graham, L. L., Beveridge, T. J. (1990). Evaluation of freeze-substitution and conventional embedding protocols for routine electron microscopic processing of eubacteria. *J. Bacteriol*. **172**. 2141–2149.

Gupta, A., Agarwell, D. C., Khan, S. A., Tripathi, A., Kabiraj, D., Mohapatra, S., Som, T., Avasthi, D. K., Chauhan, R. S. (2009). SHI Induced surface modifications of immiscible Fe/Bi bilayer system. *Sur. Coat. Tech*. **203**. (17-18). 2399-2402.

Hadley, M. J., Atkinson, R. J., Pollard, J. (2002). Magnetic properties of Co films deposited onto obliquely sputtered Pt underlayers. *J. Mag. Mag. Mater*. **246**. L347.

Hall, R. E., Bender, G., Marquis, R. E. (1987). Inhibitory and cidal antimicrobial actions of electrically generated silver ions. *J. Oral. Max. Sur.* **45**. (9). 779-784.

Harrison, J. J. Ceri, H., Turner, R. J. (2007). Multimetal resistance and tolerance in microbial biofilms. *Nat*. *Rev*. *Microbiol*. **5**. 928–938.

Herrero, J., Guillén, C. (2004). Improved ITO thin films for photovoltaic applications with a thin ZnO layer by sputtering. *Thin*. *Sol*. *Film*. **451-452**. 630-633.

Higgins, M. L., Shockman, G. D. (1976). Study of a cycle of cell wall assembly in *Streptococcus faecalis* by three-dimensional reconstruction of thin sections of the cell. *J. Bacteriol*. **137**. 1346–1358.

Hippocrates, On Ulcers, 400 B.C.E.; Translated by Francis Adams http://classics.mit.edu/Hippocrates/ulcers.html. Last accessed on 12/02/2012.

Holt, K. B., Bard, A. J., (2005). Interaction of silver (I) ions with the respiratory chain of *escherichia coli*: An electrochemical and Scanning Electrochemical

Microscopy study of the antimicrobial mechanism of micromolar Ag^{+}. *Biochem*. **44**. 13214-13223.

Hornebecq, V., Antonietti, M., Cardinal, T., Treguer-Delapierre, M. (2003). Stable silver nanoparticles immobilized in mesoporous silica. *Chem*. *Mater*. **15** . 1993–1999.

Houk, R. S., Fassel, V. A., Flesch, G. D., Svec, H. J., Gray, A. L., Taylor, C. E. (1980). Inductively coupled argon plasma as an ion source for mass spectrometric determination of trace elements. *Anal*. *Chem*. **52**. (14). 2283-2289.

Hu, J., Xiao, X-D., Ogletree, D., Salmeron, M. (1995). Imaging the condensation and evaporation of molecularly thin films of water with nanometer resolution. *Sci*. **268**. (5208). 267-269.

Hutter, E., Boridy, S., Labrecque, S., Lalancette-Herbert, M., Kriz, J., Winnik, F. M., Maysinger, D. (2010). Microglial response to gold nanoparticles. *ACS Nano*. **4**. 2595-2606.

Imazato, S., Ehara, A., Torii M., Ebisu, S. (1998). Antibacterial activity of dentine primer containing MDPB after curing. *J*. *Dent*. **26**. 267–271.

Itoh, M., Nakamura, M., Suzuki, T., Kawai, K., Horitsu, H., Takamizawa, K. (1995). Mechanism of chromium (VI) toxicity in *Escherichia coli*: is hydrogen peroxide essential in CR (VI) toxicity? *J. Biochem*. **117**. 780-786.

Jalili, N., Laxminarayana, K. (2004). A review of atomic force microscopy imaging systems: application to molecular metrology and biological sciences. *Mechatron*. **14**. (8). 907-945.

Jarvis, K. E., Gray, A. L., Houk, R. S. (1992). Handbook of inductively coupled plasma mass spectrometry. Blackie. London. UK.

Jensen, R. H., Davidson, N. (1966). Spectrophotometric, potentiometric, and density gradient ultracentrifugation studies of the binding of silver ion by DNA. *Biopolymers*. **4** .17-32.

Jawets, E., Melnick, J. L., Adelberg, E. A. (1987). Cell Structure. *Review of Medical Microbiology*. **1**. 1-29.

Kadiiska, M. B., Xiang, Q. H., Mason, R. P. (1994). In vivo free radical generation by chromium (VI): an electron resonance spin-trapping investigation. *Chem. Res. Toxicol*. **7**. 800-805.

Kanazawa K. K., Gordon G. G. (1985). Frequency of a quartz microbalance in contact with liquid. *Anal. Chim. Acta*. **57**. (8). 1770-1771.

Kanazawa K. K., Gordon G. G. (1985). The oscillation frequency of a quartz resonator in contact with a liquid. *Anal. Chim. Acta* **175**. 99–105.

Kang, S., Pinault, M., Pfefferle, L. D., Elimelech, M. (2007). Single-walled carbon nanotubes exhibit strong antimicrobial activity. *Langmuir*. **23**. 8670-8673.

Kang, S., Mauter, M. S., Elimech, M. (2008). Physicochemical determinants of multiwalled carbon nanotube bacterial cytotoxicity. *Environ*. *Sci*. *Technol*. **42**. 7528-7534.

Karbonowska, H., Wiater, A., Hulanicka, D. (1977). Sulphate permease of *Escherichia coli* K12. *Acta Biochim. Pol.* 24. 329-334.

Kawanishi, S., Inoue, S., Sano .S. (1986). Mechanism of DNA cleavage induced by sodium chromate (VI) in the presence of hydrogen peroxide. *J. Biol. Chem*. **261**. 5952-5958.

Keller, D., Franke, F. S. (1993). Envelope reconstruction of probe microscope images. *Surf. Sci.* **294**. (3). 409-419.

Ketterer, M. E., Szechenyl, S. C. (2008). Determination of plutonium and other transuranic elements by inductively coupled plasma spectrometry: A historical perspective and new frontiers in the environmental sciences. *Spectrochim*. *Acta*. *B: Atom*. *Spect*. **63**. (7). 719-737.

Kim, J. Y., Lee, C., Cho, M., Yoon, J. (2008). Enhanced inactivation of *E. coli* and MS-2 phage by silver ions combined with UV-A and visible light irradiation. *Wat. Res*. **42**. (1-2). 356-362.

Kim, S. H., Marmo, C., Somorjai, G. A. (2001). Friction studies of hydrogel contact lenses using AFM: non-crosslinked polymers of low friction at the surface. *Biomat*. **22**. (24). 3285-3294.

Kim, H. W., Kim, B. R., Rhee, Y. H. (2010). Imparting durable antimicrobial properties to cotton fabrics using alginate-quaternary ammonium complex nanoparticles. *Carb*. *Poly*. **79**. (4). 1057-1062.

Knoll, M., Charging potential and secondary emission of bodies under electron irradiation. (1935). *Z. Tech. Phys*. **16**. 467-475.

Koch, A. L. (1981). Growth measurement. Manual of methods for general bacteriology. *American Society for Microbiology*. Washington, USA. 179-207.

Koch, A. L. (1998). The biophysics of the Gram-negative periplasmic space. *Crit*. *Rev*. *Microbiol*. **24**. (1). 23-59.

Koch, A. L., Woeste, S. (1992). Elasticity of the sacculus of *Escherichia coli*. *J*. *Bacteriol*. **174**. (14). 4811-4819.

Kopycinska-Müller, M., Geiss, R. H., Hurley, D. C. (2006). Contact mechanics and tip shape in AFM-based nanomechanical measurements. *Ultramicrosp*. **106**. 466-474.

Kuch, W., Chelaru, L. I., Offi, F., Wang, J., Kotsugi, M., Kirschner, J. (2006). Tuning the magnetic coupling across ultrathin antiferromagnetic films by controlling atomic-scale roughness. *Nat. Mater*. **5**. 128.

Li, Y., Leung, P., Yao, L., Song, Q. W., Newton, E. (2006). Antimicrobial effect of surgical masks coated with nanoparticles. *J. Hosp. Infect*. **62**. (1). 58-63.

Liau, S., Read, D., Pugh, W., Furr, J., Russell, J. (1997). Interaction of silver nitrate with readily identifiable groups: Relationship to the antibacterial action of silver ions. *Letters Applied Microbiology.* **25**. 279-283.

Liu, J. (2000). High-resolution and low-voltage FE-SEM imaging and microanalysis in materials characterization. *Mat. Charact*. **44**. (4-5)/ 353-363.

Liu, S., Wei, L., Hao, L., Fang, N., Chang, M. W., Xu, R., Chen, Y. (2009). Sharper and faster "nano darts" kill more bacteria: A study of antibacterial activity of individually dispersed pristine single-walled carbon nanotube. *ACS Nano*. **3**. 3891-3902.

London Daily, 06.05.2011, Silver Price, Consumer Price Index CPI-U: www.bis.gov.

Luedtke, W. D., Landman, U. (1989). Molecular-dynamics studies of the growth modes and structure of amorphous silicon films via atom deposition. *Phys. Rev. B*. **40**. 11733-11746.

Luo, H., Lu, Y., Shi, X., Mao, Y., Delal, N. S. (1996). Chromium (IV)-mediated Fenton-like reaction causes DNA damage: implication to genotoxicity of chromate. *Ann. Clin. Lab. Sci*. **26**. 185-191.

Lv, Y., Liu, H., Wang, Z., Liu, S., Hao, L., Sang, Y., Liu, D., Wang, J., Boughton, R. I. (2009). Silver nanoparticle-decorated porous ceramic composite for water treatment. *J. Mem. Sci*. **331**. (1-2). 50-56.

Maeda, Y., Matsumoto, T., Kawai, T. (1999). Observation of single- and double-stranded DNA using non-contact atomic force microscopy. *App. Sur. Sci*. **40**. (3-4). 400-405.

Maneerung, T., Tokura, S., Rujiravanit, R. (2008). Impregnation of silver nanoparticles into bacterial cellulose for antimicrobial wound dressing. *Carb. Poly*. **72**. (1). 43-51.

Maple, P. A., Hamilton-Miller, J. M., Brumfit, W. (1992). Comparison of the in-vitro activities of the topical antimicrobials azelaic acid, nitrofurazone, silver sulphadiazine and mupirocin against methicillin-resistant *Staphylococcus aureus*. **29**. (6). 661-668.

Martin, L. W., Chu, Y-. H., Ramesh, R. (2010). Advances in the growth and characterization of magnetic, ferroelectric, and multiferroic oxide thin films. *Mat. Sci Engin. R. Rep*. **68**. (4-6). 89-133.

Martinez-Gutierrez, F., Olive, P. L., Banuelos, A., Orrantia, E., Nino, N., Sanchez, E.
Melaiye A., Youngs, W. J. (2005). Silver and its application as an antimicrobial agent. *Expert Opin Ther Pat*, **15**. 125–130.

Méndez-Vilas, A., Corbacho, I., González-Martín, M. L., Nuevo, M. J. (2004). Direct surface probing of cell wall-defective mutants of *Saccharomyces cerevisiae* by atomic force microscopy. *App. Sur. Sci*. **238**. (1-4). 51-63.

M**é**ndez-Vilas, Bruque, J. M., González-Martín, M. L. (2007). Sensitivity of surface roughness parameters to changes in the density of scanning points in multi-scale AFM studies. Application to a biomaterial surface. *Ultramicrocosp*. **107**. (8). 617-625.

M**é**ndez-Vilas, A., Donoso, M. G., González-Carrasco, J. L., González-Martín, M. L. (2006). Looking at the micro-topography of polished and blasted Ti-based

biomaterials using atomic force microscopy and contact angle goniometry. *Colloids Surf. B*. **52**. (2). 157-166.

Meyer E., Heinzelmann H., Grütter P., Jung T., Weisskopf T., Hidber H. R., Lapka R., Rudin H., Güntherodt H. J. (1988). *J. Microsc.* **152**. 269.

Mirzanji, F., Ghassempour, A., Allahmadi, A., Esmaelli, M. A. (2011). Antibacterial effect of silver nanoparticles on *Staphylococcus aureus*. *Res. In. Microbiol*. **162**. (5). 542-549.

Miyata, T., Kawaguchi, S., Ishii, M., Minami, T. (2003). High sensitivity gas sensors using Cu-phtahocyanine thin films. *Thin*. *Film*. *Solid*. **425**. (1-2). 255-259.

Miyawaki, J., Yudasaka, M., Azami, T., Kubo, Y., Lijima, S. (2008). Toxicity of single-walled carbon nanohorns. *ACS Nano*. **2**. 213-226.

Miller, J. C., Miller, J. N. (1994). Statistics for Analytical Chemistry. Ellis Horwood PTR Prentice Hall, London, UK. **3**, 65-70.

Möller, C., Allen, M., Elings, V., Engel, A., Müller, D. (1999). Tapping-mode atomic force microscopy produces faithful high-resolution images of protein surfaces. *Biophys. J.* **77**. (2). 1150-1158.

Montaser, A., Golightly, D. W. (1992). Inductively coupled plasmas in analytical atomic spectrometry. VCH. New York. USA.

Moreira, C. M., Duarte, F. A., Lebherz, J., Pozebon, D., Flores, E. M. M., Dressier, V. L. (2011). Arsenic speciation in white wine by LC-ICP-MS. *Food*. *Chem*. **126**. (3). 1406-1411.

Muramatsu H., Dicks J. M., Tamiya E., Karube I. (1987). *Anal. Chem.* **59**. 2760.

Muramatsu H., Tamiya E., Karube I. (1988). *Anal. Chem.* **60**. 2142.

Nel A., Xia, T., Madler, L., Li, N. (2006). Toxic potential of materials at the nanolevel. *Science*. **311**. 622-627.

Nelms, S. M. (2005). ICP Mass Spectrometry Handbook. Blackwell Publishing, Cheshire, UK, Preface. Chapter 2. Page 45.

Neogi, P. (2006). Length scales and roughness on a growing solid surface: a review. *J. Electroanal. Chem*. **595**. (1). 1-10.

Nies, A., Nies, D. H., Silver, S. (1989). Cloning and expression of plasmid genes encoding resistance to chromate and cobalt in *Alcaligenes eutrophus*. *J. Bacteriol*. **171**. 5065-5070.

Nowicki, B. (1985). Multiparameter representation of surface roughness. *Wear*. **102.** 161–176.

Ohashi, S., Saku., S., Yamamoto, K. (2004). Antibacterial activity of silver inorganic agent YDA filler. *J. Oral. Rehabil*. **31**. 364–367.

Ohtake, H., Cervantes, C., Silver, S. (1987). Decreased chromate uptake in *Pseudomonas fluorescens* carrying a chromate resistance plasmid. *J. Bacteriol*. **169**. 3853-3856.

Ong, S-Y., Wu, J., Moochhala, S. M., Tan, M-H., Lu, J. (2008). Development of a chitosan-based wound dressing with improved hemostatic and antimicrobial properties. *Biomat*. **29**. (32). 4323-4332.

Panácek, A., Kvítek, L., Prucek, R., Kolár, M., Vecerová R., Pizúrová, N. (2006). Silver colloid nanoparticles: synthesis, characterization, and their antibacterial activity. *J Phys Chem B*. **110**. 16248–16253.

Parikh, D.V., Fink, T., Rajasekharan, K., Sachinvala, N. D., Sawhney, A. P. S., Calamari, T. A. (2005). Antimicrobialsilver/sodium carboxymethyl cotton dressings for burn wounds. *Text Res J*, **75** . 134–138.

Pham, M. T., Matz, W., Selfarth, H. (1998). Surface roughness with nanometer-scale Ag particles generated by ion implantation. *Anal*. *Chim*. *Acta*. **350**. (1-2). 209-220.

Poland, C. A., Duffin, R., Kinloch, I., Maynard, A., Wallace, W. A. H., Seaton, A., Stone, V., Brown, S., MacNee, W. (2008). Nanotubes introduced into the abdominal cavity of mice show asbestos-like pathogenicity in a pilot study. *Nat*. *Nanotech*. **3**. 423-428.

Politi, P., Grenet, G., Marty, A., Ponchet, A., Villain, J. (2000). Instabilities in crystal growth by atomic or molecular beams. *Phys. Rep*. **324**. (5-6). 271-404.

Ponce-de-Leon, S. (1991). The needs of developing countries and the resources required. *Journal of Hospital Infections*. **18**. 376-381.

Poon, C. Y., Bhushan, B. (1995). Comparison of surface roughness measurements by stylus profiler, AFM and non-contact optical profiler. *Wear*. **190**. (1). 76-88.

Plowman, R. (1999). The socioeconomic burden of hospital-acquired infection. *London Public Health Laboratory Service and London School of Hygiene and Tropical Medicine.*

Rana, D., Kim, Y., Matsuura, T., Arafat, H. A. (2011). Development of antifouling thin-film composite membranes for seawater desalination. *J. Mem. Sci*. **367**. (1-2). 110-118.

Richards, M. J., Russo, P. L. (2007). Surveillance of hospital-acquired infections in Australia – one nation, many states. *J. Hosp. Infect*. **65**. (2). 174-181.

Ricketts, C. R., Lowbury, E. J., Lawrence, J. C., Hall, M., Wilkins, M. D. (1970). Mecahnism of prophylaxis by silver compounds against infection of burns. *J. Brit*. *Med.* **1**. (707). 444-446.

Rönnow, D., Eisenhammer, T., Roos, A. (1999). Surface roughness characterization of a thin transparent dielectric-silver tandem by spectroscopic light scattering. *Sol*. *Ener*. *Mat*. *Sol. Cell*. **52**. (1-2). 37-43.

Rosenberger, R. F., Elsden, S. R. (1960). The yields of *Streptococcus faecalis* grown in continuous culture. *J. Gen. Microbiol*. **22**. 726-739.

Rothen, A. (1945). The Ellipsometer, an apparatus to measure thicknesses of thin surface films. *Review Scientific Instrumentation*. **16**. (2). 26-30.

Rubin, S., Passell, T. O., Bailey, E. (1957). Chemical analysis of surfaces by nuclear methods. *Analytical Chemistry*. **29**. 736.

Ruiz, M., Bach, F., Av-Gay, H. (2010). Synthesis, characterization and evaluation of antimicrobial and cytotoxic silver and titanium nanoparticles. *Nanomed*. *Nanotech. Biol*. *Med*. **6**. 681-688.

Rupp, M. E., Fitzgerald, T., Marion, N., Helget, V., Puumala, S., Anderson, J. R. (2004). Effect of silver-coated urinary catheters: efficacy, cost-effectiveness, and antimicrobial resistance. *Am*. *J*. *Infect*. *Control*. **32**. 445–450.

Russel, A. D., Chopra, I. (1996). Understanding antibacterial action and resistance, Ellis Horwood, Hemel, Hempstead, Hertofdshire. [Chapter 3].

Russel, A. D., Hugo, W. B. (1994). Antimicrobial activity and action of silver. Progress in Medicinal Chemistry. **31**. 351-370.

Sabbani, S., Gallego-Perez, D., Nagy, A., Waldman, W. J., Hansford, D., Dutta, P. K. (2010). Synthesis of silver-zeolite films on micropattered porous alumina and its application as an antimicrobial substrate. *Micropor*. *Mesopor*. *Mat*. **135**. (1-3). 131-136.

Salapaka, M., Chen, D. (1998). Stability and sensitivity analysis of periodic orbits in tapping mode atomic force microscopy. *Proc. Conf. Decision. Control*. 2047–2052.

Salton, M. R. (1963). The relationship between the nature of the cell wall and the Gram stain. *J. Gen*. *Microbiol*. **30**. 223-235.

Sant, S. B., Gill, K. S., Burrell, R. E. (1999). Morphology of novel antimicrobial silver films deposited by magnetron sputtering. *Acta Metallurgica*. **41**. 1333-1339.

Santiago, A. S., dos Santos, E. A., Sader, M. S., Santiago, M. F., Soares, G. A. (2005). Response of osteoblastic cells to titanium submitted to three different surface treatments. *Braz. Oral. Res*. **19**. (3). 203-208.

Sauerbrey G. Z. (1959). Use of quartz vibration for weighing thin films on a microbalance. J. Physic. 155. 206-212.

Sambrook. J., Russell, D. (2001). *Molecular Cloning – A Laboratory Manual*. Cold Spring Harbor Laboratory Press, USA. A1.14, A1.7.

Samuel, U., Guggenbichler, J. P. (2004). Prevention of catheter-related infections: the potential of a new nano-silver impregnated catheter. *Int*. *J*. *Antimicrob*. *Agents*. **23**. Suppl. 1. S75–S78.

Schreurs, W. J., Rosenberg, H. Effect of silver ions on transport and retention of phosphate by *escherichia coli*. *J. Bacteriol*. **152**. 7-13.

Schwander, P., Kisielowski, C., Seibt, M., Baumann, F. H., Kim, Y., Ourmazd, A. (1993). Mapping projected potential, interfacial roughness, and composition in general crystalline solids by quantitative transmission electron microscopy. *Phys. Rev. Lett*. **71**. (25). 4150-4153.

Sharma, G. T., Dubey, P. K., Meur, S. K. (2009). Survival and developmental competence of buffalo preantral follicles using three-dimensional collagen gel culture system. **114**. (1-3). 115-124.

Shi, X., Dalal, N. S. (1990). On the hydroxyl radical formation in the reaction between hydrogen peroxide and biologically generated chromium (V) species. *Arch. Biochem. Biophys.* **277**. 342-350.

Shin, P-K., Aya, Y., Ikegami, T., Ebihara, K. (2008). Application of pulsed laser deposited zinc oxide films to thin film transistor device. *Thin*. *Film*. *Solid*. **516**. 3767-3771.

Silver, S. (2003). Bacterial silver resistance: molecular biology and uses and misuses of silver compounds. *FEMS Microbiology Reviews*. **27**. (2-3). 341-353.

Sirko, A., Hryiewicz, M., Hulanicka, D., Böck, A. (1990). Sulfate and thiosulfate transport in *Escherichia coli* K-12: nucleotide sequence and expression of the *cysTWAM* gene cluster. *J. Bacteriol*. 172. 3351-3357.

Slawson, R. M., Vandyke, M. I., Lee, H., Trevors, J. T. (1992). Germanium and silver resistance, accumulation, and toxicity in microorganisms. *Plasmid*. **27**. 72–77.

Smith, D. O., Cohen, M. S., Weiss, G. P. (1960). Oblique-incidence anisotropy in evaporated permalloy films. *J. App. Phys*. **31**. 1755-163.

Sonenshein, A. L., Hoch, J. A., Losick, R. (1993). *Bacillus subtilis* and other Gram-positive bacteria. Biochemistry, physiology and molecular genetics. *Am*. *Soc*. *Microbiol*. Washington. USA. Chapter 2. Page 17.

Spaciciapoli, P., Buxton, D., Rothstein, D., Friden, P. (2001). Antimicrobial activity of silver nitrate against periodontal pathogens. *J. Peri. Res*. **36**. (2). 108-113.

Spiller, E., Stearns, D., Krumrey, M. (1993). Multilayer X-ray mirrors: interfacial roughness, scattering, and image quality. **74**. (1). 107-118.

Spadaro, J.A., Berger, T.J., Barranco, S.D. Barranco. (1974). Antibacterial effects of silver electrodes with weak direct current. *Antimicrobial Agents Chemotherapeutics* **6**. 637–642.

Stevens, K. N. J., Crespo-Biel, O., van den Bosch, E. E. M., Dias, A. A., Knetsch, M. L. W., Aldenhoff, Y. B. J., van der Veen, F. H., Maessen, J. G. (2009). The relationship between the antimicrobial effect of catheter coatings containing silver nanoparticles and the coagulation of contacting blood. *Biomat*. **30**. (22). 3682-3690.

Stobie, N., Duffy, B., McCormack, D. E., Colreavy, J., Hidalgo, M., McHale, P. (2008). Prevention of *Staphylococcus epidermidis* biofilm formation using a low-temperature processed silver-doped phenyltriethoxysilane sol–gel coating. *Biomaterials*, **29**. 963-969.

Stoudt M. R., Hubbard, J. B. (2005). Analysis of deformation–induced surface morphologies in steel sheet. *Acta. Mater*. **53**. 4293–4304.

Stout, K. J., Sullivan, P. J., Dong, W. P., Mainsah, E., Luo, N., Mathia T. (1993). The development of methods for the characterisation of roughness in three dimensions, Commission of the European Communities, University of Birmingham, UK. Chapters 11–12.

Strathmann, M., Wingender, J. (2004). Use of an oxonol dye in combination with confocal laser scanning microscopy to monitor damage to *Staphylococcus aureus* cells during colonisation of silver-coated vascular grafts. *Int. J. Antimicrob. Agents*. **24**. 234–240.

Strus, M. C., Raman, A., Han, C-S., Nguyen, C. V. (2005). Imaging artefacts in atomic force microscopy with carbon nanotube tips. *Nanotech*. **16**. 2482-2492.

Tanaka, S., Grévin, B., Rannou, P., Suzuki, H., Mashiko, S. (2006). Conformational studies of self-organized regioregular poly(3-dodecylthiophene)s using non-contact atomic force microscopy in ultra high vacuum condition. *Thin. Solid. Film*. **499**. (1-2). 168-173.

Thomas, S., McCubbin, P. (2003). A comparison of the antimicrobial effects of four silver-containing dressings on three organisms. *Journal of Wound Care*. **12**. 101-107.

Tombelli S., Minunni M., Mascini M. (2005). Piezoelectric biosensors: Strategies for coupling nucleic acids to piezoelectric devices. *Methods*. **37**. 48-56.

Tompkins, H. G. (1993). A User's Guide to Ellipsometry. Dover Publications Inc. Mineola, New York, USA. 1, 17.

Ulkur, E., Oncul, O., Karagoz, H., Yeniz, E., Celikoz, B. (2005). Comparison of silver-coated dressing (Acticoat), chlorhexidine acetate 0.5% (Bactigrass), and fusidic acid 2% (Fucidin) for topical antibacterial effect in methicillin-resistant staphylococci-contaminated, full-skin thickness rat burn wounds. *Burns*. **31**. 874–877

Ungersböck, A., Rahn, B. (1994). Methods to characterize the surface roughness of metallic implants. *J. Mater. Sci.: Mater.* **5**. (6-7). 434-440.

Valkonen, A. E. (1987). Plastic deformation and roughness of free metal surfaces. Ph.D. Thesis, The Ohio State Univeristy, Columbus, Ohio, U.S.A.

van Dijken, S., Di Santo, G., Poelsema, B. (2000). Growth-induced uniaxial anisotropy in grazing-incidence deposited magnetic films. *App. Phys. Lett*. **77**. 2030.

van Dijken, S., Jorritsma, L. C., Poelsema, B. (1999). Steering-enhanced roughening during metal deposition at grazing incidence. *Phys. Rev. Lett*. **82**. (20). 4038-4041.

van Dijken, S., Jorritsma, L. C., Poelsema, B. (2000). Grazing-incidence metal deposition: Pattern formation and slope selection. *Phys. Rev. Lett*. **61**. (20). 14047-14058.

van Dijken, S., Jorritsma, L. C., Poelsema, B. (2001). Influence of the deposition angle on the magnetic anisotropy in thin Co films on Cu(001) *Phys. Rev. Lett*. **63**. 10443-10453.

Wang, J-M., Meng, M-Q., Lu, F., Shi, B-R., Wang, F-X., Li, W., Shuen, D-Y., W, X-M. (1999). Rutherford Backscattering/channeling study of the implanted MeV Au^{+} in silicon. *Mat. Sci. Engin. B*. **57**. (2). 92-96.

Wang, J. Y., Hofmann, S., Zalar, A., Mittemeijer, E. J. (2003). Quantitative evaluation of sputtering induced surface roughness in depth profiling of polycrystalline multilayers using Auger electron spectroscopy. *Thin. Solid. Film*. **444**. (1-2). 120-124.

Warheit, D. B., Laurence, B. R., Reed, K. L., Roach, D. H., Reynolds, G. A. M., Webb, T. R. (2004). Comparative pulmonary toxicity assessment of single-walled carbon nanotubes in rats. *Toxicol*. *Sci*. **77**. 117-125.

Watson, D. W., Brandly, C. A. (1949). Virulence and Pathogenicity. In: Clifton CE, Raffel S, Baker HA (Eds). *Annual Review of Microbiology*. Annual Reviews Inc, Stanford, California, USA, pp. 195-220.

Wayne, C. E., and Wayne, R. P. (1995). Photochemistry. *Oxford Science Publications*. Oxford. UK. **1**. 4.

Wenzel, R. P. (1995). The economics of nosocomial infections. *Journal of Hospital Infections*. **31**. 79-87.

Williams, J. S., Möller, W. (1978). On the determination of optimum depth-resolution conditions for Rutherford backscattering analysis. *Nuc*. *Ins*. *Meas*. **157**. (2). 213-221.

Williams, R. L., Doherty, P. J., Vince, D. G., Grashoff, G. J., Williams, D.F. (1989) The Biocompability of Silver. *Critical Reviews in Biocompatibility*. **5**. 221.

Xie X. N., Chung H. J., Sow C. H., Wee A. T. S. (2006). Nanoscale materials patterning and engineering by atomic force microscopy nanolithography. *Mat. Sci. Engin. R. Report*. **54**. (1-2). 1-48.

Xu, L-C., Siedlecki, A. (2012). Submicrob-textured biomaterial surface reduces *staphylococcal* bacterial adhesion and biofilm formation. *Acta. Biomater*. **8**. (1). 72-81.

Yang, H. C., Pon, L. A. (2003). Toxicity of metal ions used in dental allows: A study in the yeast *Saccharomyces cerevisiae*. *Drug*. *Chem*. *Toxicol*. **152**. 7-13.

Yang, G., Xie, J., Hong, F., Cao, Z., Yang, X. (2011). Antimicrobial activity of silver nanoparticle impregnated bacterial cellulose membrane: Effect of fermentation carbon sources of bacterial cellulose. *Carb*. *Poly*. In Press, Corrected Proof.

Yoksan, R., Chirachanchai, S. (2010). Silver nanoparticle-loaded chitosan-starch based films: Fabrication and evaluation of tensile, barrier and antimicrobial properties. *Mat*. *Sci*. *Eng*. *C*. **30**. (6). 891-897.

Yoon, J., Lund, D. B. (1994). Magnetic treatment of milk and surface treatment of plate heat exchangers: effects on milk fouling. *J*. *Food*. *Sci*. **59**. 964-969.

Yu, J., Amar, J. G. (2002). Effects of short-range attraction in metal epitaxial growth. *Phys. Rev. Lett*. **89**. 286103-286107.

Zhang, Y., Ali, S. F., Dervishi, E., Xu, Y., Li, Z., Casciano, D., Biris, A. S. (2010). Cytotoxicity effects of graphene and single-wall carbon nanotubes in neural phaechromocytoma-derived PC12 cells. *ACS Nano*. **4**. 3181-3186.

Zhang, M., Chiu, T-L., Lin, C-F., Lee, J-H., Wang, J-K., Wu, Y. (2011). Roughness characterization of silver oxide anodes for use in efficient top-illuminated organic solar cells. *Sol*. *Ener*. *Mat*. *Sol*. *Cell*. **95**. (9). 2606-2609.

Zoureb, M., Elwary, S., Turner, A. (2008). Principles of Bacterial Detection: Biosensors, Recognition Receptors and Microsystems. Springer. New York. USA. **1**. 9.

Appendices

Appendix A. Raw data optical density of *E. coli* growth

This data was presented in section 5.2 in figure 38 and was used to calculate antimicrobial activity throughout this study.

Time (Hours)	Optical Density Readings (600 nm)		
	Reading 1	Reading 2	Reading 3
0	0	0	0
0.5	0.0018 ± 0.0002	0.0017 ± 0.0001	0.0018 ± 0.0001
1	0.0017 ± 0.0001	0.0019 ± 0.0002	0.0020 ± 0.0002
2	0.0041 ± 0.0002	0.0025 ± 0.0002	0.0032 ± 0.0001
4	0.0513 ± 0.0003	0.0496 ± 0.0004	0.0441 ± 0.0002
8	0.1355 ± 0.0006	0.1395 ± 0.0003	0.1254 ± 0.0005
12	0.3479 ± 0.0009	0.3522 ± 0.0014	0.3356 ± 0.0008
16	1.7712 ± 0.0011	1.7986 ± 0.0019	1.7595 ± 0.0010
24	2.2057 ± 0.0013	2.1666 ± 0.0017	2.1920 ± 0.0016
48	2.2774 ± 0.0013	2.2547 ± 0.0020	2.3054 ± 0.0015

Appendix B. Raw data optical density of *S. aureus* growth

This data was used to calculate antimicrobial activity throughout this study.

Time (Hours)	Optical Density Readings (600 nm)		
	Reading 1	Reading 2	Reading 3
0	0	0	0
0.5	0.0019 ± 0.0002	0.0018 ± 0.0002	0.0020 ± 0.0001
1	0.0020 ± 0.0003	0.0021 ± 0.0001	0.0023 ± 0.0002
2	0.0038 ± 0.0002	0.0042 ± 0.0002	0.0032 ± 0.0002
4	0.0654 ± 0.0006	0.0721 ± 0.0004	0.0688 ± 0.0009
8	0.1572 ± 0.0010	0.1395 ± 0.0012	0.1401 ± 0.0007
12	0.4319 ± 0.0011	0.4432 ± 0.0011	0.5066 ± 0.0018
16	1.9650 ± 0.0018	2.0031 ± 0.0017	1.9870 ± 0.0020
24	2.2317 ± 0.0015	2.2216 ± 0.0023	2.2408 ± 0.0022
48	2.4556 ± 0.0022	2.5457 ± 0.0019	2.3182 ± 0.0017